INTEGRATION OF SCREEN-PRINTED BISMUTH FERRITE THICK FILMS ONTO CERAMIC AND METAL SUBSTRATES

Evgeniya Khomyakova

Doctoral Dissertation
Jožef Stefan International Postgraduate School
Ljubljana, Slovenia

Supervisor: Asst. Prof. Dr. Andreja Benčan Golob, Jožef Stefan International Postgraduate School and Jožef Stefan Institute, Ljubljana, Slovenia
Co-Supervisor: Asst. Prof. Dr. Tadej Rojac, Jožef Stefan International Postgraduate School and Jožef Stefan Institute, Ljubljana, Slovenia

Evaluation Board:
Prof. Dr. Barbara Malič, Chair, Jožef Stefan International Postgraduate School, Jožef Stefan Institute, Ljubljana, Slovenia
Prof. Dr. Anton Meden, Member, Faculty of Chemistry and Chemical Technology, Ljubljana, Slovenia
Assoc. Prof. Dr. Sverre Magnus Selbach, Member, Faculty of Natural Sciences and Technology, Trondheim, Norway

MEDNARODNA PODIPLOMSKA ŠOLA JOŽEFA STEFANA
JOŽEF STEFAN INTERNATIONAL POSTGRADUATE SCHOOL



Evgeniya Khomyakova

INTEGRATION OF SCREEN-PRINTED BISMUTH FERRITE THICK FILMS ONTO CERAMIC AND METAL SUBSTRATES

Doctoral Dissertation

INTEGRACIJA DEBELIH PLASTI BIZMUTOVEGA FERITA NA KERAMIČNE IN KOVINSKE PODLAGE Z METODO SITOTISKA

Doktorska disertacija

Supervisor: Asst. Prof. Dr. Andreja Benčan Golob

Co-Supervisor: Asst. Prof. Dr. Tadej Rojac

Ljubljana, Slovenia, October 2016

To my mother, Alexandra Shuvalskaya, my father, Andrey Ladus, and my dear sister, Yaroslava

Acknowledgments

Here I would like to express my gratitude to everyone who helped me during this PhD study.

My first and major thanks go to my mentor Asst. Prof. Dr. Andreja Benčan-Golob. 3.5 years ago, at the moment of my enrollment at the Jozef Stefan IPS study program, almost all of my scientific skills, such as searching, reading and processing of scientific literature, writing of academic texts, systematization and presentation of scientific results, organization and communication skills, and even my English language proficiency, were at a very low level. So, both of us, I and my mentor, have been working very hard all these years in order to improve them all. Andreja needed a lot of passion, energy, self-control, resourcefulness and patience to work with me and I want to thank her for finding all of these for me. I thank her for caring, for always being there for me; for all the pieces of advice concerning fields of science and personal life that she gave me; for supporting, encouraging me and pushing me to move forward. Andreja, thank you for everything!

I also deeply thank my co-mentor Asst. Prof. Dr. Tadej Rojac for his extensive knowledge, open, creative mind, and bright ideas. Not only were all the meetings with him extremely productive, fruitful and efficient, but also fun, easy and non-exhausting (even 5-hour-long ones☺). Tadej, thanks for all your help, for the moral and scientific support you have been giving me all this time, and for being my mentor!

I would like to express my gratitude to Prof. Dr. Barbara Malič and the late Prof. Dr. Marija Kosec for seeing the potential in me four years ago and accepting me as a PhD student at the Electronic Ceramics Department of the Jozef Stefan Institute.

I sincerely thank all the people working at Electronic Ceramics Department. I thank our engineers, Brigita Kmet, Jena Cilinšek and Silvo Drnovšek, and our student, Maja Makarovič, who not only countlessly helped me with laboratory work, but also taught me crucially important steps of the experimental procedure. Our students Matej Šadl and Aneja Tuljak gave me a lot of help in experimental work, which made my work much easier, I very much appreciate it. I thank my co-workers, Asst. Prof. Dr. Hana Uršič for provided help in AFM/PFM analysis, Asst. Prof. Dr. Tadej Rojac for electrical measurements, Asst. Prof. Dr. Andreja Bencan for TEM analysis, Dr. Julian Walker for English grammar corrections of our papers. I also thank all my other colleagues (and former colleagues) at the K5 department, including Dr. Katarina Vojisavljevic, Dr. Tanja Pečnik, Dr. Raluca Frunza, Dr. Kostja Makarovič, Dr. Jernej Pavlič, Andraž Bradeško, Aleksandr Matavž for the warm and friendly atmosphere in the offices.

I also thank people from outside of K5 department, i.e. Maja Koblar from the Center of Electron Microscopy and Microanalysis at the Jozef Stefan Institute for her help with the EBSD analysis, and Edi Kranjc from the National Institute of Chemistry for performing numerous XRD analyses.

And I want to take the chance to thank the co-authors of our article for their great help in interpreting the results, building up a story from the results and writing the article, those are Assoc. Prof. Dr. John Daniels from School of Materials Science and Engineering, University of New South Wales, and Prof. Dr. Dragan Damjanovic from Ceramics Laboratory, Swiss Federal Institute of Technology in Lausanne-EPFL.

Last but not least, I express my gratitude to the Slovenian Research Agency for the financial support; this PhD thesis would not exist without it.

Abstract

$BiFeO_3$ (BFO) has been shown to have great potential for many applications due to a number of attractive properties, such as its multiferroic nature at room temperature, high Curie temperature (T_C ~ 830 ^oC), and high remanent polarization. Thus, various piezoelectric devices, for example, sensors, actuators and transducers, can be prepared using an active layer of BFO-based materials integrated onto substrates as thick films. But, the processing of the BFO thick films is challenging due to readily occurring chemical reactions between the substrate, electrode and BFO layer. The present literature data does not provide the necessary information on the preparation conditions that could be used to improve the quality of BFO thick films on a broader basis.

The purpose of this PhD thesis was to study the interactions between different substrates and the BFO films and thus be able to prepare high-quality BFO thick films in terms of phase composition and microstructure.

In the first part of this dissertation we provide a comprehensive investigation of BFO thick films prepared by screen-printing and their interactions with ceramic (Au/Al_2O_3) and metal (Ag, Au, Pt) substrate materials during processing. We show that the microstructure and phase composition of the BFO thick films is strongly dependent on two parameters, i.e., the impurity present in the electrode and the sintering temperature. By optimizing the sintering temperature (740 ^oC), and by using a high-purity Ag metal substrate we successfully prepared dense and nearly single-phase BFO thick films. While the local ferroelectric behavior of this film has been confirmed by piezo-response force microscopy analysis, its macroscopic electrical response is characterized by a high electrical conductivity coupled with an interface-related, diode-like, current-voltage behavior.

However, not only is it challenging to prepare high-quality BFO thick films due to processing issues, but it is problematic to pole the material due to its high coercive field and high electrical conductivity. The results of the last part of the dissertation suggest an alternative way of poling BFO films by sintering (annealing) at a temperature above the ferroelectric-paraelectric phase transition, overcoming the obstacle of poling the BFO "ex-situ" using large external electric fields. Direct and converse piezoelectric measurements confirmed that the as-sintered BFO thick films on Pt/Al_2O_3 substrates yield d_{33} values of up to ~20 pC/N. It was observed that a significant self-poling effect only appears in cases when the films are heated and cooled through the T_C (~ 820 ^oC). These self-poled films exhibit a microstructure with randomly oriented columnar grains. The compressive strain gradient across the film thickness cooled from above the T_C was experimentally confirmed and is suggested to be responsible for the self-poling effect.

Povzetek

$BiFeO_3$ (BFO) je zaradi svoje multiferoične narave pri sobni temperaturi, visoke temperature feroelektričnega-paraelektričnega faznega prehoda (T_C ~ 830 °C) in visoke remanentne polarizacije zanimiv za uporabo v številnih aplikacijah. V piezoelektričnih napravah, kot so senzorji, aktuatorji in pretvorniki, je BFO kot funkcionalni material lahko integriran na podlago v obliki debele plasti. Vendar pa je, v primeru BFO, priprava debelih plasti zaradi pogostih kemijskih reakcij med podlago, elektrodo in plastjo BFO zahtevna. Prav tako v literaturi ni moč zaslediti potrebnih informacij o pogojih priprave, ki bi jih lahko v širšem kontekstu uporabili za izboljšanje kakovosti debelih plasti BFO.

Namen doktorske disertacije je bil študij interakcij med debelimi plastmi BFO in različnimi podlagami. Razumevanje in obvladovanje interakcij med plastmi naj bi vodilo k pripravi kakovostnih, debelih plasti BFO s primerno fazno sestavo in mikrostrukturo.

V prvem delu doktorskega dela smo podrobno preiskali interakcije med debelimi plasti BFO in keramičnimi (Au/Al_2O_3) in kovinskimi (Ag, Au, Pt) podlagami. Debele plasti BFO smo pripravili z metodo sitotiska. Pokazali smo, da sta mikrostruktura in fazna sestava debelih plasti BFO močno odvisni od dveh parametrov: od nečistoče prisotne v elektrodi in od temperature sintranja. Z optimizacijo temperature sintranja (740 °C) in z uporabo podlage iz kovinskega Ag smo uspešno pripravili gosto in skoraj enofazno debelo plast BFO. Plasti smo z mikroskopom na atomsko silo potrdili lokalni feroelektrični odziv. Makroskopsko se je plast, ki je izkazovala visoko električno prevodnost, obnašala kot dioda.

Vendar pa BFO ni le znan po zahtevni pripravi, zaradi visokega koercitivnega polja in visoke električne prevodnosti je ta material tudi težje polarizirati, saj zahteva uporabo zadosti velikega zunanjega električnega polja. V zadnjem delu disertacije zato predlagamo alternativni način polarizacije debelih plasti BFO, in sicer s sintranjem (žganjem) plasti nad feroelektričnim-paraelektričnim faznim prehodom. Direktne in obratne piezoelektrične meritve so potrdile, da izkazujejo debele plasti BFO na podlagah Pt/Al_2O_3, sintrane nad temperaturo prehoda T_C(~820°C), samo-polarizacijo z d_{33} ~ 20 pC/N. Za omenjene plasti je značilna mikrostruktura s stebričastimi zrni. Študija razkriva, da se v plasteh pri ohlajanju preko feroelektričnega-paraelektričnega faznega prehoda pojavi gradient tlačnih napetosti, ki vodi do omenjene samo-polariziracije debelih plasti BFO.

Contents

List of Figures xv

List of Tables xix

Abbreviations xxi

Symbols xxiii

1 Introduction 1
1.1 Motivation and Outline 1
1.2 $BiFeO_3$ 2
1.2.1 Crystal structure of $BiFeO_3$ 2
1.2.1.1 Crystal structure at room temperature 2
1.2.1.2 Crystal structure at increased temperature or pressure 3
1.2.2 $BiFeO_3$ ceramic processing issues 4
1.2.2.1 Thermodynamic aspects 4
1.2.2.2 Reaction kinetics, bismuth evaporation and segregation of sillenite phase 7
1.3 Thick-Film Technology 9
1.3.1 Screen-printing 9
1.3.2 Thick-film processing issues 10
1.4 $BiFeO_3$-Based Thick Films 13

2 Aims and Hypothesis 15

3 Materials and Methods 17
3.1 List of Chemicals and Accessories 17
3.2 Processing of $BiFeO_3$ Thick Films 19
3.2.1 Solid-state synthesis of powder for screen printing 19
3.2.2 Screen-printing and sintering of the thick-film structures 19
3.3 Characterization of the Powders and Films 21
3.3.1 Particle size distribution analysis 21
3.3.2 Heating-stage microscope 21
3.3.3 X-ray diffraction 21
3.3.4 *In-situ* X-ray diffraction 22
3.3.5 Analytical microscopy 22
3.3.5.1 Scanning electron microscopy 22
3.3.5.2 Transmission electron microscopy 23
3.3.5.3 Atomic force microscopy/Piezoresponse Force Microscopy 23
3.3.6 Electrical and electro-mechanical properties 23

4 Results and Discussion 25
4.1 Characterization of the Bi_2O_3–Fe_2O_3 Powder Mixture 25
4.2 $BiFeO_3$ Thick Films on the Au/Al_2O_3 Substrate 27
4.2.1 The influence of the sintering temperature on the phase composition and microstructure 27
4.3 $BiFeO_3$ Thick Films on the Noble Metal Foils 36
4.3.1 The influence of the substrate material on the phase composition and the microstructure 36

4.3.2 The influence of the sintering or post-annealing temperature on the phase composition and the microstructure 38
4.3.3 Investigation of the electric properties of the $BiFeO_3$ thick film on a Ag foil 40
4.3.3.1 Macroscopic properties 40
4.3.3.2 Local properties 41
4.4 Self-Poling Effect in $BiFeO_3$ Thick Films on a Pt/Al_2O_3 Substrate 43
4.4.1 Evidence of the self-poling effect 43
4.4.2 Investigation of the microstructure 48
4.4.3 Strain gradient in $BiFeO_3$ thick films 53
4.4.4 Discussion of the self-poling effect 55
4.4.5 Characterization of macroscopic piezoelectric behaviour of the self-poled $BiFeO_3$ thick films 57

5 Summary and Conclusions **59**

References **61**

Bibliography **71**

Biography **73**

List of Figures

Figure 1.1: Representation of rhombohedral, R3c, $BiFeO_3$ crystal structure in hexagonal (a), rhombohedral (b) and pseudocubic (c) crystallographic settings, and the geometrical relationship between the different settings (d)..... 2

Figure 1.2: Temperature-induced or hydrostatic-pressure-induced phase transitions in rhombohedral, R3c, BFO. Bi_2O_3–Fe_2O_3 phase diagram (a); schematic pressure-temperature phase diagram of BFO (b).....4

Figure 1.3: XRD patterns of BFO at different sintering temperatures (a). Calculated temperature dependence of the Gibbs free energy ($\Delta G°(T)$) (b) 5

Figure 1.4: Proposed phase relations in the ternary Bi_2O_3–Fe_2O_3–AO_x system where AO_x is SiO_2. (a); XRD patterns of pure Bi_2O_3–Fe_2O_3 mixture and with 0.1 and 0.5 wt% additions of SiO_2 sintered at 800 °C for 5 h in air (b).....6

Figure 1.5: Schematic representation of the reaction mechanism for the solid-state synthesis of BFO from Bi_2O_3 and Fe_2O_3.....7

Figure 1.6: SEM images of BFO ceramics sintered at 760°C for 6 h in air (marked "non-immersed") (a), sintered at 820°C for 10 h and additionally post-annealed for 10 h at 820 °C in a BFO packing powder (marked "immersed") (b), at 820°C in air (c) and at 880°C in air (d).....8

Figure 1.7: Schematic representation of a piezoelectric thick-film structure 9

Figure 1.8: Schematics of the processing steps for the screen-printing of thick films.....10

Figure 1.9: Influence of thermal stress on thd piezoelectric performance of PZT thick films deposited on silicon, sapphire and YSZ substrates.... 11

Figure 1.10:SEM cross-section images with corresponding XRD patterns of 0.65PMN–0.35PT thick films on Pt/PZT/Al_2O_3 (a), and on Pt/AlN substrates (b). Both thick films were sintered at 950 ^oC for 2 h.....12

Figure 3.1: Schematic illustration of temperature profiles for the sintering step (a); and for the post-annealing step (b)..... 20

Figure 4.1: Characterization of the Bi_2O_3–Fe_2O_3 powder mixture. Granulomentric analysis of the mixture after 1, 2, 3 and 4 hours of milling (a) and calculated d_{10}, d_{50} and d_{90} particle sizes as a function of milling time (lines are drawn as a guide to the eye) (b). BE SEM images (c,d) of the 4-hours-milled Bi_2O_3–Fe_2O_3 powder mixture 25

Figure 4.2: Densification curve of the 4-hours-milled Bi_2O_3–Fe_2O_3 powder mixture with images of the Bi_2O_3–Fe_2O_3 pellet at 730 ^oC and 830 ^oC..... 26

Figure 4.3: XRD patterns of BFO/Au/Al_2O_3 structures sintered at different temperatures (a) and enlarged region of the XRD patterns illustrating the major peaks of secondary mullite and sillenite phases (b)..... 27

Figure 4.4: Quantitative phase composition of BFO thick films as a function of sintering temperature.....28

Figure 4.5: EDXS spectra of the perovskite BFO, mullite $Bi_2Fe_4O_9$ and sillenite $Bi_{25}FeO_{39}$ phases acquired at 15 keV..... 29

Figure 4.6: BE SEM images of the cross-sections (a-e) and surface views (f-j) of BFO thick films sintered at different temperatures between 730 °C and 820 °C.....30

Figure 4.7: BE SEM cross-section images of the BFO/Au/Al_2O_3 structure (a-e) sintered at different temperatures. The cross section of the Au/Al_2O_3 substrate without the BFO thick film, annealed at 750 °C (f).....32

Figure 4.8: The BE SEM image of the Al_2O_3 substrate (sample sintered at 820 °C) (a) and EDXS spectrum taken from the marked region (circle) (b) 33

Figure 4.9: Penetration depth of Bi-rich phase from BFO thick films into Au/Al_2O_3 substrate as a function of sintering temperature determined from BE-SEM cross-sections of BFO/Au/Al_2O_3 structures.....34

Figure 4.10: BE SEM image of the interface between the BFO and Au/Al_2O_3 substrate sintered at 730 °C (a) and EDXS spectrum taken from the circled area as indicated with an arrow (b).....35

Figure 4.11: Schematic illustration of all possible processes taking place during the sintering of BFO thick films.....35

Figure 4.12: XRD patterns of BFO/Ag, BFO/Au and BFO/Pt thick films sintered at 750°C.....36

Figure 4.13: BE SEM images of polished cross-sections (a-c) and surfaces (d-f) of BFO/Ag (a,d), BFO/Au (b,e) and BFO/Pt (c,f) thick films sintered at 750 °C.....37

Figure 4.14: BE SEM image of the polished cross-section of BFO/Ag structure sintered at 750 °C (a). EDXS spectrum of the area highlighted with circle (b) 38

Figure 4.15: BE SEM images of polished cross-sections of BFO/Au (a), BFO/Pt (b) and BFO/Ag (c) thick-film structures sintered at 750 °C for 4 hours and post-annealed at 820 °C for two hours; the inset illustrates an EDXS spectrum taken from the circled area.....39

Figure 4.16: BE SEM image of polished cross-sections of BFO/Ag thick-film structure sintered at 740 °C 40

Figure 4.17: Polarization–electric-field (P-E) hysteresis loop of BFO/Ag structure (sintered at 740 °C) measured at 2.9 kV/cm of field amplitude and 1 Hz of field frequency (a), j-E curve of BFO/Ag film (circles) (b) and, for comparison, j-E curve of BFO ceramics (squares).....41

Figure 4.18:Topography (a) and out-of-plane amplitude PFM image (b) of the bare surface of BFO/Ag structure sintered at 740 °C.....42

Figure 4.19: Out-of-plane amplitude PFM images of the BFO/Ag structure sintered at 740 °C (a,b), PFM hysteresis loop (c) obtained from the area marked by a cross in the out-of-plane PFM image shown in panel (a). The circles in the PFM images illustrate different domain morphologies, i.e., lamellar- (ellipse), wedge- (square) and island-like (circle) domains.....42

Figure 4.20: Mechanical displacement of the BFO thick-film structures sintered at 800 °C (a) and 820 °C (c) as a function of time under an applied sinusoidal voltage. The schematic representations of the BFO thick films sintered at 800 °C (b) and 820 °C (d) indicate the out-of-plane component of the built-in P determined from phase measurements of the direct and converse piezoelectric response. 44

Figure 4.21: XRD patterns of the BFO thick films sintered at 800 °C (a,b) and 820 °C (c,d). The (b,d) panels show the enlarged part of the respective patterns with $\{111\}_{pc}$ peaks.....45

Figure 4.22: *In situ* HT XRD investigation of the BFO thick-film structure sintered at 750 °C. XRD patterns recorded in the heating/cooling cycles in the temperature range 780–810 °C (a) and 780–840 °C (b).....46

Figure 4.23: XRD patterns at RT of the BFO thick-film structure sintered at 750 °C (a,b), BFO thick-film structure sintered at 750 °C and post-annealed at 810 °C (c,d) and sintered at 750 °C and post-annealed at 840 °C (e,f). The (b,d,f) panels highlight an enlarged region with $\{111\}_{pc}$ peaks 47

Figure 4.24:BE SEM images of cross sections and surface views of the BFO thick-film structures sintered at 800 °C (a,c) and 820 °C (b,d) 48

Figure 4.25: EBSD orientation maps of cross-sections (a,b) and surface views (c,d) of the BFO thick films sintered at 800 °C and 820 °C with the corresponding colour-key IPF legend showing Miller Bravais indices for hexagonal symmetry (central inset) 50

Figure 4.26:Out-of-plane amplitude PFM images of polished surfaces of BFO thick films sintered at 800 °C (a) and 820 °C (b) 51

Figure 4.27:BE SEM images of the cross-sections (a,b) and surface views (c,d) of BFO thick-film structure sintered at 750 °C and post-annealed either at 810 °C (a,c) or 840 °C (b,d) 52

Figure 4.28: EBSD orientation maps of cross-section of BFO thick film sintered at 750 °C and post-annealed at 840 °C with the corresponding colour-key IPF legend 52

Figure 4.29:BFO/Pt/Al_2O_3 structure sintered at 820 °C: Low-magnification BF TEM image of the BFO/Pt interface, circles indicate areas where SAED patterns were acquired (a). HR TEM image of BFO grain in the $[110]_{pc}$ zone axis near the film-substrate interface (b); enlarged area showing out-of-plane $(110)_{pc}$ and in-plane $(001)_{pc}$ direction relative to the substrate plane (c). Variation of normalized $(001)_{pc}$ and $(110)_{pc}$ d-values calculated from SAED patterns through the film thickness (d) 54

Figure 4.30:XRD patterns showing $(001)_{pc}$ peak of BFO film with different thickness sintered at 750 °C and post-annealed at 850 °C 55

Figure 4.31:Schematic illustration of the strain-developing mechanism in BFO thick films sintered below (a) or above T_C (b) 57

Figure 4.32:Piezoelectric d_{33} and tanδ of the BFO thick film sintered at 750 °C and post-annealed at 840 °C as a function of the driving-field frequency measured at ~11 kV/cm of field amplitude (a). The d_{33} of the film as a function of the amplitude of the driving field measured at 1 Hz of frequency (b) 58

List of Tables

Table 1.1: Thickness, t, conductivity, σ, remanent polarization, P_r, and coercive field, E_C, of BFO-based thick-film structures from the literature. 13

Table 3.1: List of chemicals and accessories. 17

Table 3.2: Notations for the layered structures. 20

Abbreviations

α-T	. . . α-Terpeneol
AFM	. . . atomic force microscope
BE	. . . backscatter electron
BEA	. . . [2-(2-buthoxyethoxy)ethyl] acetate
BFO	. . . $BiFeO_3$
BF	. . . bright field
CTE	. . . coefficient of thermal expansion
DART-SS	. . . dual ac resonance tracking switching
DC	. . . direct current
EBSD	. . . electron back-scatter diffraction
EC	. . . ethyl cellulose
EDXS	. . . energy-dispersive X-ray spectroscopy
FWHM	. . . full width at half maximum
hex	. . . hexagonal
HR	. . . high resolution
HT	. . . high temperature
IPF	. . . inverse pole figure
KNN	. . . $K_{0.5}Na_{0.5}NbO_3$
LTCC	. . . low-temperature co-fired ceramics
MEMS	. . . micro-electro-mechanical system
MERAM	. . . magneto-electric random access memory
MPB	. . . morphotropic phase boundary
pc	. . . pseudo-cubic
PFM	. . . piezoresponse force microscopy
PMN-PT	. . . $(1-x)(PbMg_{1/3}Nb_{2/3})O_3–xPbTiO_3$
PT	. . . $PbTiO_3$
PZT	. . . $Pb(Zr,Ti)O_3$
rh	. . . rhombohedral
RT	. . . room temperature
SAED	. . . selected-area electron diffraction
SEM	. . . scanning electron microscope
TEM	. . . transmission electron microscope
XRD	. . . x-ray diffraction
YSZ	. . . ZrO_2 stabilized with Y_2O_3

Symbols

d	...	Feret's diameter, μm
d_{33}	...	piezoelectric coefficient, pC/N or pm/V
d_{90}, d_{50}, and d_{10}	...	90th (d_{90}), 50th (d_{50}), and 10th (d_{10}) percentile of the particle size limit, μm
E	...	amplitude of driving electric field, kV/cm
E_C	...	coercive field, kV/cm
e_{CTE}	...	the residual strain related to the difference in coefficients of thermal expansion, %
e_{TR}	...	the residual strain related to phase transition, %
e_{RT}	...	the residual strain at room temperature, %
F	...	electric field frequency, Hz
ΔG°(T)	...	molar Gibbs free energy, kJ/mol
I_o	...	the initial intensity of X-ray, counts
I_L	...	the intensity of X-ray transmitted from the material after passing through the path length L, counts
I_{111}	...	intensity of $(111)_{pc}$ peak of BFO thick film, counts
$I_{11\bar{1}}$	...	intensity of $(11\bar{1})_{pc}$ peak of BFO thick film, counts
I'_{111}	...	intensity of $(111)_{pc}$ peak of BFO ceramic reference, counts
$I'_{11\bar{1}}$	...	intensity of $(11\bar{1})_{pc}$ peak of BFO ceramic reference, counts
j	...	current density, mA/cm^2
L	...	the path length of X-ray, μm
P	...	polarization, $\mu C/cm^2$
P_r	...	remanent polarization, $\mu C/cm^2$
T_C	...	Curie temperature, ^oC
T_N	...	Néel temperature, ^oC
T_{sint}	...	sintering temperature, ^oC
T_{RT}	...	room temperature, ^oC
tanδ	...	tangent of piezoelectric phase angle, /
t	...	thickness, μm
$V_{unit\ cell}$	...	volume of unit cell, $Å^3$
α	...	coefficient of thermal expansion, K^{-1}
ε	...	relative dielectric permittivity, /
η_{111}	...	volume fraction of domains that has reoriented to the $[111]_{pc}$ direction from the random direction, /
Θ	...	incident angle of X-ray, ^{o}
μ/ρ_m	...	mass absorption coefficient of the material, cm^2/g
v_{111}	...	volume fraction of the material with $[111]_{pc}$ oriented domains in an out-of-plane thick-film direction, /
ρ	...	density of the material, g/cm^3
σ	...	specific electrical conductivity, $Ohm^{-1}cm^{-1}$
τ	...	the penetration depth of X-rays, μm
ϕ	...	diameter, mm

Chapter 1

Introduction

1.1 Motivation and Outline

Perovskite bismuth ferrite – $BiFeO_3$ (BFO) – has been the subject of intensive investigations in previous years with hundreds of papers published annually, exploring synthesis issues and the properties of BFO. BFO is a potential candidate for a wide range of applications due to a combination of interesting magnetic, ferroelectric and piezoelectric properties. For example, BFO is at the same time a G-type antiferromagnetic and a ferroelectric at room temperature [1-6], a combination attractive for magneto-electric and spintronic applications, for example, for magneto-electric random access memory (MERAM) devices where the BFO could function as an active layer [7, 8]. The spontaneous polarization of BFO along the $[111]_{pc}$ direction was theoretically predicted and experimentally confirmed to be exceedingly high, ~100 $\mu C/cm^2$ [9, 10]; this property could potentially be used in ferroelectric memory devices [7, 11]. Although BFO exhibits a relatively low piezoelectric d_{33} coefficient, (the maximum reported value for bulk BFO is ~ 60 pm/V [7, 12]), owing to its high Curie temperature (835 ± 10^oC [1-4, 13]), it is still a potential material for developing BFO-based high-temperature piezoelectric ceramics [14-17]. Possessing an optical bandgap of 2.2–2.8 eV [7], BFO was reported to exhibit electro-optical properties such as photoconductivity [18] and the photovoltaic effect [19] and can potentially be used in opto-electronic devices, for example photosensors.

While BFO has been studied intensively in bulk (polycrystalline ceramics) and in thin films (thickness (t) < 1 μm), few reports have been published on the preparation and properties of BFO thick films ($t > 1$ μm). Studies on the integration of BFO onto substrates as thick films are particularly important at this stage as they would provide the key step towards applications for BFO, e.g., in micro-electro-mechanical systems (MEMS) [20]. Especially in the case of BFO, however, the integration is demanding and not straightforward due to the readily occurring chemical reactions between the BFO layer and the electrode/substrate. In addition, differences in the coefficients of thermal expansion of the film and the substrate can lead to stresses in the films, which can diversely affect the structure, microstructure and thus the functional response.

After a short survey of the crystal structure of BFO, in the introduction part of the thesis the major problems that must be taken into account in order to prepare defect-free, phase-pure BFO thick films are presented. As the preparation of BFO is known to be difficult, the thermodynamic and kinetics aspects of the solid-state processing of BFO are explained and discussed. Next, the preparation of thick-film structures with the emphasis on screen-printing is described and the key factors, such as chemical reactions between layers and stress development are addressed. The literature review of BFO-based thick films concludes the introduction part of the PhD thesis.

1.2 $BiFeO_3$

1.2.1 Crystal structure of $BiFeO_3$

1.2.1.1 Crystal structure at room temperature

The room-temperature $BiFeO_3$ (BFO) phase possesses a rhombohedrally distorted perovskite crystal structure, which is described by the R3c # 161 space group [1, 21, 22]. The structure can be represented with three different crystallographic lattice settings: hexagonal (hex) (Fig. 1.1a), rhombohedral (rh) (Fig. 1.1b), and pseudocubic (pc) (Fig. 1.1c), in which each unit cell contains six, two and one formula units of BFO, respectively. The unit-cell parameters are a_{hex}=5.579 Å, c_{hex}=13.869 Å for the hexagonal setting; a_{rh}=5.634 Å, α_{rh}=59.35° for the rhombohedral setting; and a_{pc}=3.965 Å, α_{pc}=89.35° for the cubic setting [1, 21, 22]. The geometrical relationship between these three lattice settings is illustrated in Fig. 1.1d; the $[0001]_{hex}$ direction in the hexagonal notation is parallel to the $[111]_{pc}$ direction in the pseudocubic and to the $[111]_{rh}$ in the rhombohedral notation.

The rhombohedral (R3c) structure of BFO can be derived from the ideal cubic ($Pm\bar{3}m$) perovskite (ABO_3) structure. In the ideal perovskite, oxygen atoms are located in the center of each cube face, forming a corner-sharing chain of BO_6 octahedra. Compared to the ideal cubic perovskite, the FeO_6 octahedra in the R3c structure (marked in pale yellow in Fig. 1.1) are out-of-phase tilted along the $[111]_{pc}$ (or $[0001]_{hex}$ or $[111]_{rh}$) direction (the tilt direction is marked with green arrows in Fig. 1.1b,c). Another difference compared to an ideal perovskite is that the Bi and Fe cations are shifted along the $[111]_{pc}$ (or $[0001]_{hex}$ or $[111]_{rh}$) direction (the shift is marked with blue and orange arrows in Fig. 1.1b,c). [23]

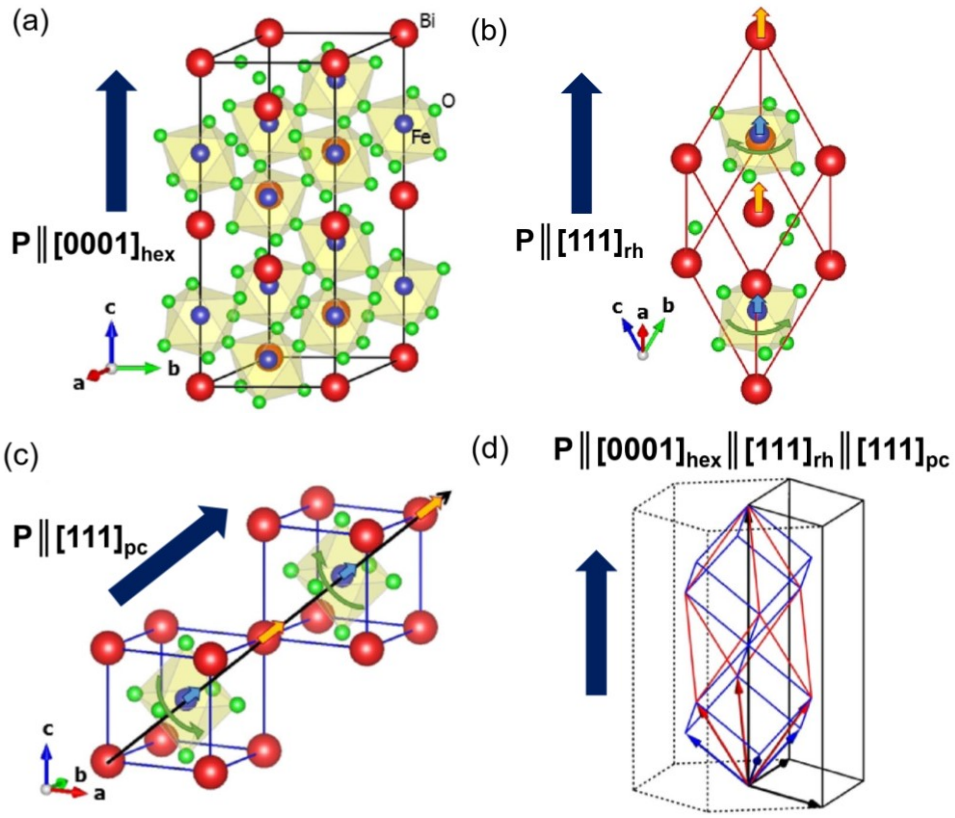


Figure 1.1: Representation of rhombohedral, R3c, $BiFeO_3$ crystal structure in hexagonal (a), rhombohedral (b) and pseudocubic (c) crystallographic settings, and the geometrical relationship between the different settings (d). Redrawn from [23]. Dark blue arrows mark the direction of polarisation (P).

The octahedral tilting (or anti-ferrodistortive rotation) is represented by the rotation angle, ω, which for BFO is 11–14° [1, 21, 24]. This parameter is directly related to the Fe–O–Fe bond angle, θ, which is 154–155° [21, 24], thus smaller than 180° from the ideal perovskite. The θ parameter is an important characteristic since it defines both the magnetic exchange and the overlap between the Fe 3*d* orbitals and the O 2*p* orbitals, and as such it determines the magnetic and electronic properties of BFO.

The shifts of the cations (Bi, Fe) in BFO, relative to the oxygen octahedra, result in the ferroelectric distortion. The distortion is explained by the presence of a stereochemically active lone pair of Bi, which causes an asymmetric bonding between the Bi and the O [25, 26]. This is reported to be responsible for the off-centering displacement of the Bi atoms with respect to the oxygen sublattice. The displacement of Bi atoms causes a cooperative displacement of Fe atoms due to the electrostatic repulsion, resulting in a finite electric polarization (P) of BFO.

1.2.1.2 Crystal structure at increased temperature or pressure

The temperature-induced expansion of the R3c BFO unit cell is reported to be non-linear and anisotropic [2, 3, 24, 27-29] where the expansion along the c_{hex}-axis is larger than that along the a_{hex}-axis [2, 27]. The measured change in the BFO unit-cell volume in the 25–800 °C temperature range is 0.004% K^{-1} [13, 30], corresponding to a linear thermal expansion coefficient of $\sim 13.3 \times 10^{-6}$ K^{-1}.

BFO with the R3c structure at room temperature is known to undergo several phase transitions with increasing temperature: (i) a magnetic transition from the G-type antiferromagnetic state to the paramagnetic state at the Néel temperature, $T_{N,}$ ~370°C [1, 5, 6], (ii) a transition from the ferroelectric to the paraelectric phase (α-β phase transition) at the Curie temperature, $T_{c,}$ 835 ± 10°C [1-4, 13], which is followed by (iii) β-γ transition near 930 °C [3, 13, 31]. With a further increase in temperature, γ-BFO peritectically decomposes into a liquid phase and $Bi_2Fe_4O_9$, and eventually into a liquid phase and Fe_2O_3 The phase transitions are illustrated in the marked region (dashed rectangle) of the Bi_2O_3–Fe_2O_3 phase diagram in Fig. 1.2a [13, 31]. The α-β phase transition is reported to be strongly first order with a drastic change in the unit-cell volume (~1.5%) and a clear hysteresis in the calorimetry data [3, 4, 13, 30, 31]. The unit-cell symmetry of the paraelectric β phase has been the subject of debates and was suggested to be one of $Pm\bar{3}m$ [32], I4/mcm [33], C2/m [33], $P2_1/m$ [31], $R\bar{3}c$ [30], or Pbnm [4]. It has been proposed by different research groups that the high-temperature γ phase has either cubic ($Pm\bar{3}m$) [13] or orthorhombic (Pbnm or Imma)[34] symmetry.

At room temperature, the crystal structure of BFO changes with applied pressure (hydrostatic). In comparison with the temperature-induced BFO transformations, these changes have been less investigated. The temperature–pressure phase relations are presented in the diagram (Fig. 1.2b) proposed by Catalan and Scott [7], which was later revised by Guennou *et al.* (Fig. 1.2b) [35]. At room temperature, the R3c structure of BFO is stable up to ~4 GPa (region marked in orange in Fig. 1.2b). With a further increase of pressure from ~4 GPa to ~11 GPa different phases possessing orthorhombic and monoclinic symmetry were observed. Let us note that in the case of non-hydrostatic (uniaxial) pressure an even larger number of new phases were suggested to form between 4 GPa and 11 GPa [36]. In the pressure range from ~11 GPa to ~38 GPa the orthorhombic Pnma phase is stable (region marked in blue in Fig. 1.2b). At ~38 GPa, the Pnma orthorhombic phase changes to Pnmm, which then at ~48 GPa changes to Cmcm [35]; this last phase transition is associated with the insulator-to-metal phase transition. Similar phase transitions were observed by Zhang *et al.* [37].

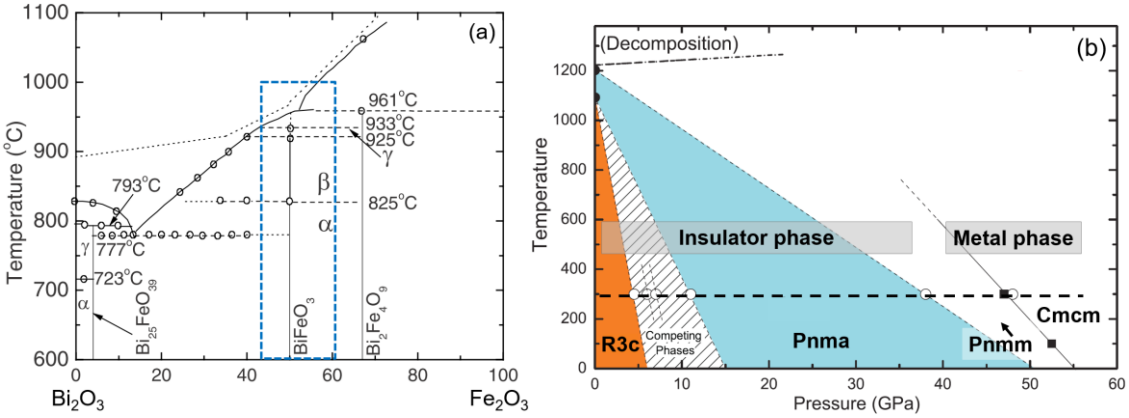


Figure 1.2: Temperature-induced or hydrostatic-pressure-induced phase transitions in rhombohedral, R3c, BFO. Bi_2O_3–Fe_2O_3 phase diagram, redrawn from [13] (a); schematic pressure-temperature phase diagram of BFO, redrawn from [35] (b); open and solid symbols represent the experimental points, while the horizontal dashed line marks room temperature.

1.2.2 $BiFeO_3$ ceramic processing issues

The preparation of phase-pure BFO ceramic is challenging as undesired, secondary, non-perovskite phases can easily form during its synthesis. As shown in Fig. 1.2a, in addition to the rhombohedral (R3c) perovskite $BiFeO_3$, two non-perovskite compounds are present in the Bi_2O_3–Fe_2O_3 phase diagram [13], i.e., orthorhombic mullite – $Bi_2Fe_4O_9$ (Pbam), and cubic sillenite – $Bi_{25}FeO_{39}$ (I23). As will be explained in the following, the main reasons for the frequently observed three-phase coexistence (perovskite phase and the two secondary phases) are the thermodynamic stability of BFO [3, 38], the sensitivity of BFO to impurities [39], the reaction kinetics between Bi_2O_3 and Fe_2O_3 [40] and the evaporation/sublimation of bismuth [41].

1.2.2.1 Thermodynamic aspects

The reaction leading to the formation of BFO from its constituent oxides is described by the following equation:

$$1/2\ Bi_2O_3 + 1/2\ Fe_2O_3 \rightarrow BiFeO_3 \qquad (1.1)$$

Mikhailov and co-workers [42] calculated the Gibbs free energy for this reaction ($\Delta G°(T)$) for different temperatures, and found $\Delta G° = -12.7$ kJ/mol for 777 °C and $\Delta G° = -9.4$ kJ/mol for 827 °C. The authors thus showed that the driving force for the BFO formation decreases with increasing temperature [42]. They suggested that the temperature for the solid-state synthesis of BFO from simple oxides should not exceed the temperature of the phase transition α-$Bi_2O_3 \rightarrow \beta$-$Bi_2O_3$ (that is at 727 °C), since the Gibbs energy is drastically reduced by the high entropy of β-Bi_2O_3 [42]. Thus, 720 °C is proposed as the optimum temperature for the synthesis.

A number of authors experimentally observed that BFO, in the form of powder [43, 44], ceramic [41] or single crystal [13], becomes unstable during sintering at elevated temperatures. Selbach and co-workers investigated the thermodynamic stability of BFO ceramics [38] from both the experimental and theoretical aspects. Using high-temperature, in-situ X-ray diffraction (XRD) analysis, the authors showed that a pre-synthesized BFO decomposes to the mullite and sillenite phases in the temperature range between ~600 °C and ~820 °C. With a further increase of the temperature to ~870 °C, both the mullite and sillenite phases disappeared. (Fig. 1.3a). To explain these results, the authors used the available thermodynamic data, i.e., the standard enthalpies of formation and the heat

capacities for the BFO, $Bi_2Fe_4O_9$ and $Bi_{25}FeO_{39}$, [45] and calculated ΔG°(T) for the equilibrium reaction:

$$1/49\ Bi_{25}FeO_{39} + 12/49\ Bi_2Fe_4O_9 \leftrightarrow BiFeO_3 \quad (1.2)$$

The results of the calculations are shown in Fig. 1.3b. The slightly positive value of ΔG°(T) between 447 and 767 °C indicated that in this temperature interval BFO will tend to decompose to the secondary phases. Although in strict thermodynamic terms, the coexistence of all three phases is possible only at 447 °C and 767°C where the ΔG°(T) of the reaction (1.2) is zero [38], the experimentally observed coexistence of all three phases, in a broader temperature range [12, 43, 44], can be explained by the small driving force of the forward and backward reactions (1.2). In addition to the effect of temperature, Selbach *et al.* [38] also discussed the influence of the pressure on the equilibrium reaction (1.2), showing that pressure will favour the formation of a close-packed perovskite rather than the mullite and sillenite phases.

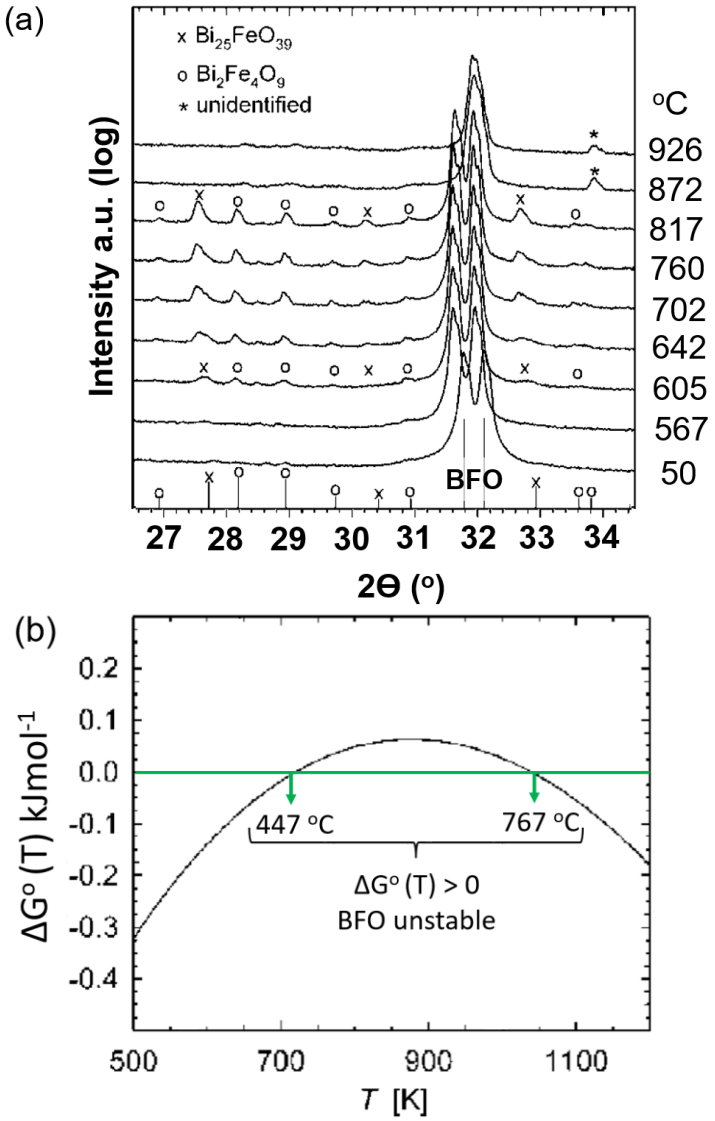


Figure 1.3: XRD patterns of BFO at different sintering temperatures (a). Redrawn from [38]. Calculated temperature dependence of the Gibbs free energy (ΔG°(T)) of the reaction 1.2 (b). Redrawn from [38].

Reactions 1.1 and 1.2 can also be greatly influenced by impurities, a minor amount of which can be easily introduced during the BFO synthesis from, e.g., the starting powders or during milling or homogenization of the powders (through wear of the milling media). As explained by Valant *et al.* [39], this results in a three-component system Bi_2O_3–Fe_2O_3–AO_x, where AO_x represents the impurity oxide, for example, Al_2O_3, SiO_2 or TiO_2. For the case of the SiO_2 impurity, the proposed Bi_2O_3–Fe_2O_3–SiO_2 ternary phase diagram is illustrated in Fig. 1.4a [39]. It becomes evident from this diagram that the incorporation of a small amount of SiO_2 in the Bi_2O_3–Fe_2O_3 system will shift the composition into a three-phase field (Fig. 1.4a, inset), resulting in the coexistence of the sillenite, mullite and BFO phases. Valant and co-workers [39] also experimentally confirmed that a small amount (<1 wt%) of selected impurities (SiO_2, Al_2O_3 and TiO_2) results in large volume fractions of the sillenite and mullite phases in coexistence with the perovskite; for example, the addition of 0.5 wt% of SiO_2 results in ~13 vol% of sillenite, ~30 vol% of mullite and only ~58 vol% of BFO (Fig. 1.4b).

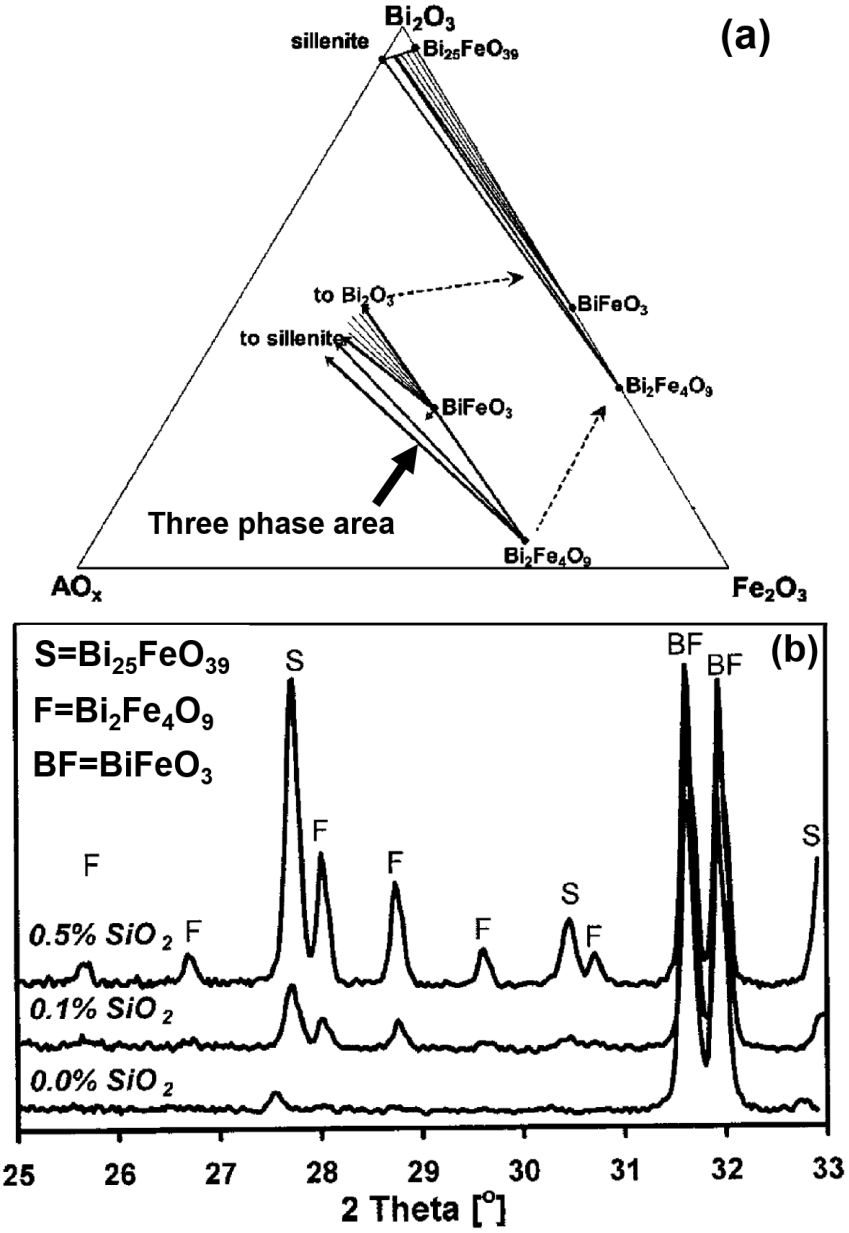


Figure 1.4: Proposed phase relations in the ternary Bi_2O_3–Fe_2O_3–AO_x system where AO_x is SiO_2. (a); XRD patterns of pure Bi_2O_3–Fe_2O_3 mixture and with 0.1 and 0.5 wt% additions of SiO_2 sintered at 800 °C for 5 h in air (b). Redrawn from [39].

1.2.2.2 Reaction kinetics, bismuth evaporation and segregation of sillenite phase

The reaction kinetics of the Bi_2O_3–Fe_2O_3 solid-state system was investigated by Bernardo *et al.* [40] using diffusion couples (reactions were studied at 650 °C). The authors observed that Bi diffuses faster into Fe_2O_3 compared to the diffusion of Fe into Bi_2O_3. The proposed reaction pathway mechanism for the solid-state synthesis of BFO from Bi_2O_3 and Fe_2O_3 (reaction 1.2) is illustrated in Fig. 1.5. At the beginning of the reaction, the sillenite, $Bi_{25}FeO_{39}$, phase is formed at the Fe_2O_3–Bi_2O_3 grain contacts. Further diffusion of Bi into Fe_2O_3 results in the formation of the perovskite BFO between the $Bi_{25}FeO_{39}$ and the Fe_2O_3 core and subsequently in the formation of the mullite, $Bi_2Fe_4O_9$, phase between the BFO and Fe_2O_3 core. The phase sequence is $Bi_{25}FeO_{39}/BiFeO_3/Bi_2Fe_4O_9/Fe_2O_3$, which is frequently observed in the microstructure of sintered BFO ceramics [40, 12].

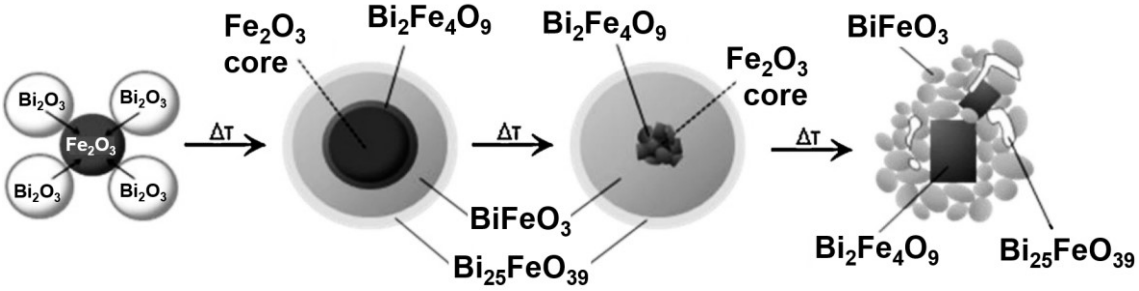


Figure 1.5: Schematic representation of the reaction mechanism for the solid-state synthesis of BFO from Bi_2O_3 and Fe_2O_3. Redrawn from [40].

According to the proposed reaction mechanism, once the mullite ($Bi_2Fe_4O_9$) crystals are formed, they become very stable and are difficult to remove. As a consequence, the formed BFO may coexist with kinetically stabilized sillenite and mullite phases. The study thus suggests that it is the length of the reaction path, which is determined by the size of the starting iron oxide particles, that should be carefully controlled in order to avoid kinetic stabilization of the secondary phases along with the BFO.

In addition to the reaction kinetics, another problem that may occur during the synthesis of BFO is the melting (peritectic decomposition) of the sillenite phase at elevated temperatures, which can lead to the segregation of this phase and to an uncontrolled evaporation of the bismuth (in the form of Bi(g) [42] and/or Bi oxides(g) [3, 42]) from the melt, resulting in local inhomogeneities and a loss of stoichiometry. This issue was investigated by Rojac and co-workers [12] (Fig. 1.6). Fig. 1.6a shows a scanning electron microscope (SEM) image of a BFO ceramic sample sintered at 760°C (i.e., below the sillenite peritectic decomposition, which is~790 °C [13]). The ceramic sample contains BFO as a main phase and well distributed μm-sized inclusions of the sillenite phase (bright spots in Fig. 1.6a). Next, the BFO ceramic sample was post-annealed at 820 °C (above the sillenite peritectic decomposition) for an extended time (>10 hours) with (Fig. 1.6b) and without (Fig. 1.6c) the BFO packing powder. The packing powder was used to provide an atmosphere during sintering enriched with bismuth/bismuth oxide vapours and thus to prevent the evaporation of bismuth from the sillenite phase. In the case when the packing powder was used, inclusions of the sillenite phase of up to 10 μm in size were observed in the BFO ceramic (Fig. 1.6b). In contrast, only a small amount of the sillenite phase was observed in the ceramic that was post-annealed without the packing powder (Fig. 1.6c), indicating that the evaporation of bismuth from the sillenite phase took place. At higher post-annealing temperatures (880 °C), this evaporation was even more pronounced as no sillenite phase was detected. Instead, large (50 μm) grains of the mullite phase were observed (Fig. 1.6d). This observation suggests the shift of the composition into the $BiFeO_3$–$Bi_2Fe_4O_9$ phase region of the Bi_2O_3–Fe_2O_3 phase diagram (see Fig. 1.2a) due to bismuth oxide losses.

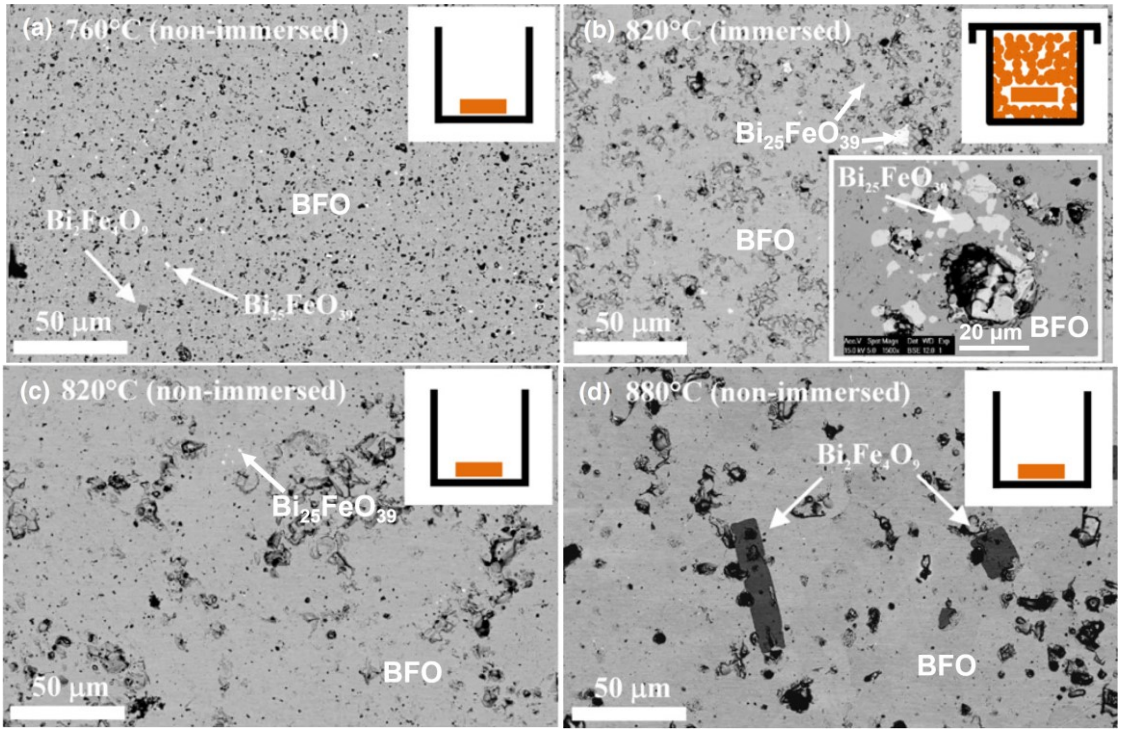


Figure 1.6: SEM images of BFO ceramics sintered at 760°C for 6 h in air (marked "non-immersed") (a), sintered at 820°C for 10 h and additionally post-annealed for 10 h at 820 °C in a BFO packing powder (marked "immersed") (b), at 820°C in air (c) and at 880°C in air (d). Redrawn from [12].

1.3 Thick-Film Technology

Micro-electro-mechanical systems (MEMS) are miniature devices with characteristic dimensions between 1 mm and 1 μm [20] that interconvert physical quantities and electrical signals, and can be used in motion, pressure and force sensors, small actuators, acoustic and ultrasonic devices, and resonators. Many MEMS applications use piezoelectric thick-film structures as one of the fundamental parts. Such a piezoelectric thick-film structure is a three-dimensional structure, which in its simplest form consists of a substrate, a bottom electrode, a piezoelectric material layer and a top electrode [46] (schematically shown in Fig. 1.7).

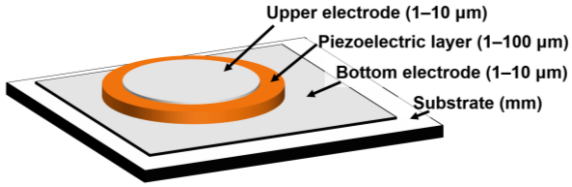


Figure 1.7: Schematic representation of a piezoelectric thick-film structure.

The production of thick-film structures can be realized with a top-down or bottom-up approach. In the first case, the prepared bulk ceramic is reduced in dimensions by cutting, grinding and polishing. Finally, the thin components are assembled. This approach involves a lot of waste material as well as high costs. Furthermore, the dimensions of the components are limited to those of primitive shapes, such as disk, plate, ring and cylinder.

With the bottom-up method, the structure is built up on the substrate with the following consecutive preparation steps [46]: i) synthesis of the ceramic powder, ii) mixing of the powder with an organic component, iii) deposition of the mixture on the substrate using various techniques and iv) sintering of the structure. The approach provides a time- and cost-effective way to produce thick-film structures without any shape limitations. The final thick-film structure is also more reliable due to easy handling and less mechanical processing.

The preparation of the ceramic powder is a crucial factor for processing a high-quality thick-film structure. The powder may be prepared by several methods, including conventional solid-state synthesis, mechanochemical synthesis, hydrothermal synthesis or coprecipitation synthesis. The prepared powder is deposited onto the substrate using a variety of methods [46], which may be divided into so-called low- and high-density deposition methods. The low-density methods include screen-printing, tape casting, electrophoretic deposition, and inkjet printing. The high-density methods include jet printing, aerosol deposition, and airflow deposition. Thick films with smaller thicknesses (from 1 to 10 μm) can be prepared by chemical solution deposition methods, such as multi spin or dip coating, and an adapted thin-film method, in which the solution precursor is modified with nano-sized particles of the chosen composition in order to increase the solids load.

1.3.1 Screen-printing

Among the deposition methods, screen-printing is the most widely used thick-film deposition technique. The method is reliable and relatively simple; it can be used for printing any material, on any substrate, in a wide range of size or thickness, and in almost any shape. Being cost-effective, screen-printing can be used for the deposition of large, accurate quantities of material with well-defined dimensions required for the fabrication of thick films [47]. Fig. 1.8 illustrates the five basic stages of the screen-printing technique. A cleaned substrate is first placed on the substrate holder (step I), and then the patterned screen is placed over the substrate (step II). In the next step, the squeegee with the paste is moved across the screen area to push the paste through the screen onto the substrate (step III). The screen is then lifted off (step IV) and the deposited layer is finally left for levelling

at room temperature (step V). Step V is typically followed by drying. In order to achieve the needed thickness of the film, steps I-V are repeated several times before the material is densified at elevated temperatures.

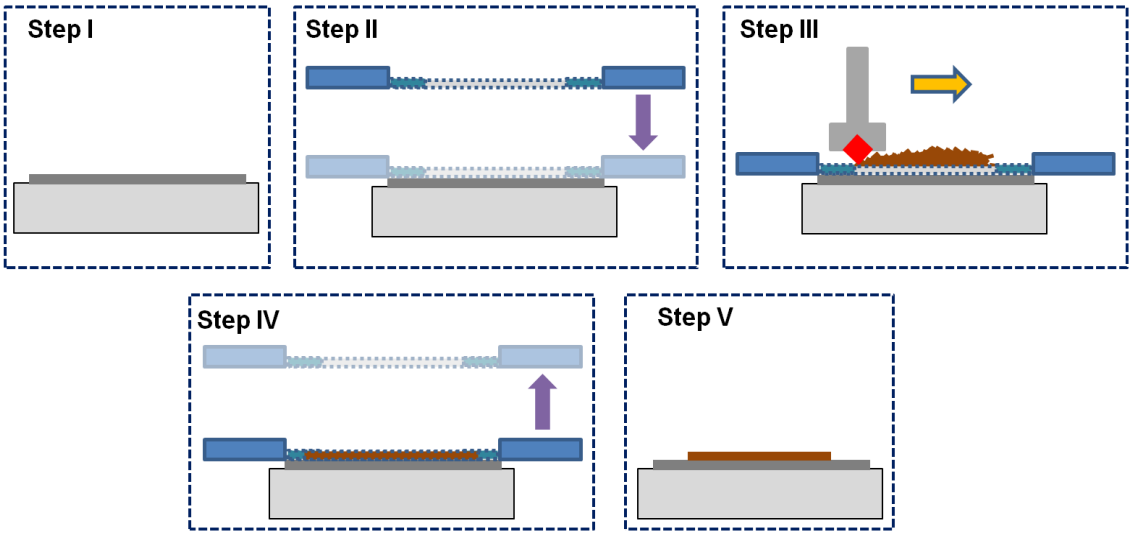


Figure 1.8: Schematics of the processing steps for the screen-printing of thick films.

The paste for screen-printing is prepared from fine powders of the desired chemical composition mixed together with an organic vehicle, which consists of different organic binders and carriers. A proper composition of the organic vehicle ensures suitable printability of the paste and preparation of defect-free thick-film structure. The formulation of the paste is probably the most challenging step in the screen-printing process and requires an extensive knowledge of rheology [48, 49].

1.3.2 Thick-film processing issues

The preparation of thick-film structures with defect-free, dense, and single-phase active layers is challenging. Sintering of thick polycrystalline films typically requires elevated temperatures; depending on the material, these temperatures may be as high as 1100 °C [50]. During the sintering, the thick film is in direct contact with a chemically different material – the substrate. A critical issue in thick-film processing is to ensure a good chemical compatibility between the different materials, which is important to avoid interface reactions and thus to provide a good adhesion between the layers. The literature provides comprehensive studies on chemical reactions between Pb-based ferroelectric layers, such as $Pb(Zr,Ti)O_3$(PZT), [51-55] $(Pb,La)(Ti,Zr)O_3$, [50] and $Pb(Mg_{1/3}Nb_{2/3})O_3$–$PbTiO_3$ [56, 57], and different substrate materials, such as silicon [51-53, 56], polycrystalline Al_2O_3, [50, 56] low-temperature co-fired ceramics [54, 55], and platinum [57]. It has been shown in these studies that the interface reactions, resulting in compositional variations and the formation of secondary phases between the thick-film structure layers, can deteriorate the functional properties of the active layer. The interdiffusion between the layers can be minimized, preventing the deterioration of the properties by introducing a barrier layer between the thick film and the substrate; for example, Al_2O_3 [54] and Au [58] barriers were introduced between PZT films and a low-temperature co-fired ceramics (LTCC) substrate.

In addition to the interface reactions, the densification of thick films is different from the isotropic densification of bulk ceramics due to sintering in the constrained conditions associated with the clamping of the films onto the substrate [59, 60].

Besides chemical reactions, which can occur between the active layer and the substrate, the substrate may introduce stresses in the film during the processing [61], as a result of either a lattice and/or a thermal expansion mismatch between the layer and the substrate. These stresses may relax through different mechanisms, for example, through a change in the crystal's unit-cell parameters [62] and the crystallographic orientation of the active layer [63] or a shift of the morphotropic phase boundary [64, 65], all of which may have a

marked effect on the final functional properties of the films. Some examples are described in the following.

Pavlic *et al.* [63] reported on preferentially oriented $K_{0.5}Na_{0.5}NbO_3$ (KNN) thick films deposited on platinized Al_2O_3 substrates. The preferred crystallographic orientation of the KNN films was attributed to compressive stresses, resulting from the mismatch between the coefficients of thermal expansion (CTE) of the KNN film and the alumina substrate. Hiramatsu *et al.* [62] investigated GaN thick films grown on sapphire substrates. Depending on the thickness of the GaN films, the stresses relaxed through a lattice deformation or through the generation of micro/macro cracks and dislocations. Finally, Han *et al.* [66] investigated the influence of different substrates on the $Pb(Zr_{0.52}Ti_{0.48})O_3$ (PZT) thick-film properties. Based on an XRD analysis, they showed that the PZT film deposited on Si, sapphire and YSZ substrates exhibited tensile (~120 MPa), weak compressive (~132 MPa), and strong compressive (~271 MPa) in-plane stresses, respectively, which were attributed to the mismatch between the CTEs of the film and the substrates (Fig. 1.9). The highest piezoelectric response was measured on the PZT film deposited on the YSZ substrate and was attributed to easier domain alignment due to the largest compressive stresses in the film (Fig. 1.9).

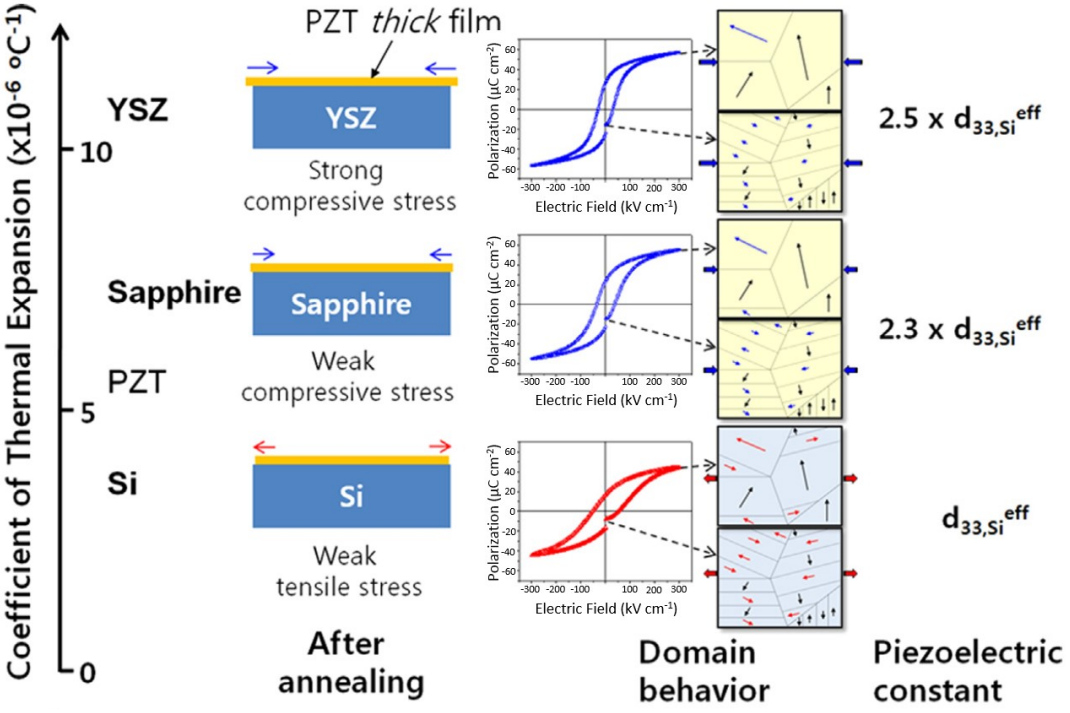


Figure 1.9: Influence of thermal stress on the piezoelectric performance of PZT thick films deposited on silicon, sapphire and YSZ substrates. Redrawn from [66].

If a thick film possesses a complex morphotropic phase boundary (MPB) composition, stresses in the thick films may shift the MPB composition, as was shown by Ursic *et al.* [64, 65]. The authors studied the influence of different substrate materials (for example $Pt/PZT/Al_2O_3$ (see Fig. 1.10a), and Pt/AlN (see Fig. 1.10b)) on the microstructure, phase composition and properties of $0.65Pb(Mg_{1/3}Nb_{2/3})O_3–0.35PbTiO_3$ (0.65PMN–0.35PT) thick films. The 0.65PMN–0.35PT thick films on alumina substrates (Fig. 1.10a), where compressive stresses were expected, had a larger density and grain size compared to the films on the AlN substrate (Fig. 1.10b), where tensile stresses were expected. In addition, XRD analyses revealed the 0.65PMN–0.35PT thick film on the alumina substrate (Fig. 1.10a) consisted of a tetragonal and monoclinic phase, while the film on the AlN substrate was monoclinic (Fig. 1.10b). The changes in the microstructure and phase composition were reflected in the dielectric properties, i.e., the 0.65PMN–0.35PT thick films under compressive stresses exhibited an-order-larger values of the dielectric permittivity (~3600) compared to those under tension (~300) [64, 65].

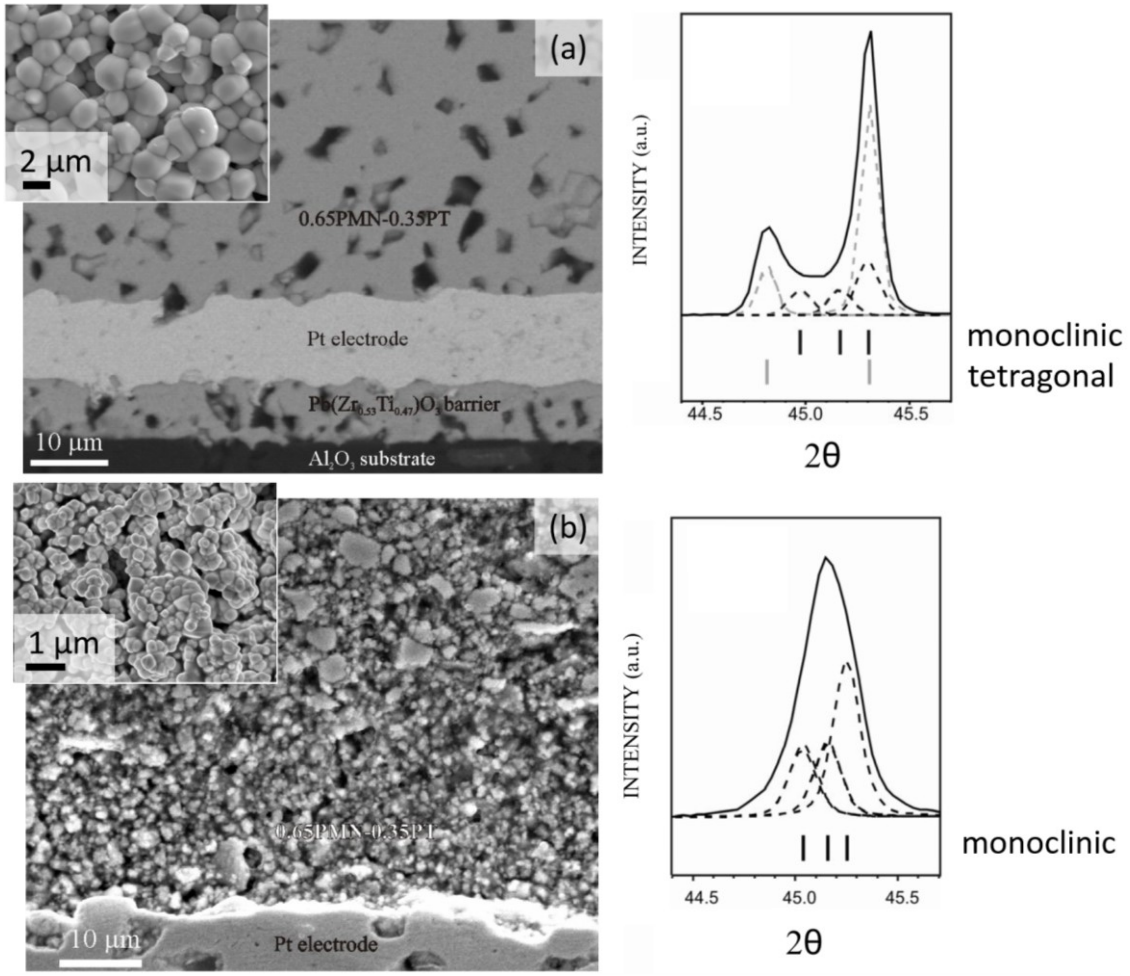


Figure 1.10: SEM cross-section images with corresponding XRD patterns of 0.65PMN–0.35PT thick films on Pt/PZT/Al_2O_3 (a), and on Pt/AlN substrates (b). Both thick films were sintered at 950 °C for 2 h. Insets show SEM surface images of each film. Redrawn from [65].

Thermal stresses can also shift the Curie temperature of the ferroelectric thick films as observed in [63-65]. For example, a large, 50 °C upshift of T_C was reported in $PbTiO_3$ thick films on silicon substrates [67].

Another mechanism of thermal-stress relaxation is the development of built-in polarization, meaning that the films can exhibit a macroscopic poled state after the processing, without being exposed to electric fields [68-72]. This phenomenon is known as the self-poling effect. While self-poling was frequently observed in thin films [73, 74], bulk ceramics [75, 76] and single crystals [77, 78], it was less often investigated in thick films. For example, a weak self-poling effect was observed in 30-μm-thick KNN films on Al_2O_3 substrate [79] and in ~1-μm-thick PZT films [80, 81]. It should be noted that the mechanisms leading to the self-poling effect can be multiple and are in general not well understood. Many factors can influence the magnitude and direction of the built-in polarization, such as Schottky barriers [82], defective surface or interfaces [78, 83], chemical compositions [73, 84, 85] and strain gradients [68-72], [86-89].

1.4 $BiFeO_3$-Based Thick Films

The first report on a BFO-based thick film was by Rao *et al.* [90] in 1991, where radio-frequency magnetron sputtering was used to deposit the films onto glass and silicon substrates. The composition was based on a BFO–$PbZrO_3$ solid solution and the resulting 1.4-μm-thick films were amorphous with promising magnetic properties. Since this early report, little has been reported on BFO-based thick films with approximately twenty publications in the past fifteen years, which include studies on thick films based on BFO-$Ba(Cu_{1/3}Nb_{2/3})O_3$ [91], BFO-$BaTiO_3$ [92] and BFO-$PbTiO_3$ [93] solid solutions.

The available publications (collected in Table 1.1) reveal an eclectic use of substrate, composition and synthesis method. The deposition methods reported are numerous: liquid-phase epitaxial growth [94], electrophoretic deposition [95], hydrothermal epitaxy methods [96], aerosol deposition [97], wet chemical route [98-101], and pulsed laser deposition [102]. The results of these studies do not provide insights into the relationships between the properties and the key parameters, which are substrate, composition and synthesis method. In addition, the measured properties of the various thick films vary widely, as illustrated in Table 1.1.

Choosing the appropriate substrate, particularly in the case of BFO-based thick films, is of great importance due to the high sensitivity of BFO to impurity elements [39] and the film-substrate interactions that can occur. Chemical reactions between BFO films and the substrate can be particularly detrimental to the BFO film because, for example, Al_2O_3 may easily stabilize the mullite ($Bi_2Fe_4O_9$) phase, SiO_2 is known to stabilize the sillenite ($Bi_{25}FeO_{39}$) phase [39], Pt reacts with metallic Bi above 250 °C [103] and bismuth-oxide-based thin films react with Pt electrodes at 800 °C forming Bi_2Pt. [104]

In addition to the substrate, the deposition technique can also have a critical impact on the film properties, such as density, adhesion between layers and residual stresses. It is thus not possible to establish a clear relationship between the thick film's properties and any of these critical parameters without a rigorous and systematic approach. No such study has yet been performed for BFO thick films. It is also important to note that the data presented in Table 1.1 do not assist with the identification of key factors that can be used to improve the BFO-based thick film's quality and properties on a broader basis. As a result, there is a need for systematic evidence of how the substrate material and synthesis method affect the BFO thick-film structure, phase composition, density and, consequently, its functional properties, such as the piezoelectric response.

Table 1.1: Thickness, t, conductivity, σ, remanent polarization, P_r, and coercive field, E_C, of BFO-based thick-film structures from the literature.

Structure: Active layer/Substrate	t, μm	σ, $Ohm^{-1}cm^{-1}$	P_r, $\mu C/cm^2$; E_C, kV/cm;	Ref.; year
(001)$BiFeO_3$/$SrTiO_3$	35.0	/	/; /;	[94] 2008
$BiFeO_3$/steel	12.0	$\sim10^{-9}$	/; /;	[95] 2013
(001)$BiFeO_3$/$SrRuO_3$/$SrTiO_3$	2.0	$\sim10^{-9}$	20.0; 25.0;	[96] 2013
$BiFeO_3$/Pt/Si	5.0	/	/; /;	[97] 2010
$BiFeO_3$/glass	10	$\sim10^{-10}$	/; /;	[98] 2010
(110)$BiFeO_3$/ITO/glass	1.2	/	/; /;	[99] 2006
$Bi_{0.95}La_{0.05}FeO_3$/$LaNiO_3$/Si	1.4	$\sim10^{-10}$	61.0*; 498.0*;	[100] 2014
(110)$Bi_{0.9}La_{0.1}FeO_3$/ITO/glass	1.2	/	42.9*; 200.0*;	[101] 2016
$BiFe_{0.9}Co_{0.1}O_3$/Pt/ Si	1.0	$\sim10^{-10}$	59.0*; 430.0*;	[102] 2011

* P_r and E_C values are likely exaggerated due to the leakage current's contribution

Chapter 2

Aims and Hypothesis

The goals of the dissertation are:

- To *identify the key parameters* that need to be controlled to obtain high-quality $BiFeO_3$ thick films in terms of phase composition and microstructure.
- To understand the *interactions between the substrates and the films* and thus be able to tailor the properties of BFO films.
- To study the electrical and electro-mechanical properties of optimized BFO thick films.

The hypotheses of the dissertation are:

- Sintering conditions and substrate materials are the key factors influencing diffusion processes, interface reactions, densification, phase composition and crystal structure, and therefore the final functional properties of BFO thick films.
- To avoid the stabilization of secondary phases through the incorporation of impurities into the films, high-purity electrodes and substrate materials are required.
- Thermal stresses due to differences in the thermal expansion coefficients between BFO and the substrate can be used to alter the BFO film's properties (such as crystallographic orientation and microstructure).
- Unlike other ferroelectrics (such as $(Pb,Zr)TiO_3$ and $BaTiO_3$), BFO can be sintered both below and above the ferroelectric-paraelectric phase transition ($T_C \sim 825$ °C). Considering that this transition is accompanied by a large change in the lattice volume, we expect an effect of stresses on the properties of films that are cooled from above the ferroelectric-paraelectric phase transition.

Chapter 3

Materials and Methods

3.1 List of Chemicals and Accessories

Table 3.1: List of chemicals and accessories.

Chemical	Specifications, producer	Role
Bi_2O_3	99.999%, Alfa Aesar, Ward Hill, Massachusetts, USA	Powder reagent
Fe_2O_3	99.998%, Alfa Aesar, Ward Hill, Massachusetts, USA	Powder reagent
Ethanol	Ethanol absolute, anhydrous, Carlo Erba Reagents, Val de Reuil, France	Milling medium
Isopropanol	99.9%, Carlo Erba Reagents, Val de Reuil, France	Solvent
[2-(2-buthoxyethoxy)ethyl] acetate (denoted as BEA)	⩾98% Merck Schuchardt OHG, Hohenbrunn, Germany	Dispersing agent, plasticizer, solvent
α-Terpeneol (denoted as α-T)	⩾98% Merck Schuchardt OHG, Hohenbrunn, Germany	Solvent
Ethyl cellulose (denoted as EC)	48.0 – 49.5% ethoxyl, Sigma Aldrich, St. Louis, Missouri, USA	Binder
Al_2O_3	Dimensions: 12 mm × 12 mm × 0.6 mm; 99.6%, A-493 Kyocera, Neuss, Germany	Substrate
Au paste	8884-G, fritless, ESL, King of Prussia, Pennsylvania, USA	Paste for bottom electrode
Pt paste	E1192, Ferro Electronic Packaging Materials, Mayfield Heights, Ohio, USA	Paste for bottom electrode
Ag paste	Flash Dry Silver Paint, Structure Probe Inc., West Chester Pennsylvania, USA	Paste for upper electrode
Ag foil	Dimensions: 10 mm × 10 mm × 0.5 mm; 99.9% Zlatarna Celje, Celje, Slovenia	Substrate
Au foil	Dimensions: 10 mm × 10 mm × 0.3 mm; 99.9% Zlatarna Celje, Celje, Slovenia	Substrate
Pt foil	Dimensions: 10 mm × 10 mm × 0.3 mm; 99.9% Zlatarna Celje, Celje, Slovenia	Substrate

Technical accessory	Specifications, producer	Role
Milling balls ϕ3 mm ZrO_2-Y_2O_3	Tosoh Corporation, Tokyo, Japan	Accessory for milling
Three roll mill	Three roll mill 50, Exakt Advanced Technologies GmbH, Norderstedt, Germany	Accessory for homogenization of the paste
Mounting epoxy	VersoCit-2 Kit, Struers, Ballerup, Denmark	Accessory for microstructure sample preparation
SiC papers	Struers, Ballerup, Denmark	Accessory for grinding
Diamond paste	DP-Paste P 3 μm, 0.25 μm, Struers Inc., Cleveland, USA	Media for polishing
OP-S suspension	Struers A/S, Ballerup, Denmark	Media for etching

3.2 Processing of $BiFeO_3$ Thick Films

The preparation of BFO thick-film structures is divided into two major steps: i) preparation of the powder mixture for the paste, and ii) screen-printing of the paste onto the substrates.

3.2.1 Solid-state synthesis of powder for screen printing

The starting powder mixture was prepared from Bi_2O_3 and Fe_2O_3. The raw oxide powders were first pre-milled individually in a planetary mill (Retsch, PM400, Haan, Germany) with 200 min^{-1} of rotational frequency for 4 h in absolute ethanol. Fe_2O_3 was milled in a 116 ml polyethylene vial with 207 g of ϕ3 mm YSZ milling balls. Bi_2O_3 was milled in a 54 ml polyethylene vial with 96 g of ϕ3 mm YSZ milling balls. After milling, both slurries were each dried in a separate glass dish overnight (for approximately 14 hours) at 120 ^oC and subsequently sieved through a 55-μm mesh.

As the next step, the pre-milled oxides were weighed in a stoichiometric $Bi/Fe = 1/1$ molar ratio and placed in a 54-ml polyethylene vial with 96 g of ϕ3 mm YSZ milling balls. The oxides were homogenized in a planetary mill with 200 min^{-1} of rotational frequency for 4 h in absolute ethanol. Then, the slurry was dried overnight at 120 ^oC and sieved through a 55-μm mesh.

3.2.2 Screen-printing and sintering of the thick-film structures

In order to prepare a paste for screen-printing, 67 wt% of Bi_2O_3–Fe_2O_3 powder mixture was mixed together with 33 wt% of organic vehicle using a three-roll mill. The organic vehicle consisted of 75 wt% of α-T, 15 wt% of BEA, and 10 wt% of EC.

The substrates used for screen-printing the BFO thick films can be divided into two groups: i) alumina with gold or platinum electrode, and ii) noble metal foils. Al_2O_3 substrates with a gold or platinum electrode (denoted as Au/Al_2O_3 and Pt/Al_2O_3, respectively) were prepared by screen-printing two layers of a commercially available Au paste and Pt paste on top of the alumina substrate. After each deposition, the Au/Al_2O_3 and Pt/Al_2O_3 structures were dried at 150 ^oC for 15 minutes. The as-printed Au/Al_2O_3 and Pt/Al_2O_3 substrates were sintered, respectively, at 900 ^oC for 10 minutes and 1200 ^oC for 1 h, both with 5 K/min heating and cooling rates. The thicknesses of the gold and platinum electrodes were ∼20 μm and ∼15 μm, respectively. In the case of the noble-metal foil substrates, commercially available, as-received, pure metallic Ag, Au, and Pt foils were used.

Next, one to five layers of paste, which consisted of a stoichiometric Bi_2O_3–Fe_2O_3 powder mixture and an organic vehicle, were deposited on the different substrates and after each deposition step, the film was dried at 150 ^oC for 15 minutes. The as-deposited and dried thick films were isostatically pressed at room temperature. The 2-hours annealing step at 500 ^oC was performed in order to burn out the organics from the films. These films were then reactively sintered (i.e., the reaction and the sintering were performed during the same annealing step) at different temperatures (730 ^oC, 740 ^oC, 750 ^oC, 770 ^oC, 800 ^oC or 820 ^oC), according to the temperature schedule illustrated in Fig. 3.1a. Selected films were additionally annealed after the sintering to either 810 ^oC for 2 minutes or 820 ^oC for 2 hours or 840 ^oC for 2 minutes or 850 ^oC for 10 minutes, as shown in Fig. 3.1b; this step is subsequently referred to as the “post-annealing”.

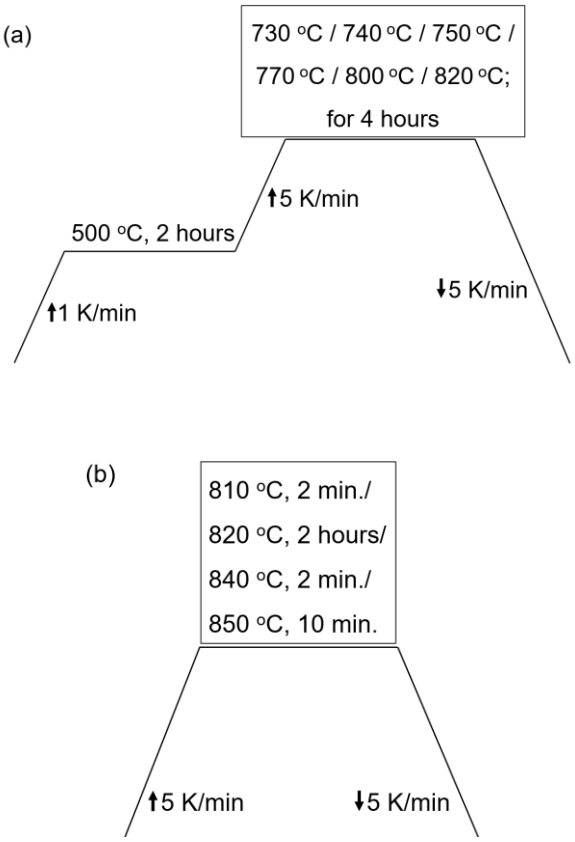


Figure 3.1: Schematic illustration of temperature profiles for the sintering step (a); and for the post-annealing step (b).

Notations of the screen-printed and sintered layered structures, which are used later in the thesis, are collected in table 3.2.

Table 3.2: Notations for the layered structures.

BFO on substrate	Notation
BFO on alumina with gold electrode	BFO/Au/Al_2O_3
BFO on alumina with platinum electrode	BFO/Pt/Al_2O_3
BFO on silver metal foil	BFO/Ag
BFO on gold metal foil	BFO/Au
BFO on platinum metal foil	BFO/Pt

BFO ceramics used as a reference for the X-ray diffraction analysis (see Chapters 3.3.3 and 4.4.1) and for the transmission electron microscopy (see Chapters 3.3.5.2 and 4.4.3) were prepared by sintering the Bi_2O_3–Fe_2O_3 powder mixture at 760 °C for 6 hours. BFO ceramics used for the electrical measurements (see Chapters 3.3.6 and 4.3.3.1) were prepared by sintering the Bi_2O_3–Fe_2O_3 powder mixture at 780 °C for 4 hours.

3.3 Characterization of the Powders and Films

3.3.1 Particle size distribution analysis

The milling of the starting powders and the Bi_2O_3–Fe_2O_3 mixture was monitored by measurements of the particle size distribution. This was measured in isopropanol with a static, light-scattering granulometer (Microtrac S3500, Particle Size Analyzer, Montgomeryville, Pennsylvania, USA). The particle size volume distributions were described with 90th (d_{90}), 50th (d_{50}), and 10th (d_{10}) percentiles of the particle size limit.

3.3.2 Heating-stage microscope

The shrinkage behaviour of the Bi_2O_3–Fe_2O_3 powder compact pressed with 100 MPa of uniaxial pressure was followed using a heating-stage microscope (Leitz V. 1a, Leitz, Wetzlar, Germany). The densification curve was recorded upon heating the powder compact up to 1020 ^{o}C, with a heating rate of 5 K/min. The shrinkage was determined from the sample dimensions, which were measured from the digital images of the compact at different temperatures.

3.3.3 X-ray diffraction

The phase compositions of the thick films were determined by XRD analysis at room temperature using an X'Pert PRO MPD diffractometer with Cu–$K_{\alpha 1}$ radiation (PANalytical B. V., Almelo, the Netherlands). The data were collected in the 2θ range from 10^{o} to 78^{o}, in steps of 0.017^{o}, with an integration time of 100 s. The LaB_6 SRM 660b standard (National Institute of Standards and Technology, Gaithersburg, Maryland, USA) was used for the calibration of the BFO peak positions. The intensities of the XRD patterns shown in the results chapter are presented using a linear scale.

The PANalytical X'Pert HighScore software package (PANalytical B. V., Almelo, The Netherlands) was used to analyse the XRD patterns. This software was also used to estimate the penetration depth of the X-rays in the samples during XRD analysis.

This software was also used to estimate the penetration depth of X-rays, τ, in the analysed samples at a given incident angle of X-ray, Θ:

$$\tau = 0.5 \times L \times \sin(\Theta) \tag{3.1}$$

L is the X-ray path length, which was calculated using the formula:

$$L = \frac{\ln(\frac{I_L}{I_o})}{-\mu/\rho_m \times \rho} \tag{3.2}$$

I_o is the initial intensity of X-ray; I_L is the intensity of X-ray transmitted from the material after passing through the path length, L, assuming $\frac{I_L}{I_o}$ ratio of 0.01, which means that 99% of initial intensity, I_o, is absorbed and 1% of initial intensity is reflected; μ/ρ_m is mass absorption coefficient of the material tabulated in the international tables; ρ is density of the material.

To obtain the fractions of phases in the samples, the XRD patterns were refined using the Rietveld method [105]. For this purpose, we used a Topas software package (Topas version 2.1, Bruker AXS, Karlsruhe, Germany). The scale factor and cell parameters were refined. The background was modelled using a Chebychev polynomial of tenth degree. The peak profiles were fitted using a Lorentzian function. The sample-displacement correction was also fitted.

Peakoc software [106] was used to obtain the normalized intensities of the observed XRD reflections of BFO thick films by fitting the peaks with a modified pseudo-Voigt function.

The amount of $[111]_{pc}$-oriented domains in the out-of-plane direction in the BFO/Pt/Al_2O_3 thick films was evaluated using the formula (3.3) [107]:

$$v_{111} = \frac{\frac{I_{111}}{I'_{111}}}{\frac{I_{111}}{I'_{111}} + 3\frac{I_{11\bar{1}}}{I'_{11\bar{1}}}} \tag{3.3}$$

v_{111} is the volume fraction of the material with $[111]_{pc}$ oriented domains in an out-of-plane thick-film direction; I_{111} and $I_{11\bar{1}}$ are the intensities of the $(111)_{pc}$ and $(11\bar{1})_{pc}$ peaks of the BFO thick film, respectively, and I'_{111} and $I'_{11\bar{1}}$ are the intensities of the $(111)_{pc}$ and $(11\bar{1})_{pc}$ peaks of a randomly oriented BFO ceramic, respectively. The intensity values (I'_{111} and $I'_{11\bar{1}}$) were measured on crushed BFO ceramics.

Next, the volume fraction of the material with $[111]_{pc}$-oriented domains, which has been reoriented from the random direction to the out-of-plane direction, η_{111}, is given by:

$$\eta_{111} = v_{111} - \frac{1}{4} \tag{3.4}$$

3.3.4 *In-situ* X-ray diffraction

The paraelectric-ferroelectric phase transition of the BFO films was followed by *in-situ* temperature-dependent XRD analyses using a PANalytical, X'Pert PRO (HTK) diffractometer with Cu–$K_{\alpha1}$ and Cu–$K_{\alpha2}$ radiation in combination with an Anton Paar HTK-1200N oven (Anton Paar, Graz, Austria). The Cu–$K_{\alpha2}$ radiation was stripped using the PANalytical X'Pert HighScore software. The temperature-dependent XRD analyses were performed in two heating and cooling runs in the temperature ranges 780–810 °C and 780–840 °C with a step of 10 °C and heating and cooling rates of 5 K/min (with few-minutes holding time at the individual temperatures required to collect the XRD patterns). The data were collected in the 2θ range from 37° to 41°, in steps of 0.026°, with an integration time of 100 s. All the XRD measurements were performed with the scattering vector perpendicular to the sample surface. The intensities of the *in-situ* XRD patterns shown in the results chapter are presented using a linear scale.

3.3.5 Analytical microscopy

3.3.5.1 Scanning electron microscopy

The density, thickness and microstructures of the thick film and the morphology of the Bi_2O_3–Fe_2O_3 powder mixture were investigated using a scanning electron microscope (SEM) JSM 7600F (Jeol, Tokyo, Japan) equipped with an Inca Energy Detector (energy-dispersive X-ray spectroscopy or EDXS). All the EDXS analyses were performed at 15 keV and a 15-mm working distance. The EBSD analyses were performed using an acceleration voltage of 20 kV, a working distance of 20 mm, a sample tilt angle of ~70° and a 50-µm aperture. The data were analysed using an Oxford Instruments HKL Technology CHANNEL 5 software package. The surface and cross-section electron back-scatter diffraction (EBSD) mappings were performed on areas of ~28,000 µm² or ~15,000 µm² with a 0.7-µm step size. To provide electrical conduction at the samples' surfaces and thus prevent charging during the SEM analyses, the samples were coated with carbon prior to the analyses using a sputter coater (SCD 050 Sputter Coater, Bal-Tec, Balzers, Liechtenstein).

For observations of the BFO thick-film cross-sections, the thick films were cut with a wire saw (Precision wire saw 3242, Well, Manheim, Germany), embedded in a mounting epoxy glue, ground with SiC papers with gradations of 800 and 1200 and polished with diamond pastes. After the polishing, the surfaces and cross-sections of the BFO thick films for the EBSD analysis and the AFM investigations were additionally polished for ~2 hours using an OP-S suspension.

The average grain size was determined from the SEM images of the sample surfaces. To extract the average grain size, areas of more than 250 grains were analysed and the digitalized microstructure images were processed with Image Tool software version 3.00

(University of Texas Health Science, San Antonio, Texas, USA). The grain size is expressed as the mean Feret's diameter (d). The porosity of the films was also evaluated from the SEM images, i.e., from ~2700-μm² areas of the sample surface.

3.3.5.2 Transmission electron microscopy

Transmission electron microscopy (TEM) imaging and selected-area electron diffraction (SAED) analysis were performed using a Jeol JEM-2010F microscope, operated at 200 kV and equipped with a JEOL EDXS detector and a CCD camera.

For investigations of the samples' cross-sections using TEM, a sample consisting of a ~6-μm-thick BFO film on Pt/Al_2O_3, was cut into pieces with dimensions ~2 mm × ~1 mm with a precision wire saw. The two pieces were glued together in such a way that the films were facing one towards the other and embedded in a brass ring with epoxy glue. The thickness of the whole structure was reduced to ~ 100 μm by grinding with SiC papers with gradations of 800, 1200, 2400 and 4000 and by subsequent polishing with diamond pastes. The ~100-μm-thick disk was dimpled on a dimple grinder (Model 623, Gatan, Pleasanton, California, USA) in such way that the thickness of the central part of the disc was reduced to 10–20 μm. Finally, the structure was ion milled with Ar using Gatan PIPS 691 (Gatan, Peasanton, California, USA) at an accelerating voltage of 3.5 kV.

Similarly, the reference BFO ceramic for the TEM/SAED analysis was prepared by cutting the ceramics into discs, grinding, polishing down to 100 μm, and then dimpling and finally thinning down to electron transparency. The error bars (see the results section 4.4.3) represent the maximum deviation from the average d-value determined by repeated measurements on the same SAED pattern.

3.3.5.3 Atomic force microscopy/Piezoresponse Force Microscopy

Topography and piezoresponse force microscopy (PFM) amplitude images were recorded with an atomic force microscope (AFM; Asylum Research, Molecular Force Probe 3D, Santa Barbara, California, USA) equipped with a piezoresponse force mode. A tetrahedral Si tip coated with Ti/Ir on a Si cantilever coated with Ti/Ir (Asyelec, AtomicForce F&E GmbH, Mannheim, Germany) was used for scanning the bare and polished thick-film surfaces. Dual AC Resonance Tracking Switching Spectroscopy (DART-SS) mode was used. Out-of-plane amplitude PFM images were measured in the DART mode at 20 V and 305 kHz. The local d_{33} (V) hysteresis response was measured in the SS mode (drive waveform parameters: amplitude 60 V, frequency 0.1 Hz, drive amplitude 10 V, off-loop).

3.3.6 Electrical and electro-mechanical properties

For the electrical and electro-mechanical measurements of the BFO thick film, an upper, sputtered Au electrode with a diameter of 1.5 mm was used. In the case of the BFO ceramics, the sample was electroded with sputtered Au on both sides of the pellet onto areas with diameters of 5 mm. The thickness of the BFO pellet was 0.36 mm.

Polarization–electric-field (P-E) hysteresis loops and current-density–electric-field (j–E) curves were measured using an aixACCT TF 2000 analyser (aixACT Systems GmbH, Aachen, Germany). For the P-E measurements, the sample was exposed to a single sinusoidal waveform of 10 V (2.9 kV/cm) and 1 Hz. For the j-E measurements, the sample was exposed to step-like voltages. The steps were 1 V in magnitude and were applied up to a maximum of +10 V (positive voltage polarity) and a minimum of –10 V (negative voltage polarity). Upon each of these steps, the voltage was maintained constant for 40 s and the electrical current was monitored. The current measurement time of 40 s was selected based on preliminary measurements. During these experiments the duration of the steps was varied between 2 s and 40 s and the longest time (40 s) at which the current values did not change significantly with respect to the preceding time tested (20 s) was selected.

The as-prepared BFO thick films on Pt/Al_2O_3 were characterized in terms of both direct and converse piezoelectric d_{33} responses. For the direct d_{33} measurements, the upper electrode of the thick-film samples was painted using a flash-dry silver paint (Spi Supplies Division of Structure Probe, Inc., West Chester, Pennsylvania, USA). In the second step, we re-measured the direct d_{33} response on samples with Au and Pt upper electrodes deposited by sputtering circled areas of 1 mm in diameter. For the converse d_{33} characterization as a

function of the driving-field frequency and amplitude, an upper, sputtered Pt electrode with a diameter of 1 mm was used.

The direct piezoelectric response of the as-sintered BFO thick films on Pt/Al_2O_3 was measured using a Berlincourt piezo d_{33} meter (Take Control PM10, Birmingham, UK) at a stress frequency of 200 Hz. The error bars (see results section 4.) represent the maximum deviation from the average d_{33} value determined by repeated measurements on the same sample.

The converse d_{33} response at weak (sub-coercive) fields was recorded on self-poled samples using a setup based on an optical-fibre sensor (MTI-2100 Fotonic Sensor, MTI Instruments Inc., Albany, New York, USA), a voltage generator (DS360, Stanford Research Systems Inc., Sunnyvale, California, USA), a voltage amplifier (Model 609E-6, Trek Inc., South Lockport, New York, USA), an oscilloscope (9310C, LeCroy Corporation, Chestnut Ridge, New York, USA), and a lock-in amplifier (Model SR830 DSP, Stanford Research Systems Inc., Sunnyvale, California, USA). A cantilever was used as the upper mechanical contact. The measurements were carried out at room temperature by using a continuous bipolar sinusoidal electric field of selected frequency and amplitude.

The displacement signals were recorded with an oscilloscope and a lock-in amplifier (the d_{33} and the piezoelectric phase angle were determined from the first-harmonic strain response).

For poling the BFO thick films on Pt/Al_2O_3 substrates a setup consisting of a high-voltage DC supply (Model 248, Keithley instruments Inc., Cleveland, Ohio, USA) connected to a poling stage was used.

Chapter 4

Results and Discussion

4.1 Characterization of the Bi_2O_3–Fe_2O_3 Powder Mixture

The efficiency of the milling process for the Bi_2O_3–Fe_2O_3 powder mixture used to formulate the paste for screen printing the BFO thick films was followed by a particle size distribution analysis. The results of the analysis are collected in Fig. 4.1a,b, where the particle size volume distributions of the mixture after 1, 2, 3 and 4 hours of milling (Fig. 4.1a) with the corresponding particle sizes d_{10}, d_{50} and d_{90}, (Fig. 4.1b) are shown. We can see in Fig. 4.1a,b that the 1-hour-milled powder has a broad particle size distribution with d_{10}, d_{50} and d_{90} of 0.2 µm, 0.5 µm and 2.4 µm, respectively. With each subsequent hour of milling the particle size decreases and this results in a particle size with d_{10}=0.1 µm, d_{50}=0.4 µm for and d_{90}=0.8 µm after 4 hours of milling. The milling procedure was stopped after 4 hours.

The morphology of the 4-hours-milled powder mixture was investigated by SEM and EDXS analyses. Backscattered electron (BE) SEM images of the powder taken at different magnifications are shown in Fig. 4.1c,d. The powder mixture is composed of larger particle agglomerates with a size of up to ~10 µm (Fig. 4.1c), which consist of sub-micrometre-sized Bi_2O_3 (white particles) and Fe_2O_3 (grey particles) (Fig. 4.1d).

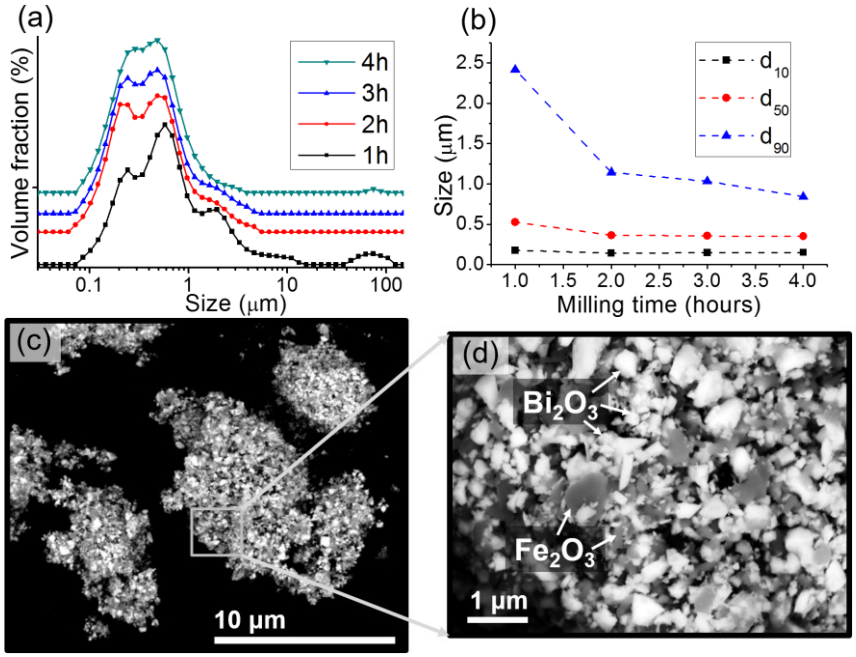


Figure 4.1: Characterization of the Bi_2O_3–Fe_2O_3 powder mixture. Granulomentric analysis of the mixture after 1, 2, 3 and 4 hours of milling (a) and calculated d_{10}, d_{50} and d_{90} particle sizes as a function of milling time (lines are drawn as a guide to the eye) (b). BE SEM images (c,d) of the 4-hours-milled Bi_2O_3–Fe_2O_3 powder mixture.

In the next step, we followed the densification behaviour of the 4-hours-milled powder mixture using a heating-stage microscope. The densification curve together with the optical images of the Bi_2O_3–Fe_2O_3 pellet at two different temperatures are shown in Fig. 4.2. The pellet starts to shrink at ~730 °C and achieves a maximum shrinkage of ~18% at ~830 °C. No major change in the shape of the pellet was observed up to 830°C, indicating that the pellet did not melt extensively.

Compared to the densification behaviour reported in Ref. [12], the densification of the powder, as shown in Fig. 4.2, starts at a ~50 °C lower temperature and achieves an 8% higher maximum shrinkage. These differences can originate from the particle size of the Bi_2O_3–Fe_2O_3 mixture; namely, we used a fine powder mixture with d_{50}=0.4 μm, while Rojac *et al.* [12] used a mixture with coarser particles, i.e., with d_{50}=1.1 μm.

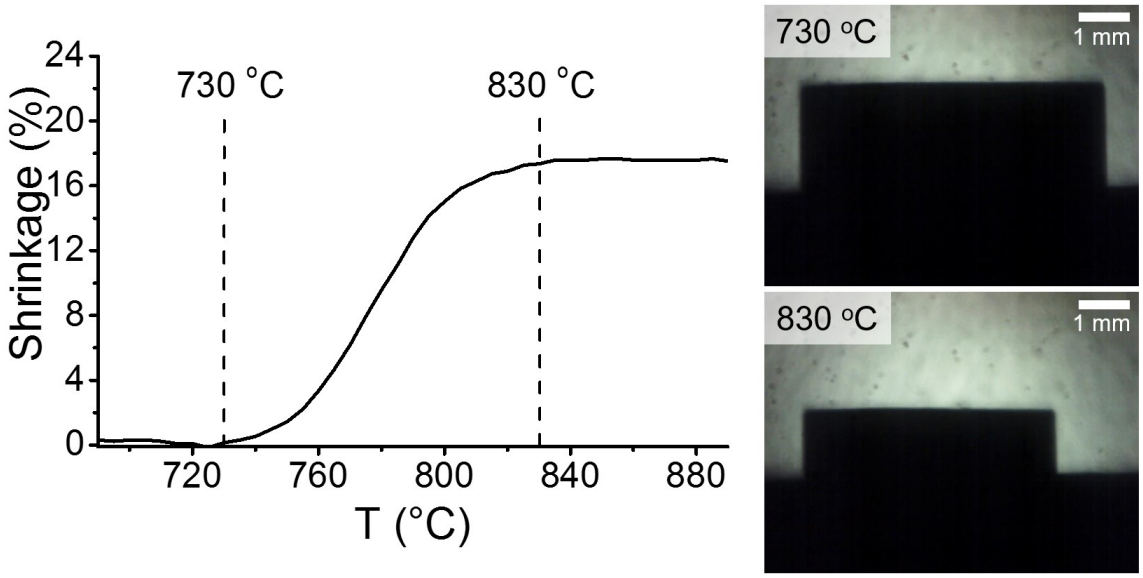


Figure 4.2: Densification curve of the 4-hours-milled Bi_2O_3–Fe_2O_3 powder mixture with images of the Bi_2O_3–Fe_2O_3 pellet at 730 °C and 830 °C.

Although thick films are subjected to constrained sintering and thus densify under different conditions than bulk ceramics [59, 60], we used the data on the densification behaviour of the Bi_2O_3–Fe_2O_3 pellet (Fig. 4.2) as a guide to design the sintering process for the thick films. Therefore, based on the shrinkage behaviour of the 4-hours-milled Bi_2O_3–Fe_2O_3 powder mixture, for further sintering experiments on the thick films we selected temperatures between 730 °C and 820 °C.

4.2 $BiFeO_3$ Thick Films on the Au/Al_2O_3 Substrate

The influence of the sintering temperature on the composition and phase distribution in the BFO films was studied. For this purpose, the as-deposited films on the Au-electroded Al_2O_3 substrate were sintered at different temperatures, i.e., at 730 °C, 750 °C, 770 °C, 800 °C, 820 °C, for 4 hours. The results of XRD, SEM and EDXS analyses are shown in the following section.

4.2.1 The influence of the sintering temperature on the phase composition and microstructure

Fig. 4.3 shows the XRD patterns of the as-sintered thick-film structures. In all the films, the perovskite BFO phase was identified together with varying amounts of the secondary phases: $Bi_{25}FeO_{39}$ (sillenite) and $Bi_2Fe_4O_9$ (mullite) (see Fig. 4.3b). In addition, reflections related to the Au electrode were also observed. As seen from the peak intensities, the fractions of the three phases vary significantly depending on the sintering temperature (Fig. 4.3b).

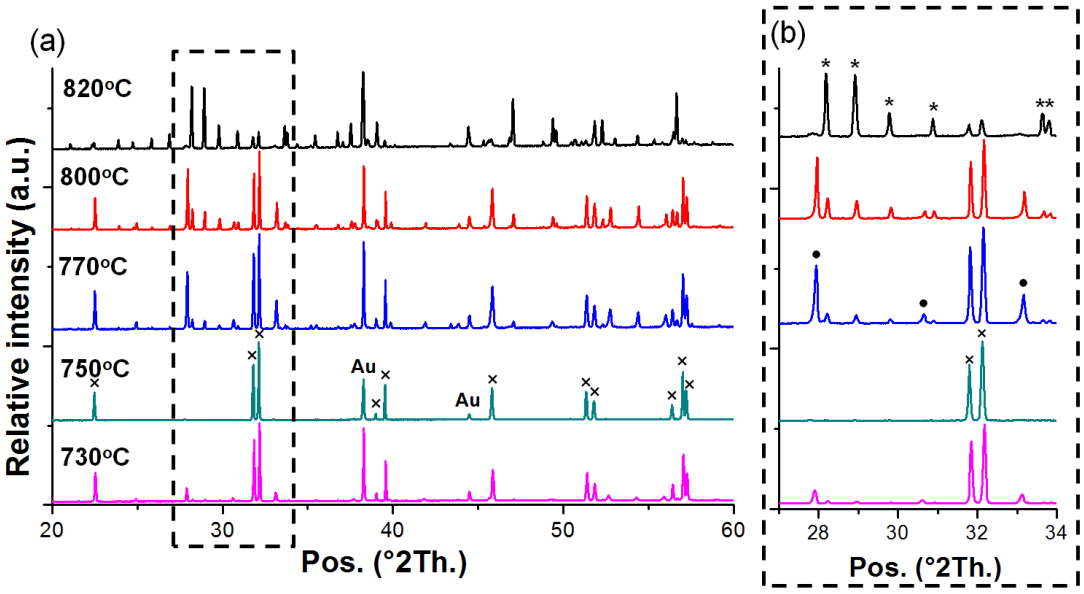


Figure 4.3: XRD patterns of $BFO/Au/Al_2O_3$ structures sintered at different temperatures (a) and enlarged region of the XRD patterns illustrating the major peaks of secondary mullite and sillenite phases (b). × $BiFeO_3$ (PDF No: 01-071-2494), * $Bi_2Fe_4O_9$ (PDF No: 01-074-1098); • $Bi_{25}FeO_{39}$ (PDF No: 01-078-1543); peaks denoted with Au correspond to the gold electrode.

In order to quantitatively evaluate the fractions of the phases present in the thick films, the Rietveld refinement method was used. The resulting wt.% fractions are plotted as a function of the sintering temperature in Fig. 4.4. The highest degree of phase purity, i.e., the largest wt% of the perovskite phase and the smallest wt% of mullite and sillenite phases, was achieved when the thick film was sintered at 750 °C. At this temperature, a nearly-single-phase BFO was produced with ~1 wt% fraction of the sillenite phase. With respect to 750 °C, either lower or higher sintering temperatures resulted in an increase in the amount of secondary phases present in the films.

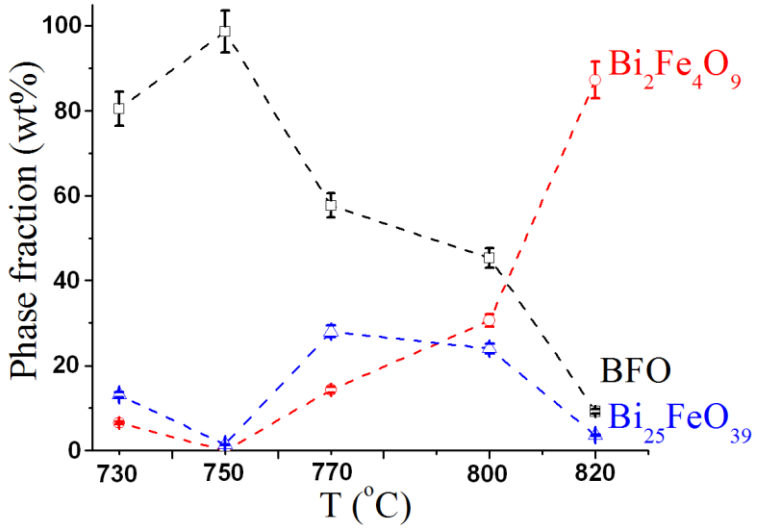


Figure 4.4: Quantitative phase composition of BFO thick films as a function of sintering temperature. Error bars express the typical ± 5% uncertainty [108] of the XRD technique. The dashed lines are drawn as a guide to the eye.

The fractions of secondary sillenite and the mullite phases vary non-monotonically as a function of the sintering temperature (see, for example, the fraction of the sillenite phase as a function of the sintering temperature in Fig. 4.4). If the secondary phases appear as a result of the diffusion reactions between Bi_2O_3 and Fe_2O_3 [40], it is expected that, in the presence of a sufficiently high chemical gradient and short diffusion paths, their fraction would lower with increasing sintering temperature at the expense of the formation of the perovskite BFO (as it is actually observed in the temperature range 730–750 °C). We note, however, that above 750 °C the amount of the mullite phase progressively increases with the temperature up to 820 °C, at which point it becomes the major phase in the film. On the other hand, the concentration of the sillenite phase exhibits a maximum at 770 °C, after which it decreases with increasing sintering temperature.

When interpreting the XRD results we should consider limitations of the XRD method for the investigation of the phase composition of BFO thick films, such as the penetration depth of the X-rays into the BFO material. The penetration depth is a function of the incident angle and in the case of BFO it varies from ~1 μm at $2\theta=10^o$ to ~6 μm at $2\theta=60^o$ (see the experimental part of Chapter 3.3.3). Thus, if the analysed BFO films are thicker than ~6 μm, only the surface of the films will be probed by X-rays and the part of the thick film closer to the film/Au interface will not be involved in the diffraction process and will thus not contribute to the XRD pattern. We must note here that the reflections of the gold electrode related to the Au/Al_2O_3 substrate observed in the film (Fig. 4.3, Au peaks) are associated with the substrate material from around the BFO film, which was also exposed to the X-rays during the analysis.

In order to analyse more precisely the phase composition, for the BFO thick films, particularly at the film/Au interface, SEM analysis was performed. EDXS analysis was used to identify the perovskite, mullite and sillenite phases; typical EDXS spectra for these phases obtained from the BFO thick films are represented in Fig. 4.5.

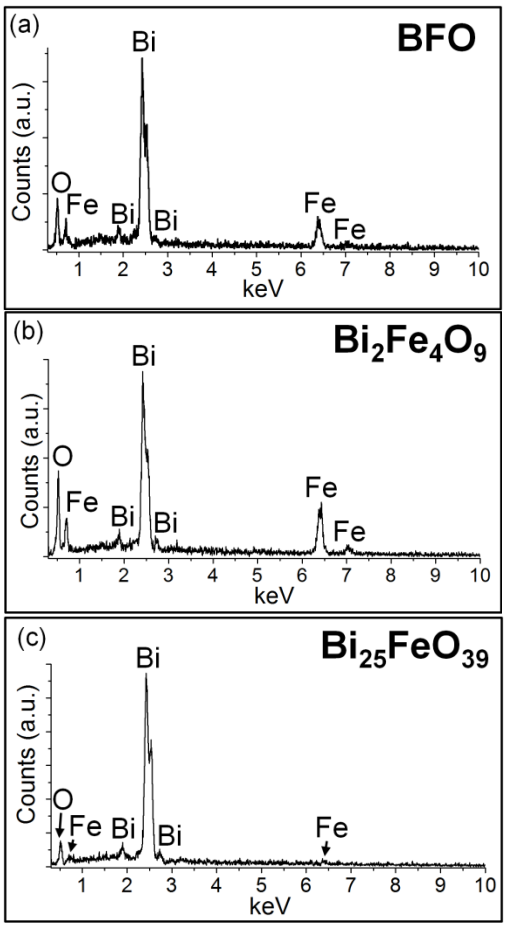


Figure 4.5: EDXS spectra of the perovskite BFO, mullite $Bi_2Fe_4O_9$ and sillenite $Bi_{25}FeO_{39}$ phases acquired at 15 keV.

BE SEM images of microstructures with both cross-sectional and surface views of the thick BFO films sintered at different temperatures (from 730 °C to 820 °C) are collected in Figure 4.6. The thick film sintered at 820 °C exhibits large, up to 10-µm-sized, cuboidal grains of the mullite phase surrounded by the sillenite phase (Fig. 4.6a,f). No BFO was observed in this image. The amount of the sillenite phase visible at the surface (Fig. 4.6f) appears significantly lower as compared to that seen in the cross-sectional image of the same film (Fig. 4.6a). The films sintered below 820 °C, i.e., from 800 °C down to 730 °C (Fig. 4.6b-e and 4.6g-j), exhibit all three phases, i.e., BFO perovskite, mullite and sillenite phase. In all films Fe_2O_3 was also present in minor concentration (see inset in Fig. 4.6d). On average, the size of the mullite grains decreases with decreasing temperature from ~10 µm at 800 °C (Fig. 4.6b,g) to a few µm at 730 °C (Fig. 4.6e,j). It was also observed that in all the films the mullite phase is concentrated at the interface with the Au electrode (Fig. 4.6b-e).

In contrast to the mullite phase, which is concentrated at the film/electrode interface, the distribution of the sillenite phase changes depending on the sintering temperature; small, µm-sized sillenite inclusions observed in the microstructures sintered at 730 °C (Fig. 4.6e) and 750 °C (Fig. 4.6d) start to segregate at 770 °C (Fig. 4.6c), forming larger, up to 10-µm-sized inclusions at 800 °C (Fig. 4.6b,g), which finally wet the mullite grains at 820 °C (Fig. 4.6a,f). Surface images of the thick film sintered at 800 °C (Fig. 4.6g) show well-crystallized cubic grains of the sillenite phase, which, however, change shape at 820°C, resembling a solidified liquid. This suggests a progressive melting of the sillenite phase as the temperature is increased.

The BFO grains, which were observed on the surface of the thick films sintered at 730–800 °C, increase in size from 1.0 $\pm$ 0.5 µm (730°C) to 4.4 $\pm$ 1.8 µm (800°C) with increasing

sintering temperature. Thick films sintered at the lowest temperature of 730 °C exhibited the highest, ~9 area%, porosity.

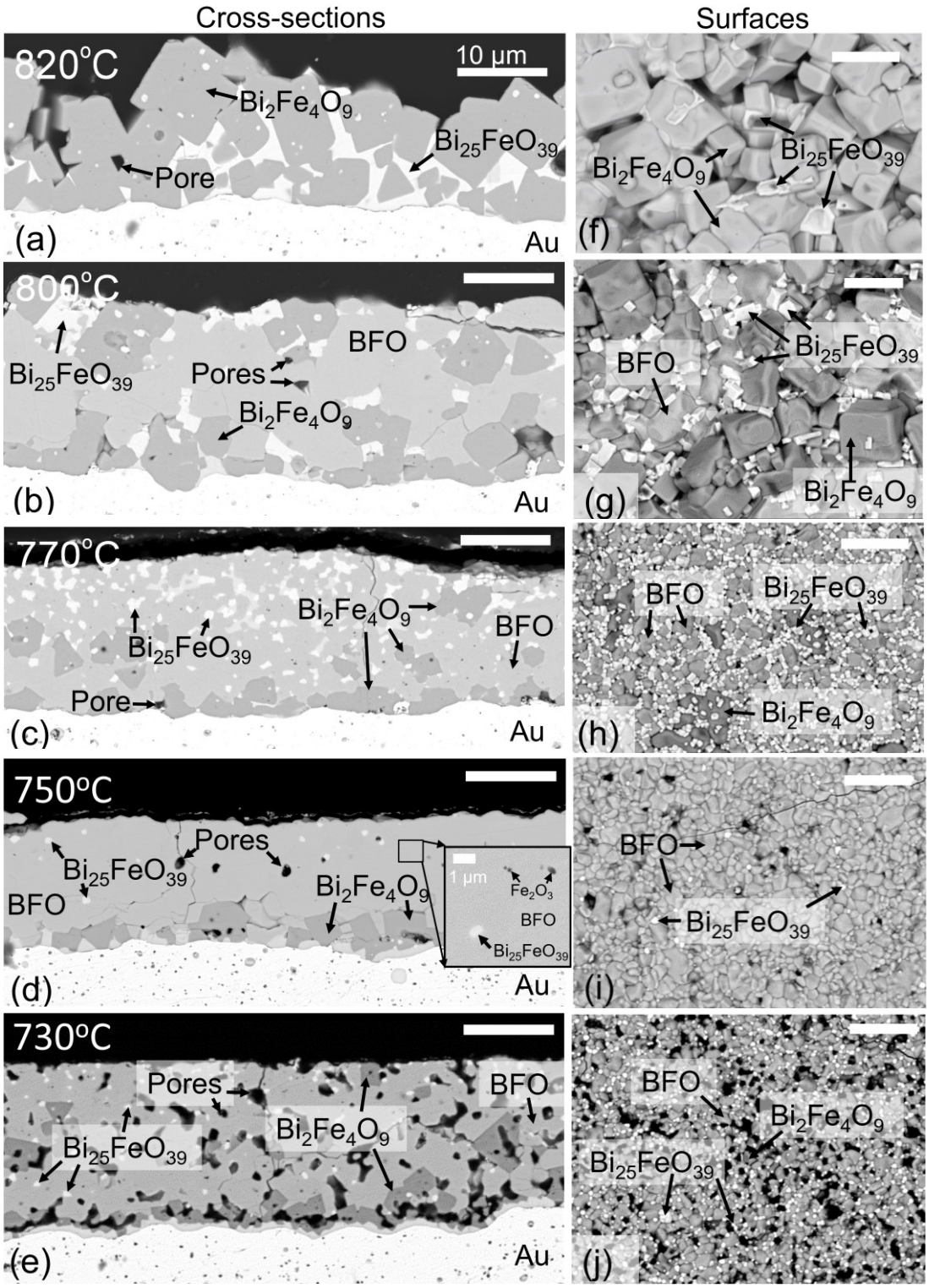


Figure 4.6: BE SEM images of the cross-sections (a-e) and surface views (f-j) of BFO thick films sintered at different temperatures between 730 °C and 820 °C.

By using both XRD and SEM analyses a complete picture of the temperature dependences of the phase composition and the phase distribution was established. As

shown in Figures 4.4 and 4.6, high-density thick films with the highest phase purity were achieved at the sintering temperature of 750 °C. At temperatures both lower and higher than 750 °C, increased amounts of the secondary phases were formed. In order to explain this phenomenon, both thermodynamic and kinetic aspects of the system and/or the presence of impurities were considered, as described in the following.

As explained in Chapter 1.2.2.1, Mikhailov *et al.* [42] calculated the change of the molar Gibbs free energy ($\Delta G°(T)$) for the formation reaction of BFO from the constituent oxides Bi_2O_3 and Fe_2O_3. The calculated $\Delta G°(T)$ for 777°C and 827°C were –12.7 kJ/mol and –9.4 kJ/mol, respectively. The authors also reported that the driving force for this reaction further reduces with the increase of temperature above 827 °C, and thus proposed ~720 °C as an optimal temperature for the synthesis of BFO. On the other hand, Selbach *et al.* [38] published thermodynamic data on the $\Delta G°(T)$ of the reaction involving the BFO decomposition to the sillenite and mullite phases (reaction 1.2), which is slightly positive ($-0.1\ kJ/mol < \Delta G°(T) < 0$) in the temperature range 447–767 °C. Therefore, if we consider the temperature range of our experiments, i.e., 730–820 °C, the formation of BFO from the constituent oxides should be favoured across the whole temperature range. In addition, the formed BFO should be stable against the secondary phases at the sintering temperatures of 770 °C, 800 °C and 820 °C, whereas it should exhibit only slight instability at temperatures of 730°C and 750°C, resulting in a slow decomposition to the two secondary phases (according to the reaction 1.2).

In addition to thermodynamics, we should also consider reaction kinetics. It is known that solid-state reactions require elevated temperatures to provide sufficient diffusion of the ions. For our case, 730 °C appears to be too low for the reaction to proceed kinetically to completion; this is seen in the high porosity and large amount of secondary phases in the film processed at this temperature (Fig. 4.6e,j). However, the reaction further proceeded towards the formation of BFO at 750°C, and this is likely the result of enhanced diffusion due to the higher temperature.

The formation of secondary phases in the thick films sintered between 770° and 820 °C (Fig. 4.4, Fig. 4.6a-d and Fig. 4.6f-i), as well as the formation of the mullite phase close to the BFO/Au interface (Fig. 4.6b-e), cannot be explained by the mentioned thermodynamic or kinetic considerations. We also note that 820 °C is well below the peritectic decomposition temperature (~933 °C) of the BFO [13]. The observed increased fraction of secondary phases with increasing temperature between 750 °C and 820 °C (Fig. 4.4) therefore suggest the involvement of other phenomena, such as i) bismuth loss due to evaporation, ii) interface reactions between the electrode, substrate and the thick film and/or iii) the presence of impurity elements.

A likely origin of the formation of secondary phases is the sublimation/evaporation of the volatile bismuth oxide at high temperatures [3, 39, 41, 42], which is expected to be more pronounced in thick films, relative to ceramics, due to the higher surface-to-volume ratio of the films. According to the kinetics of the reaction between Bi_2O_3 and Fe_2O_3 (Chapter 1.2.2.2), the sillenite phase forms as a first reaction product [40]. This sillenite phase then melts incongruently at 790 °C [109, 110], meaning that an increased evaporation of bismuth may occur from this melt at sintering temperatures exceeding 790 °C [3, 39, 41, 42]. As we discussed earlier, at a high sintering temperature of 820 °C the amount of sillenite phase is lower at the film surface compared to that in the interior of the film (Fig. 4.6a,f). This indicates that a pronounced evaporation from the liquid Bi-rich phase took place at 820 °C, which is in agreement with the studies on BFO ceramics [41]. Additionally, the XRD analysis, which pertains to the surface layer of the film, indicates that the mullite phase is more prevalent than the sillenite phase. In agreement with the evaporation of bismuth at high temperatures (Chapter 1.2.2.2), the mullite phase is the majority phase at the surface of the film sintered at 820 °C (Fig. 4.3-4.4).

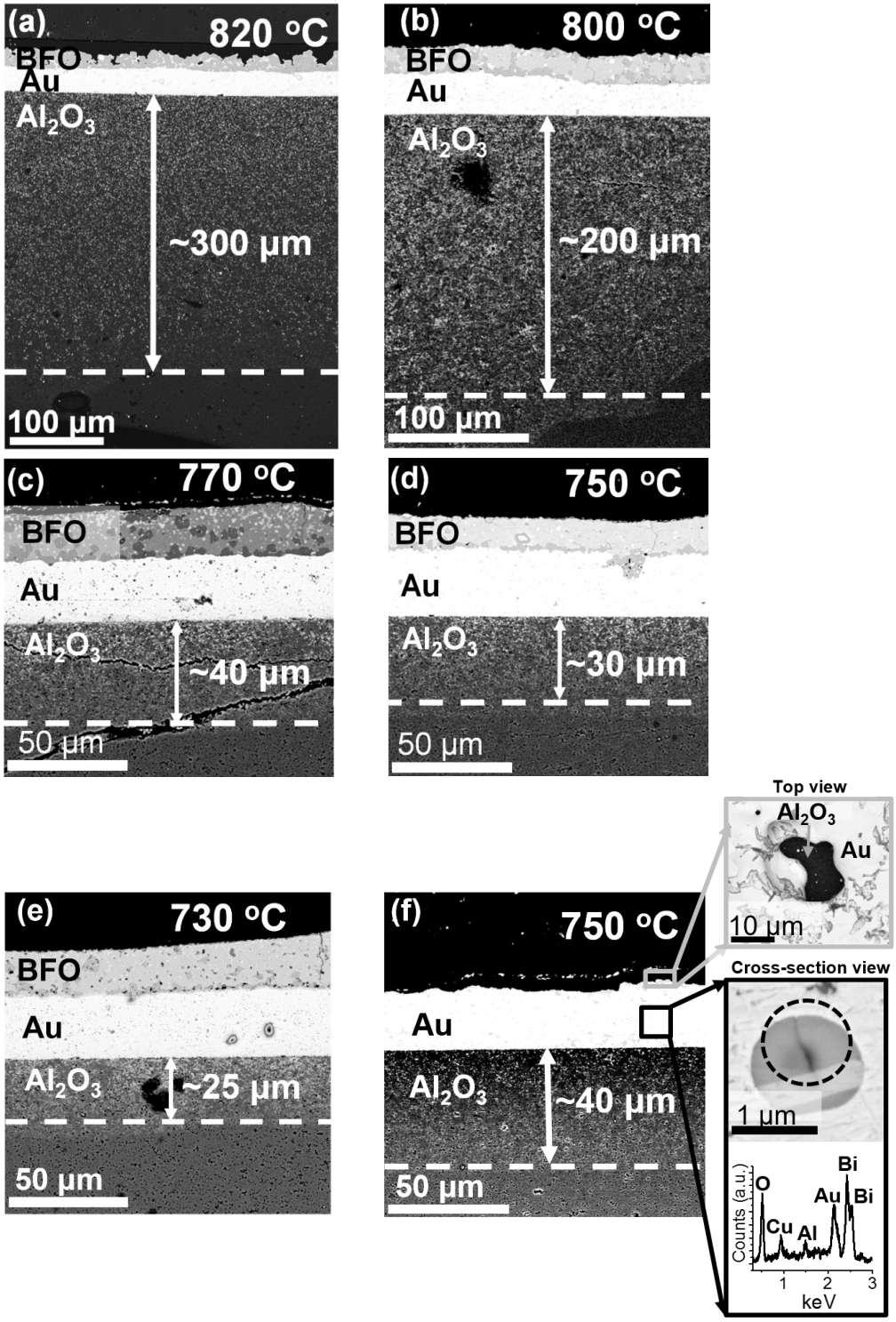


Figure 4.7: BE SEM cross-section images of the BFO/Au/Al_2O_3 structure (a-e) sintered at different temperatures. Note the change of magnification in the images. The cross section of the Au/Al_2O_3 substrate without the BFO thick film annealed at 750 °C (f), is added for comparison. The upper inset in (f) shows a part of the Au surface where a large pore was observed percolating the thickness of the electrode. The bottom inset shows a cross-section view of the Au electrode where impurities (Cu, Bi) were identified (see corresponding EDXS spectrum acquired from the circled area) The penetration depth of the Bi-rich phase into the substrate is marked by double arrows.

In addition to the evaporation, the reaction between the film and the substrate or electrode is likely to influence the phase composition of the film. In order to evaluate the likelihood and extent of the reaction between the BFO film and the Au/Al_2O_3 substrate in the samples, additional SEM and EDXS analyses of the substrate were performed; the results are shown in Fig. 4.7. The analysis reveals small, μm-sized inclusions (seen as white spots in Fig. 4.8a) in the substrate with increasing penetration depth as the sintering temperature was increased. According to the EDXS analysis (Fig. 4.8b) this phase is Bi-rich and appears as filling the regions between the grains in the polycrystalline alumina substrate (Fig. 4.8a).

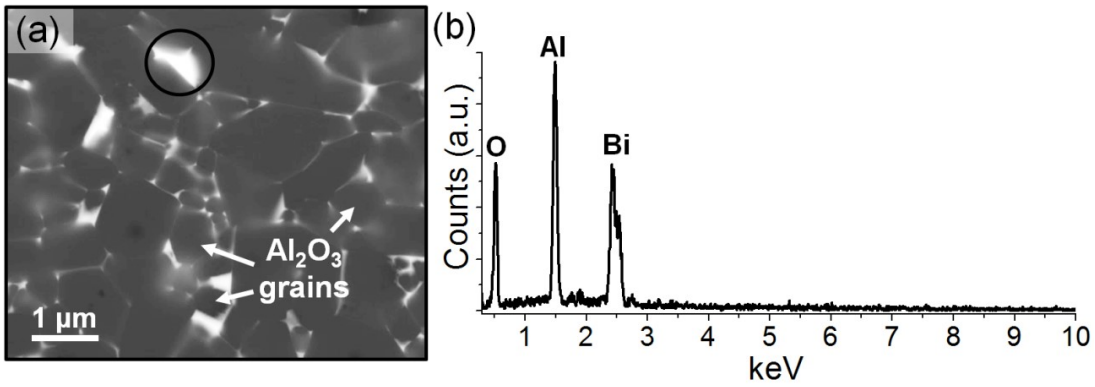


Figure 4.8: The BE SEM image of the Al_2O_3 substrate (sample sintered at 820 °C) (a) and EDXS spectrum taken from the marked region (circle) (b). Aluminium peak which was also detected in the EDXS spectrum originates from the Al_2O_3 matrix.

As indicated in Fig. 4.7, we evaluated the diffusion of the Bi-rich phase into the alumina substrate from BE SEM images and compared the penetration depth of the Bi-rich phase as a function of sintering temperature. The results of this analysis are shown in the Fig. 4.9.

As the sintering temperature increases from 730 °C to 770 °C, the depth of penetration of the Bi-rich phase into the substrate increases from 25 μm to 40 μm. Between sintering temperatures of 770 °C and 800 °C, however, there is a significant increase in the Bi-rich phase penetration depth, from 40 μm to 250 μm, and at the maximum sintering temperature of 820 °C the penetration depth (370 μm) is approximately seven times greater than that at 770 °C (40 μm). This abrupt increase in the penetration depth of the Bi-rich phase occurs over the same temperature range at which incongruent (peritectic) melting of the sillenite phase is expected [109, 110] (see dashed line in Fig. 4.9), indicating that it is related to the liquid phase formation and thus to the penetration of the Bi-rich liquid into the substrate. This assumption is supported by the observation that below 790 °C, where the sillenite phase should be present in a solid form, the penetration depth of the Bi-containing phase does not change significantly with temperature (Fig. 4.9). Similarly, studies by Immovilli *et al.* [111] on the reaction between a screen-printed Bi_2O_3 thick film and an Al_2O_3 substrate showed that significant diffusion of Bi_2O_3 into Al_2O_3 occurs at a temperature (850 °C) exceeding the melting temperature of Bi_2O_3 (~830 °C [112]). This indicates a propensity for Bi_2O_3 diffusion into the substrate once a liquid phase is formed.

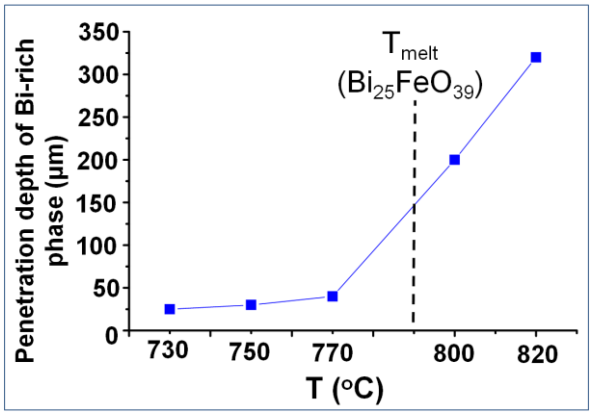


Figure 4.9: Penetration depth of Bi-rich phase from BFO thick films into Au/Al_2O_3 substrate as a function of sintering temperature determined from BE-SEM cross-sections of $BFO/Au/Al_2O_3$ structures (see arrows in Fig. 4.7). The dashed vertical line indicates the melting point (peritectic decomposition) of the $Bi_{25}FeO_{39}$ phase (~ 790 °C). The solid line is drawn as a guide to the eye.

To verify whether the diffusing Bi-rich phase originates from sources other than the BFO film, we also analysed the Al_2O_3 substrate with the printed Au electrode but without the printed BFO film on the top of the Au layer (Fig. 4.7f). EDXS analysis of the Au electrode revealed the presence of bismuth in the electrode layer (Fig. 4.7f, bottom inset). In addition, large pores of several tens of micrometers in size were observed in the Au electrode layer (Fig. 4.7f upper inset); it should be noted that bottom Al_2O_3 substrate is clearly visible through the pore, meaning that the pore creates a channel for the diffusion of Bi-rich liquid phase from the BFO film into the alumina substrate.

As shown in Fig. 4.7f, this Bi-rich phase diffused inside the Al_2O_3 substrate during sintering in much the same way as it was observed for the $BFO/Au/Al_2O_3$ structures. Furthermore, a similar diffusion depth of the Bi-rich phase was observed in the Au/Al_2O_3 (Fig. 4.7f) and $BFO/Au/Al_2O_3$ structures (Fig. 4.7d) sintered at 750 °C. This suggests that the main source of the diffusing bismuth at this low temperature is the Au electrode, not the BFO film, implying that probably little bismuth was lost from the BFO film through diffusion into the substrate. Therefore, sintering temperatures below 790 °C effectively minimized the diffusion of the Bi-rich phase from the BFO layer into the Al_2O_3 substrate, preventing the BFO film from becoming highly non-stoichiometric.

As observed in Figure 4.6b-e, in the films sintered between 730 °C and 800 °C the mullite phase segregated preferentially at the BFO/Au interface. This phenomenon was further investigated. Figure 4.10 shows a BE-SEM image of the BFO/Au interface for the film sintered at 730 °C with an accompanying EDXS spectrum. In the BE SEM image (Fig. 4.10a), besides the perovskite, sillenite and mullite phases, an additional layer was observed between the electrode and the mullite phase. According to the EDXS analysis, this layer contains copper and bismuth (Fig. 4.10b). A layer with a similar chemical composition was also found in the films sintered at 750 °C (Fig. 4.6d, light-grey phase at the BFO/Au interface), while at higher sintering temperatures grains of Cu-containing phase were detected within the films and not at the BFO/Au interface layer.

Copper was found to be the major impurity in the Au electrode, which is most likely the reason for the formation of the mullite phase at the BFO/Au interface. Presumably, copper oxide reacted with the bismuth oxide from the film, resulting in Bi_2CuO_4, a phase reported in the Bi_2O_3–CuO phase diagram [113]. Besides, the Bi_2O_3–CuO phase diagram reports on several different CuO-Bi_2O_3 eutectic compositions, i.e., at ~ 12 mol% of CuO (eutectic temperature T_{eut}~770 °C) [113], ~ 6 mol% CuO (T_{eut}~ 740 °C) [114] and ~ 5 mol% CuO (T_{eut}~600 °C) [115]. The reaction of copper oxide with bismuth oxide is thus expected to cause a local bismuth deficiency in the film, resulting in the formation of the mullite phase at the film/electrode interface. Similar reactions were observed between $BiFeO_3$ and SiO_2 [2, 39].

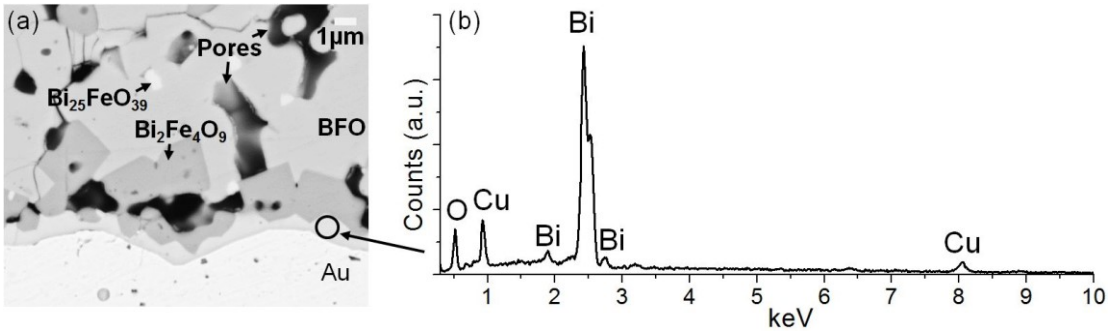


Figure 4.10: BE SEM image of the interface between the BFO and Au/Al_2O_3 substrate sintered at 730 °C (a) and EDXS spectrum taken from the circled area as indicated with an arrow (b).

In Fig. 4.11 all the above-described processes that can take place during reactive sintering of BFO thick films, i.e., evaporation of Bi(g)/Bi oxides (g), diffusion of the Bi-rich liquid phase into the alumina substrate through the channels in the electrode, segregation of the mullite phase on the BFO/Au interface and chemical reaction of BFO with the impurities from the electrode, are shown schematically.

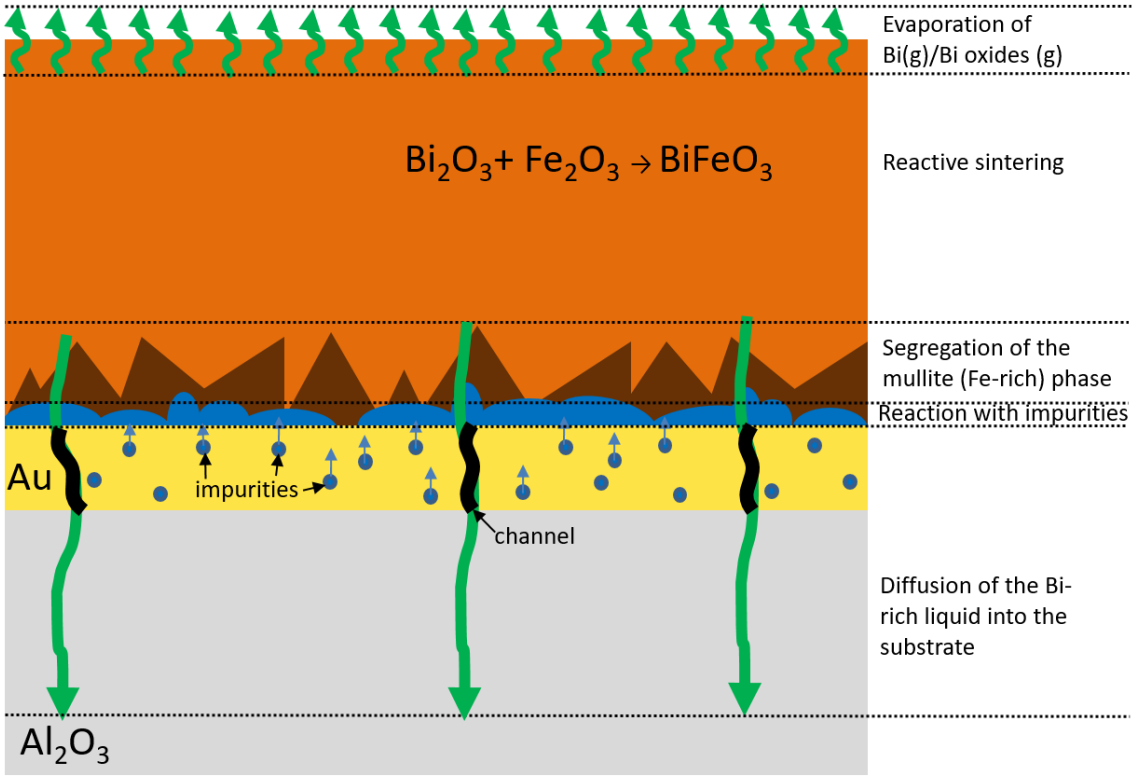


Figure 4.11: Schematic illustration of all possible processes taking place during the sintering of BFO thick films.

To conclude, we managed to drastically reduce the amount of secondary phases by optimizing the sintering temperature. As the copper impurity was introduced into the film through the electrode, we can conclude that in order to avoid the degradation of the phase composition of BFO thick films, particularly at the film/electrode interface, higher purity electrode and substrate materials are required. This is presented in the following section.

4.3 $BiFeO_3$ Thick Films on the Noble Metal Foils

In order to prepare phase-pure BFO thick films and to investigate the influence of the different substrates on the BFO thick-film composition and microstructure, we tested several high purity metals as substrates, i.e., Ag, Au and Pt. Based on the experiments shown in Chapter 4.2 (see Fig. 4.6 and Fig. 4.7) we chose a sintering temperature of 750°C. The results of the XRD, SEM and EDXS analyses are shown in the following section.

4.3.1 The influence of the substrate material on the phase composition and the microstructure

XRD patterns of the BFO thick-film structures, denoted as BFO/Ag, BFO/Au and BFO/Pt, are shown in Fig. 4.12. In all three films, the perovskite BFO was identified as the majority phase together with weak reflections of $Bi_{25}FeO_{39}$ (sillenite) secondary phase. The amount of sillenite phase in the BFO thick films was evaluated by the quantitative Rietveld refinement method [105] as ~2.5 wt%, ~0.3 wt% and ~1.6 wt% for samples deposited on Ag, Au and Pt substrates, respectively.

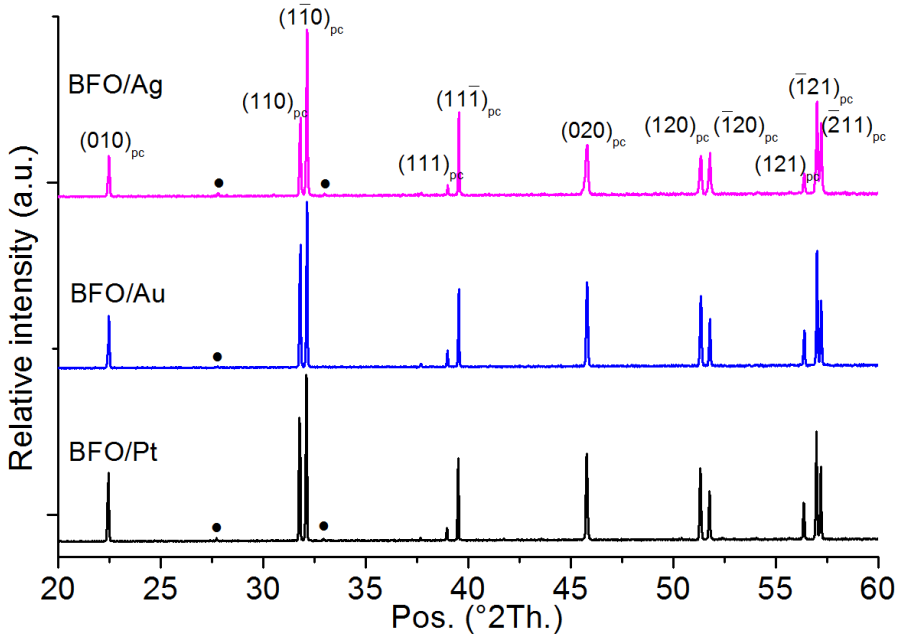


Figure 4.12: XRD patterns of BFO/Ag, BFO/Au and BFO/Pt thick films sintered at 750 °C. The reflections of BFO are marked with (hkl) indices in pseudocubic notation (PDF No: 01-071-2494); •$Bi_{25}FeO_{39}$ (PDF No: 01-078-1543).

In order to analyse the distribution of phases throughout the films in more detail, we performed SEM analysis. Fig. 4.13 shows the BE SEM images of the surfaces and polished cross-sections of BFO/Ag, BFO/Au and BFO/Pt structures sintered at 750 °C. Inspection of the images clearly shows that the microstructure and phase composition of the BFO thick films depends on the type of the metal foil used as the substrate. The BFO/Ag thick film (Fig. 4.13a,d) contains the perovskite as the main phase with some inclusions of the sillenite phase and mullite phases of up to ~5 μm in size (Fig. 4.13a). This film is characterized by a high density with small pores (~2 μm). In contrast, the BFO/Au (Fig. 4.13b,e) and BFO/Pt films (Fig. 4.13c,f) are almost single-phase perovskite, containing only a small amount of the sillenite phase in the form of small inclusions (~1 μm in size), clearly visible in the cross-section images (Fig. 4.13b,c). The average BFO grain size determined from the SEM images of the films surfaces (Fig. 4.13d-f) was similar for all the samples, i.e., 2.2 ± 1.3 μm, 1.9 ± 0.9 μm and 1.7 ± 0.9 μm for BFO/Ag, BFO/Au and BFO/Pt, respectively.

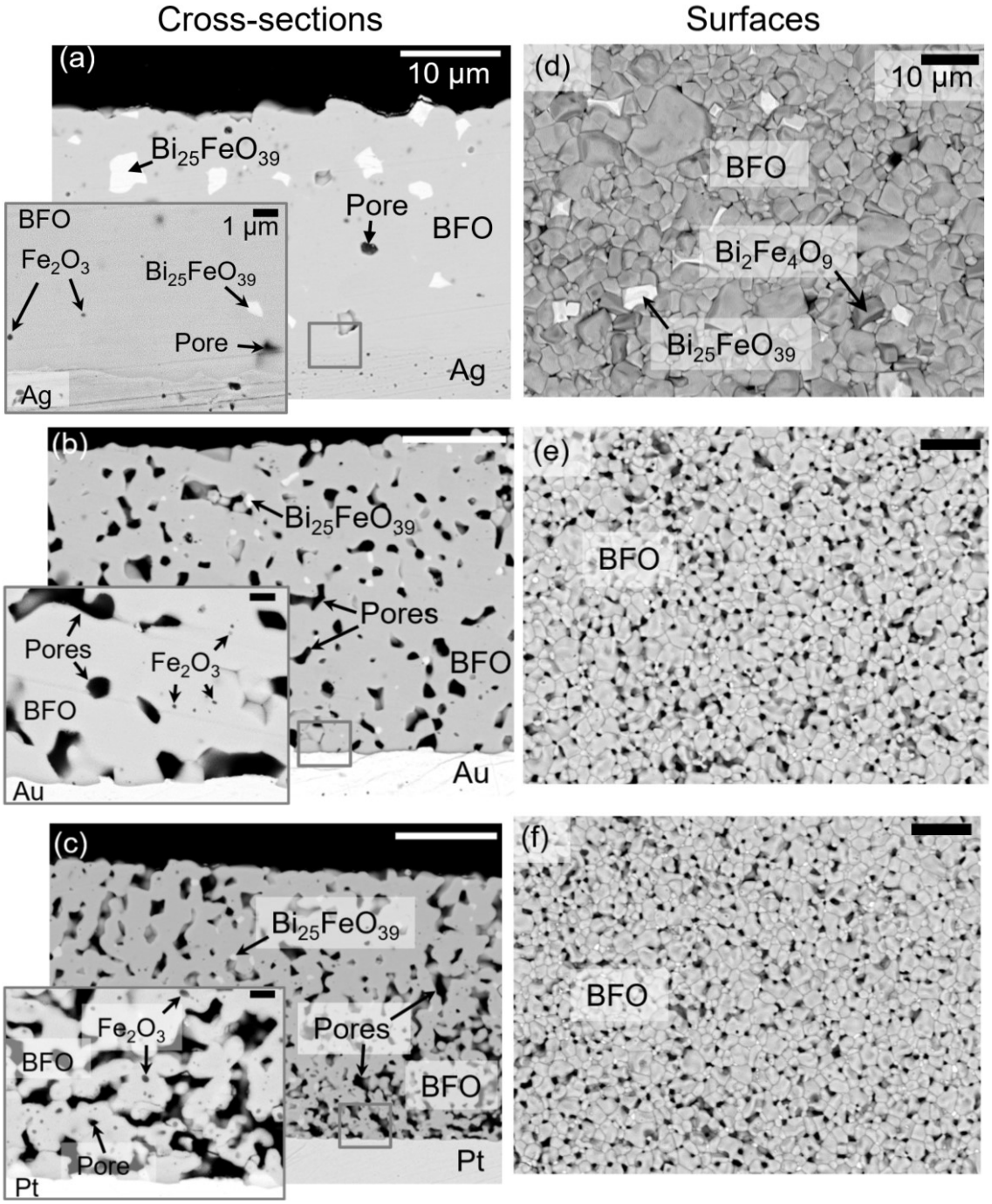


Figure 4.13: BE SEM images of polished cross-sections (a-c) and surfaces (d-f) of BFO/Ag (a,d), BFO/Au (b,e) and BFO/Pt (c,f) thick films sintered at 750 °C.

The densities of the BFO/Au and BFO/Pt films (Fig. 4.13b,c) are significantly lower than the BFO/Ag film (Fig. 4.13a). It is also worth noting that the BFO thick film on Pt (Fig. 4.13c) is characterized by a gradient in porosity along the films thickness with a higher porosity in the vicinity of the substrate/film interface than at the film surface.

In all the three films, unreacted oxide (Fe_2O_3) was observed as dark, round inclusions. Interestingly, the concentration of Fe_2O_3 appears to be dependent on the type of substrate, with the lowest concentration observed in the BFO/Ag film (Fig. 4.13a, inset) and the highest in the BFO/Pt film (Fig. 4.13c, inset).

While no secondary phases could be detected at the interface between the BFO and Ag, Au or Pt, we further investigated any possible interdiffusion between the layers using SEM/EDXS analyses. Fig. 4.14 shows the surface of the BFO/Ag film in which small, ~0.5-µm-sized, Ag-containing inclusions were identified, revealing that Ag diffuses into the film at 750 °C and forms regions with a higher Ag concentration (see also the inset of Fig. 4.14a). The Ag–Bi_2O_3 phase diagram [116] shows the existence of a eutectic composition at ~12 mol% of Ag with T_{eut}~ 711 °C. Considering that the films were sintered at 750°C, it is possible that during sintering the observed Ag-containing phase was present as a liquid and thus promoted the densification of the BFO film. This might explain the higher density of the BFO/Ag film relative to that of BFO/Au and BFO/Pt (Fig. 4.13).

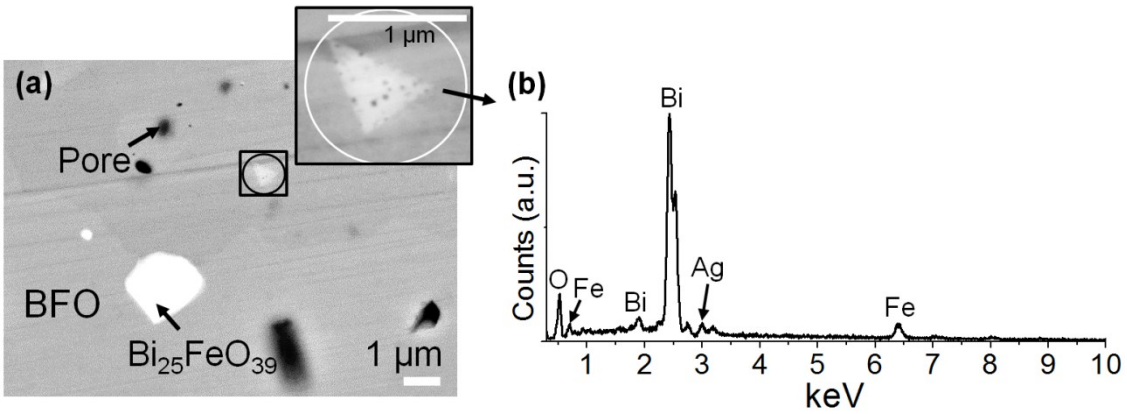


Figure 4.14: BE SEM image of the polished cross-section of BFO/Ag structure sintered at 750 °C (a). EDXS spectrum of the area highlighted with circle (b).

While the observed differences in the microstructure and phase composition of the BFO thick films sintered on Ag, Au and Pt substrates (Fig. 4.13) are probably a result of a number of parameters, we may tentatively explain the density difference and different amount of unreacted Fe_2O_3 between the films by considering thermal stresses during cooling. The metals used as substrates possess different CTE ($\alpha(Pt)=8{,}8\cdot10^{-6}K^{-1}$; $\alpha(Au) = 14{,}2\cdot10^{-6}\ K^{-1}$; $\alpha(Ag) = 18{,}9\cdot10^{-6}\ K^{-1}$)[117] than BFO ($\alpha(BFO) \approx 13{,}3\cdot10^{-6}\ K^{-1}$) (see Chapter 1.2.1.2). According to the differences in the CTE between BFO and the different metals, we expect strong tensile stresses in BFO/Pt, weak compressive stresses in BFO/Au and strong compressive stresses in BFO/Ag, during cooling of the structures. These stresses may explain the high density observed in BFO/Ag (Fig. 4.13a) (compressive case) and the low density with a gradient in porosity observed in BFO/Pt (Fig. 4.13c) (tensile case). A similar effect of the substrate and thus the thermal stresses on the densification of PMN-PT films was observed by Ursic *et al.* [64, 65].

As we are performing reactive sintering we should also consider that the densification could strongly influence the course of the reaction. A low densification means loose contacts between the particles of Bi_2O_3 (or Bi-rich phase) and Fe_2O_3 (or Fe-rich phase), and thus a lower reaction yield and hence a higher amount of unreacted iron oxide in porous BFO/Pt (Fig. 4.13c, inset) compared to the denser BFO/Ag (Fig. 4.13a, inset). In addition, other effects may also be present, such as the effect of pressure on the chemical reaction, pointed out by Selbach *et al.* [38].

The results suggest that the control of thermal stress is particular important in tailoring the BFO film density.

4.3.2 The influence of the sintering or post-annealing temperature on the phase composition and the microstructure

In order to further improve the density of the BFO films, particularly of those on the Au and Pt substrates, we additionally post-annealed the 750 °C-sintered structures BFO/Ag, BFO/Au and BFO/Pt at 820 °C for 2 hours. BE-SEM images of the polished cross-sections of these BFO films on the Au, Pt and Ag substrates are shown in Fig. 4.15.

The densities of the post-annealed BFO films on Au and Pt were significantly improved compared to the films sintered at 750 °C (compare Fig. 4.13b,c with Fig. 4.15a,b). In both samples, however, a small amount of the sillenite phase was detected, irrespective of the sintering temperature. In addition, a higher porosity is observed in the BFO/Pt film compared to that of the BFO/Au (Fig. 4.15b versus Fig. 4.15a) and all the samples exhibited a degree of BFO delamination from the substrate. The delamination was more prevalent in the BFO/Au structure (see Fig. 4.15a). While the origin of this phenomenon is presently unclear, sample preparation for the SEM analysis is suspected as being the influential factor.

As anticipated from the results shown in Fig. 4.14, which confirmed Ag diffusion from the substrate into the BFO film, the BFO film on Ag completely decomposed to sillenite and mullite secondary phases at a higher sintering temperature (820 °C) (Fig. 4.15c). In addition, metallic silver was detected in this film (seen as the grey phase in Fig. 4.15c).

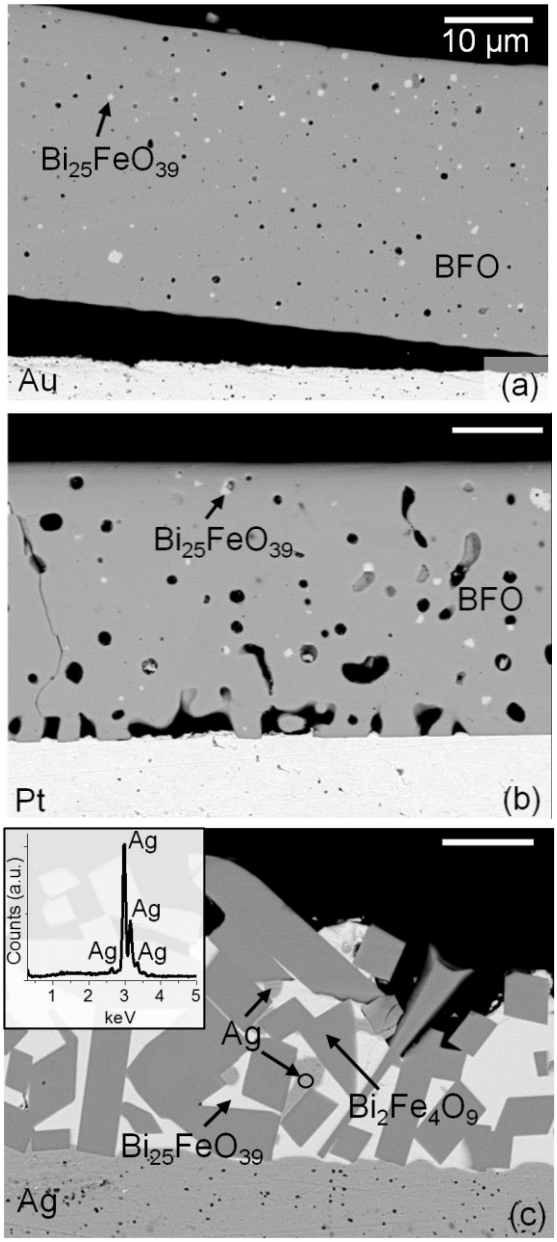


Figure 4.15: BE SEM images of polished cross-sections of BFO/Au (a), BFO/Pt (b) and BFO/Ag (c) thick-film structures sintered at 750 °C for 4 hours and post-annealed at 820 °C for two hours; the inset illustrates an EDXS spectrum taken from the circled area.

In order to reduce the chemical reaction between BFO and Ag, the BFO film was sintered at lower temperature, i.e. at 740 °C, and investigated by SEM/EDXS analysis (Fig. 4.16). The film is characterized by a high density with pores of up to ~2 μm in size. In addition to the perovskite BFO phase, inclusions of the sillenite phase are observed with sizes of ~1 μm. The mullite phase and Fe_2O_3 (not seen in Fig. 4.16) were found only in minor concentrations. The Ag-containing inclusions were not detected in the film. We finally note that the sintering temperature of the BFO thick film on Ag (740 °C) is, respectively, ~100 °C, ~200 °C and ~300 °C, lower than that used for the preparation of $Pb(Zr,Ti)O_3$ [118], $0.65Pb(Mg_{1/3}Nb_{2/3})O_3–0.35PbTiO_3$ [64, 65, 119] and $K_{0.5}Na_{0.5}NbO_3$ [63] thick films using the same screen-printing method.

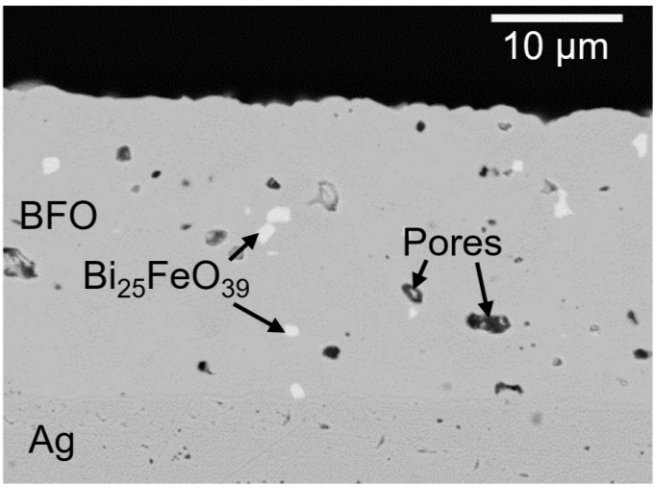


Figure 4.16: BE SEM image of polished cross-sections of BFO/Ag thick-film structure sintered at 740 °C.

To verify the reproducibility, the samples were prepared at least twice at the same sintering conditions and analysed using SEM and XRD analyses. The results were qualitatively consistent, confirming the main conclusions presented in Chapters 4.2 and 4.3.

To conclude, we showed that the use of an appropriate substrate of high purity results in nearly single phase BFO with no segregation of mullite phase at the BFO/substrate interface and no diffusion of bismuth-containing phase into the substrate (compare results in this section with those in Section 4.2). The BFO/Ag thick film structure sintered at 740 °C was selected for further electrical characterization.

4.3.3 Investigation of the electric properties of the $BiFeO_3$ thick film on a Ag foil

4.3.3.1 Macroscopic properties

The BFO/Ag structure sintered at 740 °C was first characterized by measurements of P-E hysteresis loops. Figure 4.17a shows a representative P-E loop of the film measured at the electric-field amplitude of 2.9 kV/cm. At higher amplitudes, the film's response reached the maximum current limit (~20 mA) of the voltage amplifier used for polarization measurements. The rounded shape of the P-E loop, related to a large phase angle δ between the polarization response and the driving sinusoidal electric field, and the anomalously high values of the measured polarization suggest a strong contribution of the leakage current to the response of the film. This conductive behaviour has been also observed in single crystals [19, 120], ceramics [12] and thin films [121, 122] of BFO, and it is most likely associated with the variable oxidation state of Fe ions, i.e., $Fe^{2+}/Fe^{3+}/Fe^{4+}$ [12, 123-125].

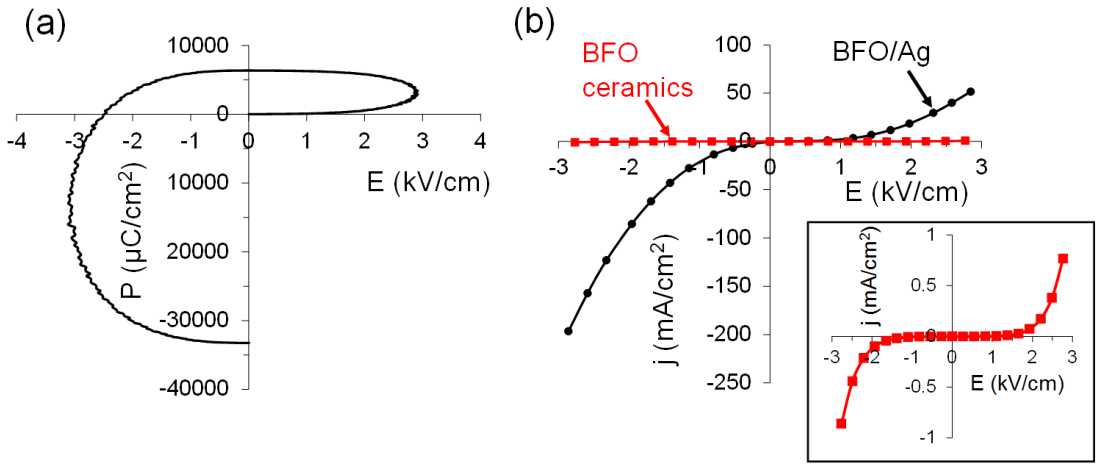


Figure 4.17: Polarization–electric-field (P-E) hysteresis loop of BFO/Ag structure (sintered at 740 °C) measured at 2.9 kV/cm of field amplitude and 1 Hz of field frequency (a), j-E curve of BFO/Ag film (circles) (b) and, for comparison, j-E curve of BFO ceramics (squares), which is additionally shown with enlarged scale in the inset.

To investigate in more detail the electrical conduction behaviour of the BFO/Ag thick film, the j-E response was measured. The j-E curve of the film (Fig. 4.17b, circles) appears nonlinear and asymmetric with respect to the field polarity, i.e., the current density at the maximum DC field of +2.9 kV/cm is 52 mA/cm², whereas that at –2.9 kV/cm is almost four times higher, i.e., 197 mA/cm². In addition to BFO-based thick films [100], this diode-like effect was previously reported for monodomain BFO single crystals [19] and epitaxial BFO thin films [126-129]. In a number of these cases, e.g., in the works of Choi *et al.* [19] and Wang *et al.* [126], the direction of the diode effect was found to be switchable by reversing the spontaneous polarization within domains by applying an above-coercive electric field. A variety of mechanisms have been proposed to explain the diode-like current behaviour in BFO, including differences in the height of the Schottky barriers at the sample/electrode interfaces due to the different bottom and upper electrodes, which might be altered by the presence of mobile charged defects [126, 127, 130], and the presence of defective, e.g., oxygen-vacancy-rich, layers at the interfaces [128]. In the absence of additional evidence, all these scenarios might play a role in the asymmetric j-E behaviour of our BFO thick films, similar to that suggested by Du *et al.* [100].

To verify whether the asymmetric j-E curve is characteristic for the BFO thick film, we performed the same j-E measurements on BFO ceramics sintered at a similar temperature (780 °C) to the BFO/Ag thick films (740 °C). In comparison to the thick film (Fig. 4.17b, circles), the ceramic sample exhibited a still nonlinear but a more symmetric j-E curve (see inset of Fig. 4.17b) with electrical current densities that were up to two orders of magnitude lower than those of the thick film (Fig. 4.17b) for the same applied electric field (2.9 kV/cm). We note that despite the optimized microstructure (see Fig. 4.16), the macroscopic electrical response of the BFO/Ag thick film is characterized by a high conductivity coupled with interface-related, diode-like phenomena.

Since the high electrical conductivity of the BFO/Ag film prevented the application of large electric fields to the sample, which would allow the characterization of the macroscopic ferroelectric properties, a PFM analysis was used to investigate the ferroelectric and piezoelectric behaviour of the film on the local scale.

4.3.3.2 Local properties

The PFM measurements were performed on the bare surface of a BFO/Ag thick-film sintered at 740 °C. The surface topography image (Fig. 4.18a) revealed that the surface roughness of the film is around 0.5 μm. The out-of-plane amplitude PFM image of the BFO surface (Fig. 4.18b) showed that some of the BFO grains exhibited a higher piezoelectric activity than the others; these grains are marked by the green arrows in the image, while grains, which are less piezoelectrically active, are marked with yellow arrows. To show that

the topography is not responsible for the grain-to-grain varying PFM amplitude signal, we highlight the region marked with dashed circles in Fig. 4.18a,b. In this region, both piezoelectric and non-piezoelectric grains are observed (Fig. 4.18b, circled region); however, all these grains are at the same height level (Fig. 4.18a).

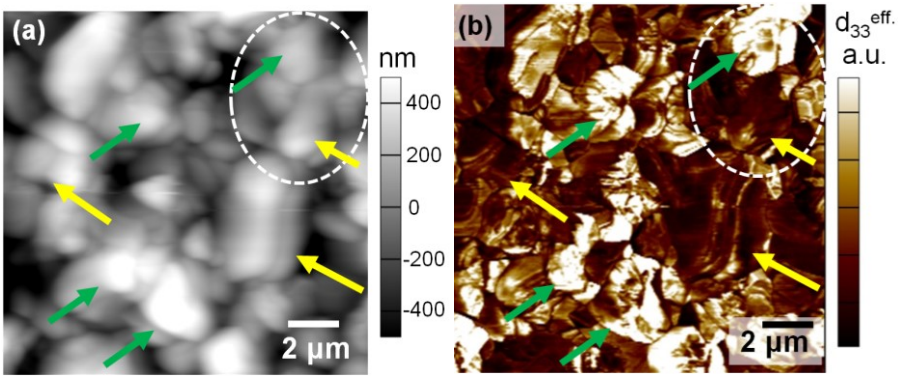


Figure 4.18: Topography (a) and out-of-plane amplitude PFM image (b) of the bare surface of BFO/Ag structure sintered at 740 °C.

Complex, sub-micrometre-sized domain configurations were observed. An example is presented in the out-of-plane amplitude PFM image of the bare BFO surface (Fig. 4.19a,b). The domains with irregular shape, lamellar and wedge-type domains are indicated by a circle in Fig. 4.19a, a square in Fig. 4.19b and an ellipse in Fig. 4.19b, respectively. Note that the grain boundaries can be identified in the amplitude images as sharp boundaries (marked with arrows in Fig. 4.19a,b).

The local piezoelectric activity is evident as the brighter areas within the grains (Fig. 4.19a,b). In order to probe the ferroelectric switching behaviour of the BFO thick film on the Ag substrate, a local d_{33} (V) loop was measured from the area highlighted by a cross in Fig. 4.19a. The local d_{33} (V) loop is shown in Fig. 4.19c and confirms the typical ferroelectric-like hysteretic response of the BFO thick film.

Although the macroscopic electrical response of the ~24-µm-thick BFO film on Ag, sintered at 740 °C, is characterized by a high conductivity (Chapter 4.3.3.1), the ferroelectric behaviour in this film has been confirmed locally with PFM analyses.

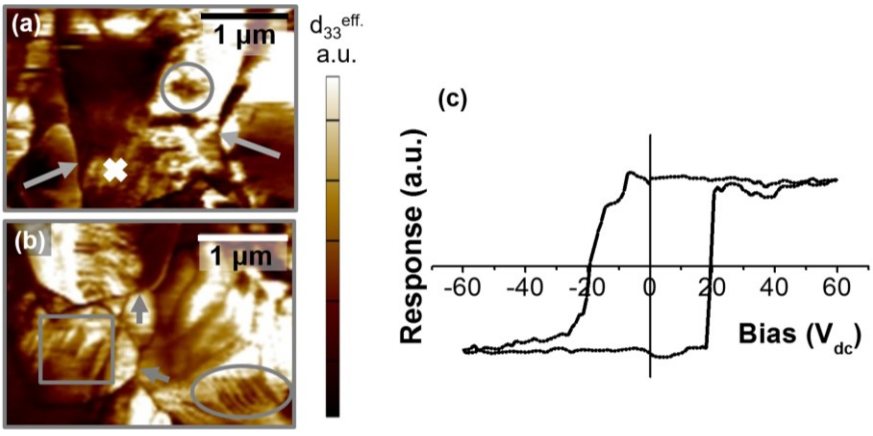


Figure 4.19: Out-of-plane amplitude PFM images of the BFO/Ag structure sintered at 740 °C (a,b), PFM hysteresis loop (c) obtained from the area marked by a cross in the out-of-plane PFM image shown in panel (a). The circles in the PFM images illustrate different domain morphologies, i.e., lamellar- (ellipse), wedge- (square) and island-like (circle) domains.

4.4 Self-Poling Effect in $BiFeO_3$ Thick Films on a Pt/Al_2O_3 Substrate

As shown in the previous chapter, the purity of the substrate plays a crucial role in the preparation of single-phase BFO thick films. As noble-metal foils are costly, for subsequent experiments a less-expensive platinum paste was screen-printed on the alumina, and the prepared Pt/Al_2O_3 structure was used as a substrate. Due to the high conductivity of the BFO films we were only able to measure the local piezoelectric activity of the films. However, to characterize the piezoelectric behaviour of BFO thick films on a macroscopic scale we investigated the possibility of self-poling BFO thick films. In this chapter we provide evidence for the self-poling effect in ~23-µm-thick BFO films screen-printed on a Pt/Al_2O_3 substrate and show that the effect is substantial when the BFO film experiences a ferroelectric-paraelectric phase transition. The key role of this phase transition in the self-poling is demonstrated by comparing thick films sintered slightly below (800 °C) and those sintered slightly above (820 °C) the Curie temperature.

4.4.1 Evidence of the self-poling effect

Before explaining the self-poling effect in the $BFO/Pt/Al_2O_3$ structure, it should be noted that the T_C of the BFO thick films determined here is between 810 °C and 820 °C, which is ~10 °C lower than the T_C reported for BFO bulk ceramics (~830 °C).[1, 3] Similarly, a deviation in the T_C of the thick films in comparison to the bulk ceramics was also reported for $K_{0.5}Na_{0.5}NbO_3$ (KNN),[63] $PbTiO_3$ (PT) [67] and $0.65Pb(Mg_{1/3}Nb_{2/3})O_3–0.35PbTiO_3$ (PMN-PT)[64, 65] thick films. The origin of the lowered T_C in the films, relative to the ceramics, is complex and many fold, and the slight change of 10 °C in the T_C observed here may be a result of a small amount of impurity phases, leading to non-stoichiometric BFO and/or residual stresses in the films.

Thus, BFO thick films sintered slightly below (800 °C) and above (820 °C) the Curie point are characterized and compared. First, we measured a macroscopic direct piezoelectric effect using a standard Berlincourt press on as-sintered BFO films, thus without any prior application of an electric field to the sample. The thick-film structure sintered slightly above the T_C, i.e., at 820 °C, exhibited a macroscopic direct piezoelectric response with $d_{33} = 18 \pm 2$ pC/N. In contrast, the thick film sintered slightly below the T_C, i.e., at 800 °C, revealed a much smaller but still a non-zero piezoelectric response ($d_{33} = 3 \pm 1$ pC/N). The self-poling effect was confirmed by converse piezoelectric measurements, which were performed only after first verifying the self-poling effect with the direct d_{33} measurements; in this way, the self-poling can be distinguished from any poling that might have occurred due to the application of the electric field during converse measurements.

The converse response of both 800°C- and 820°C-sintered thick films was analysed with an oscilloscope and a lock-in amplifier. The measured mechanical displacement signals taken with an oscilloscope as a response to the applied sinusoidal voltage of frequency 10 Hz and amplitude 25 V (corresponding to an electric field amplitude of ~11 kV/cm) are illustrated in Fig. 4.20a,c for the two samples. The thick-film structure sintered at 800 °C did not exhibit any clear periodic displacement signal from the oscilloscope data (Fig. 4.20a); however, a small, in-phase displacement response with respect to the voltage was detected with the lock-in amplifier, resulting in a d_{33} value of ~2 pm/V. This suggests an in-built polarization pointing downwards, thus in the direction from the surface of the films towards the substrate (see schematic in Fig. 4.20b). In contrast, the sample sintered at 820 °C shows a clear piezoelectric response by expanding and shrinking in a sinusoidal form with an amplitude of 0.5 nm, following the waveform of the applied voltage (Fig. 4.20c). The 180° out-of-phase displacement signal with respect to the voltage signal suggests an in-built polarization looking in the opposite direction (upward) to that in the 800 °C-sintered film (see schematic in Fig. 4.20d). The built-in polarization pointed upward in as-sintered films was also observed in epitaxial $BaTiO_3$ [70, 89] and $PbZr_{0.2}Ti_{0.8}O_3$.[69]. Within the limits of the measurement techniques, the converse d_{33} measurements were consistent with the direct d_{33} measurements performed using a standard Berlincourt press. Thus, a difference of only 20 °C in the sintering temperature results in a sharp difference in the amplitude values and the phase of the macroscopic piezoelectric response of the thick films in the as-sintered state.

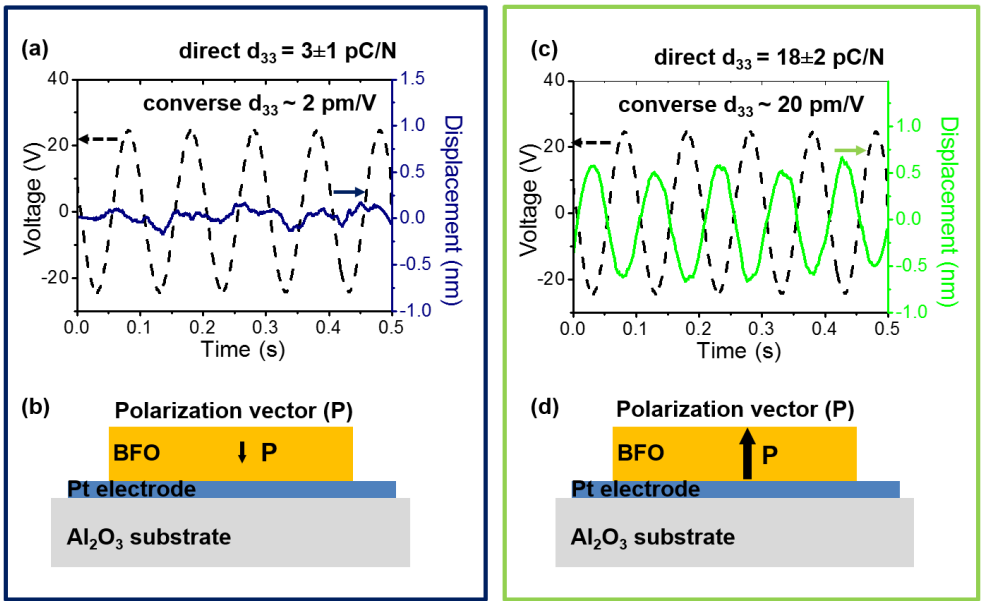


Figure 4.20: Mechanical displacement of the BFO thick-film structures sintered at 800 °C (a) and 820 °C (c) as a function of time under an applied sinusoidal voltage. The schematic representations of the BFO thick films sintered at 800 °C (b) and 820 °C (d) indicate the out-of-plane component of the built-in P determined from phase measurements of the direct and converse piezoelectric response.

In order to verify whether the large difference in the d_{33} responses between the two films indeed originates mostly from the self-poling effect, both the samples were poled at room temperature by the application of an external DC electric field of 50 kV/cm for ~5 minutes. The poling field was applied along the thickness of the films in both the upward and downward directions with respect to the plane of the substrate. After the DC poling, the direct piezoelectric d_{33} coefficient of the BFO thick film sintered at 800 °C was 18±3 pC/N, while that of the sample sintered at 820 °C was 32±3 pC/N. The same values were confirmed for both upward and downward DC poling directions. The results of this experiment lead to two conclusions. First, the DC poling significantly improved the macroscopic piezoelectric response of the sample sintered at 800 °C (d_{33}=3±1 pC/N before DC poling versus d_{33}=18±3 pC/N after DC poling). This confirms that the low d_{33} response of the as-sintered sample at 800 °C (Fig. 4.20a) is indeed related to the weak self-poling effect, considering that a much higher d_{33} coefficient can be achieved by the DC poling. Second, the samples sintered at 800 °C and 820 °C exhibited very different d_{33} values, i.e., 18±3 pC/N and 32±3 pC/N, respectively, despite the same DC field (50 kV/cm) being used for the poling. Such a difference in the macroscopic piezoelectric response can be related to the difference in the microstructure, i.e., different grain size and grain morphology and/or the effects of the residual stresses, which are discussed in detail in Chapters 4.4.2 and 4.4.3.

The appearance of the macroscopic piezoelectricity in the as-sintered samples (Fig. 4.20a,c) should be reflected in the preferred alignment of the ferroelectric/ferroelastic domains along the polar $[111]_{pc}$ axis, which we followed by XRD analysis.[107] The XRD patterns of both thick films, i.e., sintered at 800 and 820 °C, are shown in Fig. 4.21a,c. The thick film sintered at 800 °C is characterized by the intensity of the $(111)_{pc}$ reflection being lower than that of the $(11\bar{1})_{pc}$ reflection with the $(111)_{pc}/(11\bar{1})_{pc}$ intensity ratio ~1/6 (Fig. 4.21b). In contrast, the thick-film structure sintered at 820 °C exhibits a drastic increase in the $(111)_{pc}$ reflection intensity with the $(111)_{pc}/(11\bar{1})_{pc}$ intensity ratio being ~34/1 (Fig. 4.21d). This suggests an increased volume fraction of the $[111]_{pc}$-oriented domains in the out-of-plane film direction in the sample sintered at 820 °C, which is consistent with the larger macroscopic piezoelectric response of this sample (Fig. 4.20c) relative to that of the film sintered at 800 °C (Fig. 4.20a).

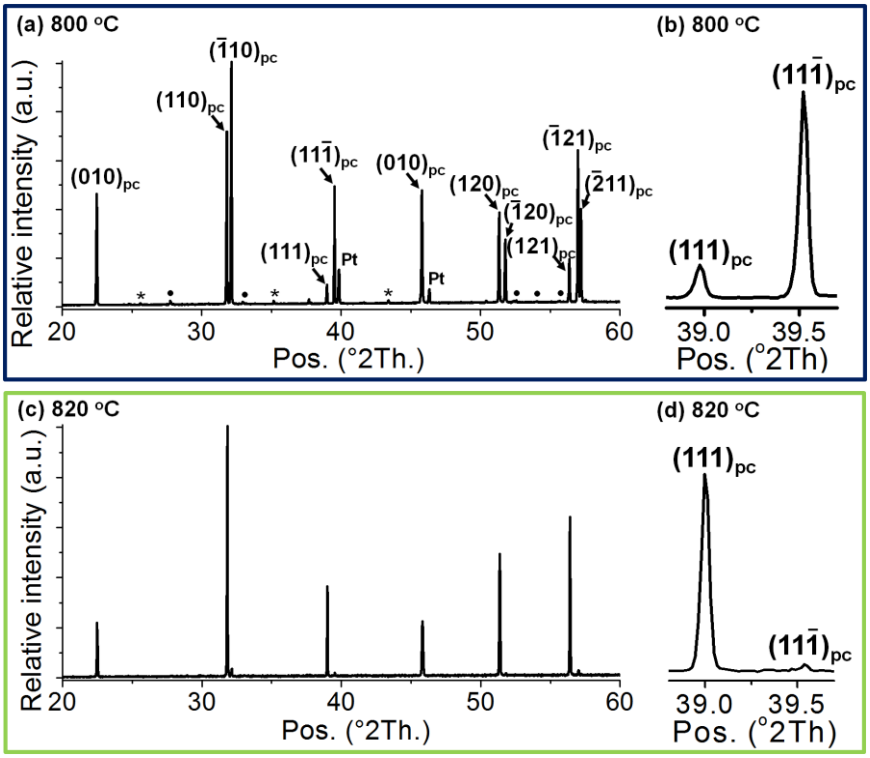


Figure 4.21: XRD patterns of the BFO thick films sintered at 800 °C (a,b) and 820 °C (c,d). The (b,d) panels show the enlarged part of the respective patterns with $\{111\}_{pc}$ peaks. All peaks marked with hkl indices belong to the $BiFeO_3$ phase (PDF No: 01-071-2494); •$Bi_{25}FeO_{39}$ (PDF No: 01-078-1543); * Al_2O_3 (PDF No: 01-088-0826); Pt marks peaks belonging to the Pt electrode.

To evaluate the degree of domain orientation in the two samples, we calculate the volume fraction of the $[111]_{pc}$-oriented domains that were switched from their random orientations to the out-of-plane film direction, η_{111}.[107] In principle, the value of η_{111} lies in the range between –0.25 and 0.75, where the minimum and maximum values correspond, respectively, to the $[11\bar{1}]_{pc}$ and $[111]_{pc}$ orientations of all the domains in the material in a particular direction, and $\eta_{111}= 0$ is expected for non-oriented ceramics with a random distribution of domains inside the grains (for example, in unpoled ceramics). For our thick films sintered at 820 °C and 800 °C, the calculated η_{111} values are 0.73 and –0.08, respectively, indicating a pronounced out-of-plane, $[\bar{1}11]_{pc}$ domain orientation in the sample sintered at 820 °C and a weak out-of-plane, $[11\bar{1}]_{pc}$ domain orientation in the film sintered at 800 °C.

It should be noted that in both samples the perovskite BFO was identified as the major phase, with weak reflections of $Bi_{25}FeO_{39}$ (sillenite) secondary phase appearing in the sample sintered at 800 °C (Fig. 4.21a). The absence of the sillenite phase in the sample sintered at 820 °C (Fig. 4.21c) can be related to the evaporation of the Bi (g)/Bi oxides (g) from the sample surface, as discussed in Chapter 4.2.1. [41] Sintering temperatures of 800 °C and 820 °C, used for the films, are higher than the peritectic decomposition temperature of the sillenite phase, which is ~790°C [109, 110]. Therefore, the sillenite phase is expected to melt during the sintering. The disappearance of the sillenite phase in the thick film sintered at 820 °C (Fig. 4.21c) can be related to the increased evaporation of bismuth oxide from this melt due to the higher sintering temperatures.

To investigate more directly the implication of the ferroelectric-paraelectric phase transition in the self-poling phenomenon in BFO, we performed an in-situ, high-temperature (HT) XRD investigation of the sample sintered at 750 °C. The HT XRD analysis was first performed in the temperature range 780–810 °C (Fig. 4.22a), followed by an analysis in the temperature range 780–840 °C (Fig. 4.22b). After each cycle, the XRD pattern of the sample was recorded at room temperature (RT) (Fig. 4.23).

As shown in Fig. 4.22, we followed the changes in the structure of BFO with increasing temperature focusing on the 2Θ° region from 38.0 to 40.5° where the $(111)_{pc}$ and $(11\bar{1})_{pc}$ reflections appear. No structural change from the initial R3c was observed in the 780–810 °C temperature interval (Fig. 4.22a). On the other hand, the transformation of the crystal structure from the ferroelectric (marked reflection at 38.8° and 39.3°) to the paraelectric phase (unmarked reflections at 39.3° and 39.5°), related to the Curie point, [4, 13, 30] took place in the temperature range 780–840 °C (Fig. 4.22b) (see also the two insets of Fig. 4.22b). Importantly, just after the transformation from the paraelectric to the ferroelectric phase during cooling, the $(11\bar{1})_{pc}$ reflection of the ferroelectric phase reduces almost to the noise level, while the intensity of the $(111)_{pc}$ reflection markedly increases (Fig. 4.22b, bottom inset). Note, however, that just before the transformation to the paraelectric phase during heating, the intensity of the $(11\bar{1})$ was approximately three times higher than that of the $(111)_{pc}$ reflection (Fig. 4.22b, upper inset). This change in the $(111)_{pc}$-to-$(11\bar{1})_{pc}$ intensity ratio strongly suggests that the domain orientation occurs when the film is cooled just below the T_C (Fig. 4.22b).

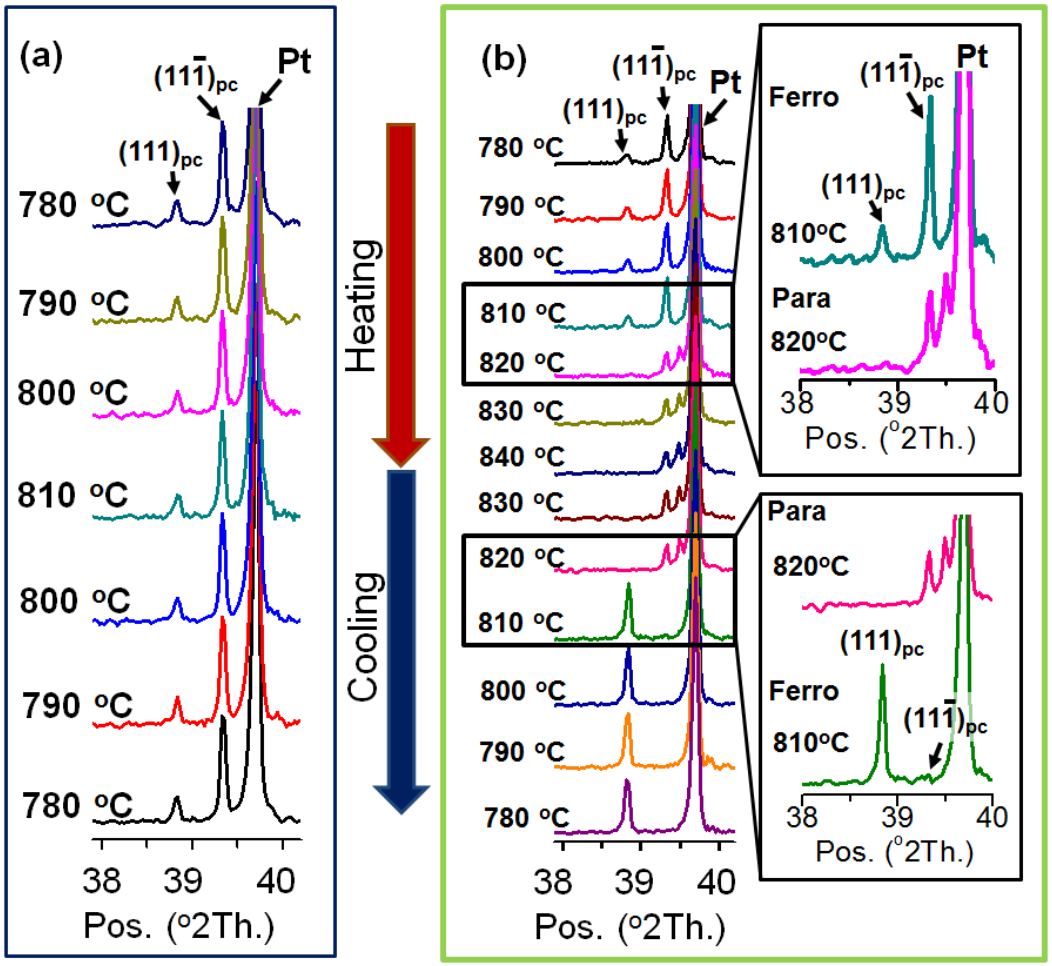


Figure 4.22: *In situ* HT XRD investigation of the BFO thick-film structure sintered at 750 °C. XRD patterns recorded in the heating/cooling cycles in the temperature range 780–810 °C (a) and 780–840 °C (b).

In agreement with the in-situ HT XRD data (Fig. 4.22) are the XRD analyses performed at room temperature after the two in-situ heating/cooling runs (Fig. 4.23). In contrast to the sample sintered at temperatures below T_C (Fig. 4.23d), a strong $[111]_{pc}$ orientation was confirmed at room temperature in the sample annealed and cooled from above T_C (Fig. 4.23f). Using the relative intensities of the $(111)_{pc}$ and $(11\bar{1})_{pc}$ peaks we calculated the volume fraction of the $[111]_{pc}$-oriented domains (η_{111}), which are –0.07 for the as-sintered

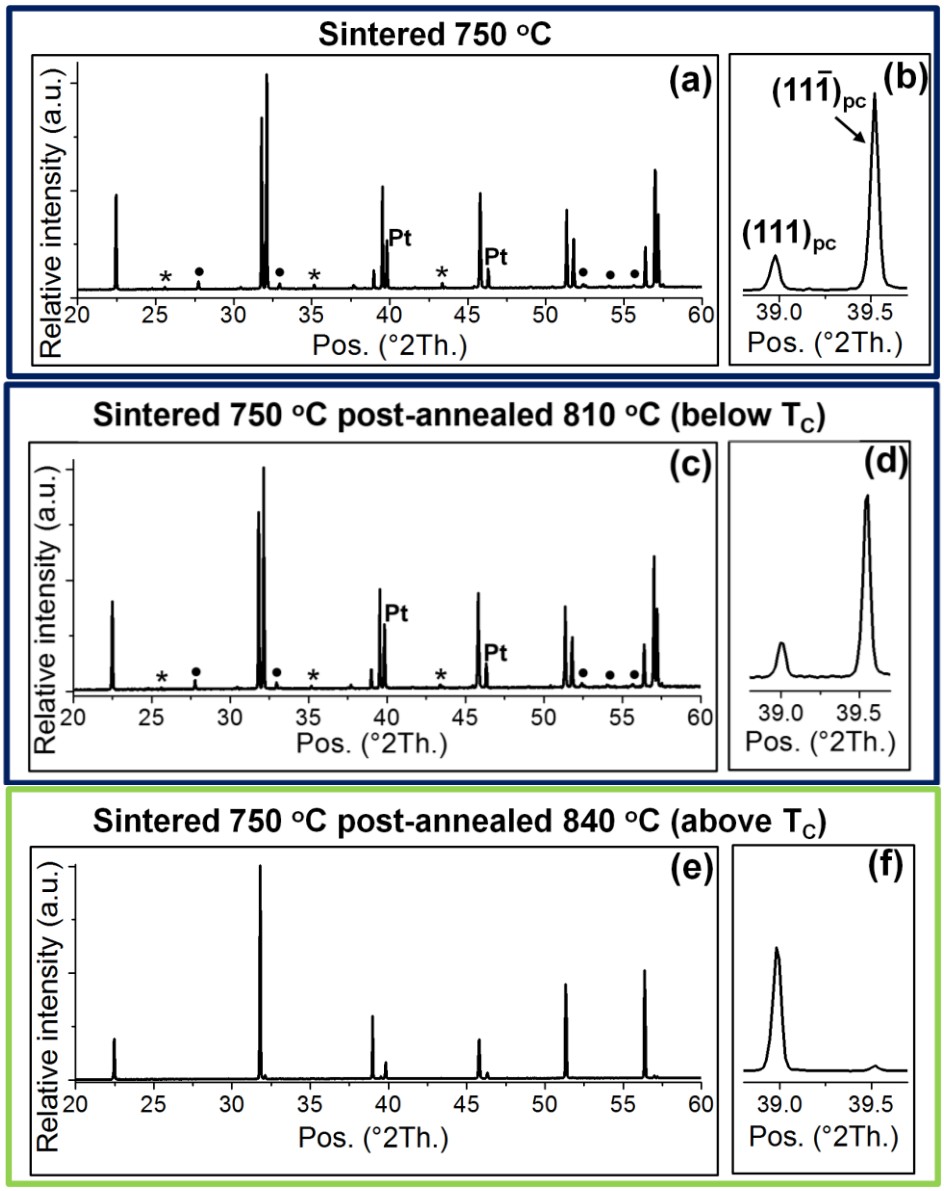


Figure 4.23: XRD patterns at RT of the BFO thick-film structure sintered at 750 °C (a,b), BFO thick-film structure sintered at 750 °C and post-annealed at 810 °C (c,d) and sintered at 750 °C and post-annealed at 840 °C (e,f). The (b,d,f) panels highlight an enlarged region with $\{111\}_{pc}$ peaks. The unmarked peaks belong to the $BiFeO_3$ phase (PDF No: 01-071-2494); •$Bi_{25}FeO_{39}$ (PDF No: 01-078-1543); * Al_2O_3 (PDF No: 01-088-0826) and Pt marks peaks belonging to the Pt electrode.

sample (i.e., before any of the HT XRD cycles), –0.06 after the first HT XRD cycle and 0.71 after the second cycle.

The XRD analysis (Fig. 4.22) provides evidence of a ferroelastic domain texture in the sample, i.e., non-180° switching of the domains from the in-plane to the out-of-plane thick-film direction; however, such an analysis gives no information about the ferroelectric domain texture, i.e., 180° domain switching in either the upward or downward out-of-plane thick-film direction, which is a necessary condition for a non-zero macroscopic piezoelectric response.

To confirm the self-poling of the films, we thus measured the direct piezoelectric response of the samples analysed by HT XRD analysis. The obtained d_{33} values for the as-sintered sample were 0 pC/N, those after first heating/cooling cycle (up to 810 °C) 1 ± 0 pC/N and those for the second heating/cooling cycle (up to 840 °C) 20 ± 3 pC/N. The large

direct d_{33} measured in the samples cooled from above the T_C (20±3 pC/N) and the corresponding drastic increase in the fraction of the out-of-plane $[111]_{pc}$-oriented domains (Fig. 4.23), occurring during cooling just below T_C (Fig. 4.22b, bottom inset), clearly shows that the BFO thick film developed a significant self-poling (d_{33} ~20 pm/V) only after crossing the T_C. The presented experimental results thus confirm that a single post-annealing step (Fig. 4.22b) or direct sintering (Fig. 4.20c) above the T_C leads to a significant self-poling effect.

4.4.2 Investigation of the microstructure

Considering that the XRD analysis and the d_{33} measurements clearly show that a significant self-poling and domain-orientation effects occur in the films that underwent the ferroelectric-paraelectric phase transition, we analyse the microstructure of samples that were sintered at 820 °C (above T_C) and 800 °C (below T_C). The microstructure of the samples was investigated by SEM/EDXS, EBSD and PFM analyses.

An inspection of the SEM surface and cross-section images of the BFO thick films sintered at 800 °C (Fig. 4.24a) and 820 °C (Fig. 4.24b) shows that both films contain the perovskite as the main phase with some inclusions of secondary phases. According to the cross-section SEM images (Fig. 4.24a,b), both films are characterized by a similar, ~30 µm, thickness and porosity. The total porosity calculated from the surface SEM images (Fig. 4.24c,d) is about 5% for both samples, while the pore size is smaller in the film sintered at 800 °C (Fig. 4.24c) compared to the pore size in the film sintered at 820 °C (Fig. 4.24d).

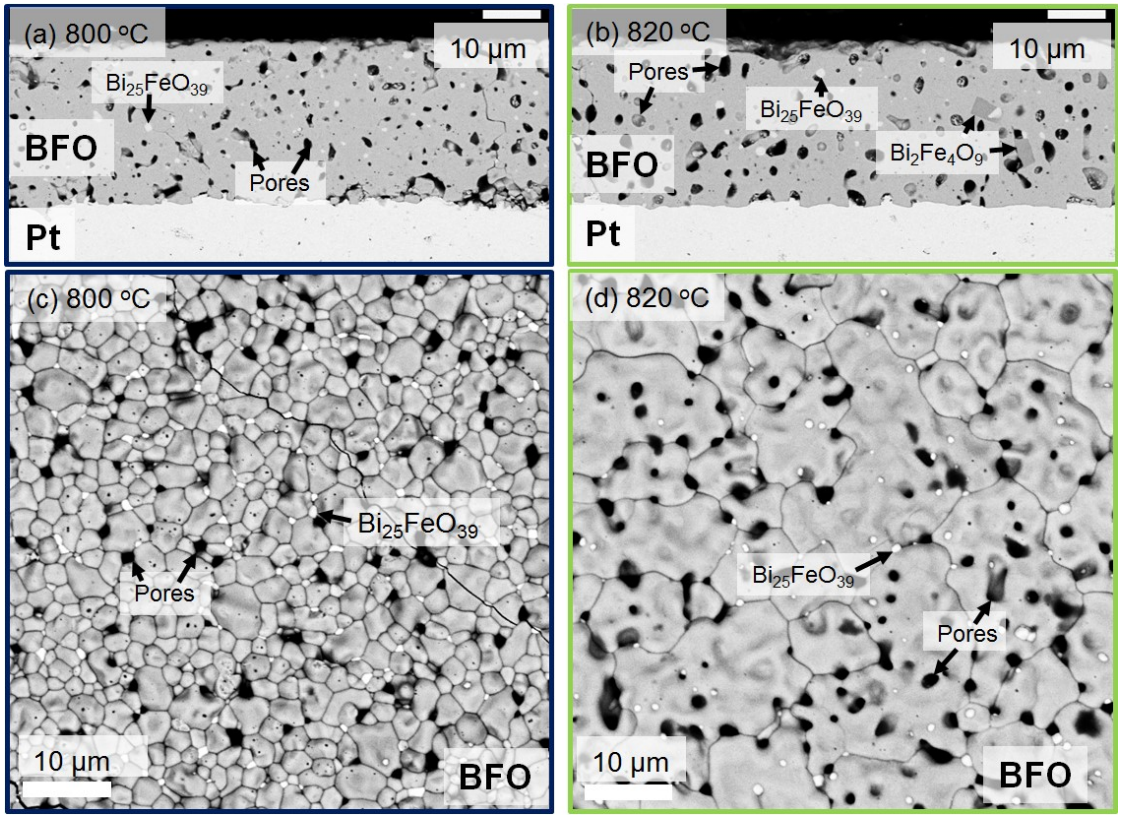


Figure 4.24: BE SEM images of cross sections and surface views of the BFO thick-film structures sintered at 800 °C (a,c) and 820 °C (b,d).

The average in-plane grain size in the films sintered at 800 °C and 820 °C was evaluated from the SEM surface images (Fig. 4.24c,d) and shows a 3-times difference, i.e., 2.6±1.3 μm and 8.7±4.6 μm for, respectively, the 800 °C- and 820 °C-sintered samples. The increase in the grain size is accompanied by a change in the type of porosity; in the case of the film sintered at 800 °C the pores are predominantly intergranular, while in the film sintered at 820 °C the majority of the pores are trapped within the grains, indicating that the grain-boundary migration velocity exceeded the pore migration velocity.[131] In addition, EDXS/SEM analyses were also performed and did not reveal any chemical reactions or interdiffusion between the BFO layer and the Pt electrode.

EBSD analysis was used to investigate the grain size, grain morphology and crystallographic orientation of the BFO films. The results related to the film sintered at 800 °C are shown in Fig. 4.25a,c, while those for the 820 °C-sintered sample are shown in Fig. 4.25b,d. Figure 4.25 illustrates the EBSD orientation inverse pole figure (IPF) maps of the cross-sections and surface views of both samples, showing the BFO grains coloured according to their orientation,[132] and pores or secondary phases as white regions. The film sintered at 800 °C exhibits a microstructure with several equiaxed grains per film thickness (Fig. 4.25a). In contrast, the film sintered at 820 °C possesses coarser columnar grains (Fig. 4.25b) with clearly visible domains, spanning the entire film thickness (Fig. 4.25b, region marked with a dashed rectangle).

The EBSD orientation surface view maps of both thick-film structures, i.e., sintered at 800 °C (Fig. 4.25c) and 820 °C (Fig. 4.25d), reveal a homogeneous distribution of all the orientations (mapped by the different colours), meaning that no preferred crystallographic orientation of the BFO was observed in any of the thick films, despite the difference in the grain morphology (granular versus columnar). The $\{0001\}_{hex}$ pole figures derived from the mappings (insets in the Fig. 4.25c,d) confirm the random crystallographic distribution of both films. Thus, the film sintered at 820 °C exhibits columnar, randomly oriented grains in three dimensions, in which, according to the XRD, the domains have a preferred $[111]_{pc}$ orientation (Fig. 4.21d). The preferred domain orientation was not identified by EBSD, which might be a consequence of the domain re-orientation induced by the mechanical polishing of the sample's surface during the sample preparation for the EBSD analysis.

As a next step, PFM analysis was used to image the domain morphology in the BFO grains in both of the samples. The out-of-plane amplitude PFM image of the film sintered at 800 °C illustrates below-10-μm-sized BFO grains with sub-micrometre-sized irregularly shaped domains (Fig. 4.26a and inset). In contrast, the PFM amplitude image of the film sintered at 820 °C shows few-tens-of-micrometre-sized BFO grains with a diverse domain morphology, such as lamellar-type and irregular-shape domains of different sizes (marked in Fig. 4.26b). As seen from the PFM amplitude image of the surface of this film, some domains percolate through the whole grain (see, for example, the lamellar domain marked with a dashed rectangle in the inset of Fig. 4.26b). Similarly, the EBSD map revealed domains percolating from the Pt/BFO interface to the film surface (marked in the Fig. 4.25b with a dashed rectangle).

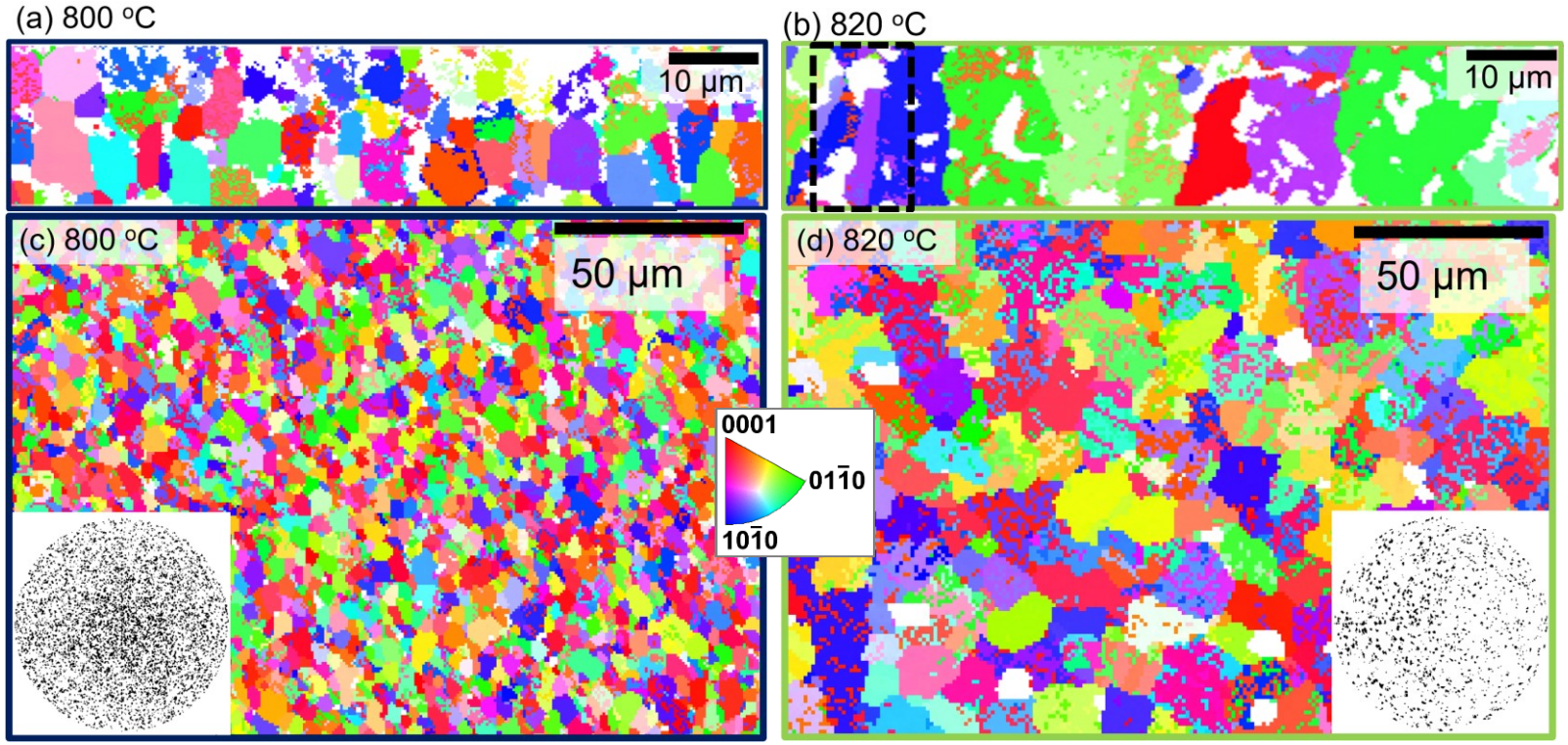


Figure 4.25: EBSD orientation maps of cross-sections (a,b) and surface views (c,d) of the BFO thick films sintered at 800 °C and 820 °C with the corresponding colour-key IPF legend showing Miller Bravais indices for hexagonal symmetry (central inset). Insets on each surface orientation map represent the $\{0001\}_{hex}$ pole figure derived from orientation maps. For the geometrical relationship between the pseudocubic and hexagonal settings see Fig. 1.1d.

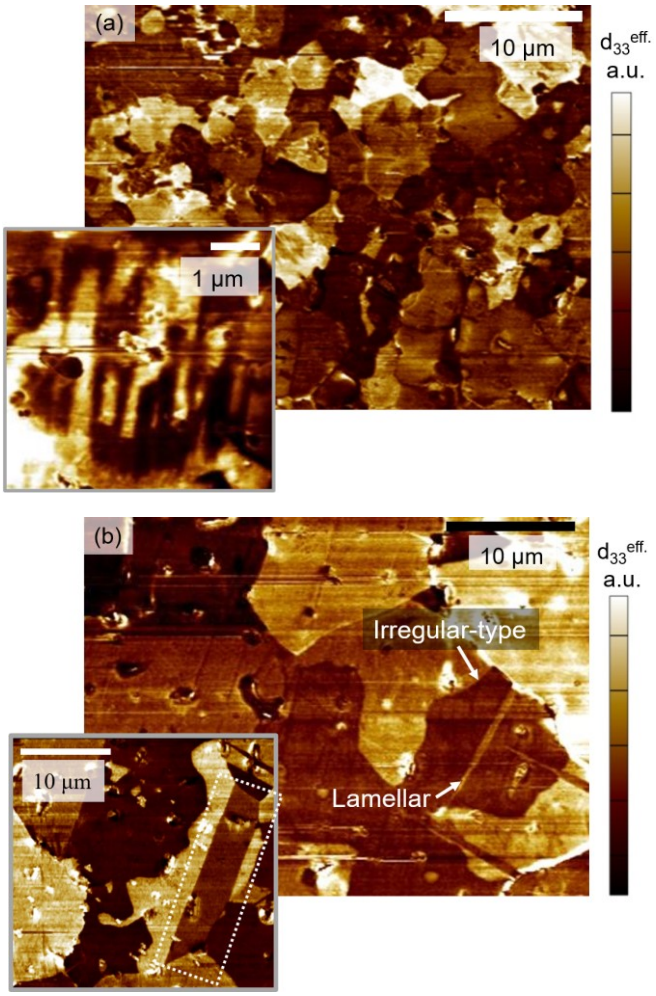


Figure 4.26: Out-of-plane amplitude PFM images of polished surfaces of BFO thick films sintered at 800 °C (a) and 820 °C (b).

In order to verify the influence of temperature of the post-annealing step on the microstructure of the BFO thick film, we additionally analysed the microstructure of the BFO thick film sample sintered at 750 °C and post-annealed either at 810 °C (below T_C) or 840 °C (above T_C). Compared to the 4-h-sintered films, so far described, the post-annealing step at the two selected temperatures was applied for only two minutes. The XRD analyses of these films were explained earlier in Fig. 4.23. We show next in Fig. 4.27 and Fig. 4.28, respectively, the cross-section/surface BE SEM images and the EBSD cross-section orientation map.

The sample sintered at 750 °C and post-annealed at 810 °C exhibited perovskite BFO as a major phase with some sillenite secondary phase inclusions (Fig. 4.27a,c). The result is in accordance with the XRD result shown in Fig. 4.23c, revealing weak sillenite peaks. The grains of several micrometres in size and intergranular porosity are observed in the SEM surface image (Fig. 4.27c). This kind of microstructure is similar to the microstructure of the sample sintered at 800 °C (Fig. 4.24c).

The sample post-annealed at 840 °C exhibits the perovskite BFO as the major phase with some inclusions of the sillenite phase (Fig. 4.27b,d). The surface image of this sample (Fig. 4.27d) shows the irregularly shaped sillenite inclusions preferentially concentrated on the grain boundaries, which implies that the melting of the sillenite phase took place during the post-annealing step at 840 °C. A small amount of the liquid sillenite phase (Fig. 4.27d), suggests increased evaporation of the volatile bismuth oxide from the surface of the BFO thick film. These results are in accordance with the XRD analysis (Fig. 4.23e), where no sillenite phase was detected. Relative to the sample post-annealed at 810 °C, the microstructure of the sample, which experienced the ferroelectric-paraelectric phase

transition during the post-annealing step at 840 °C, changed drastically: the grains are coarser with a size of several tens of micrometres and the pores are trapped inside the BFO grains (Fig. 4.27d).

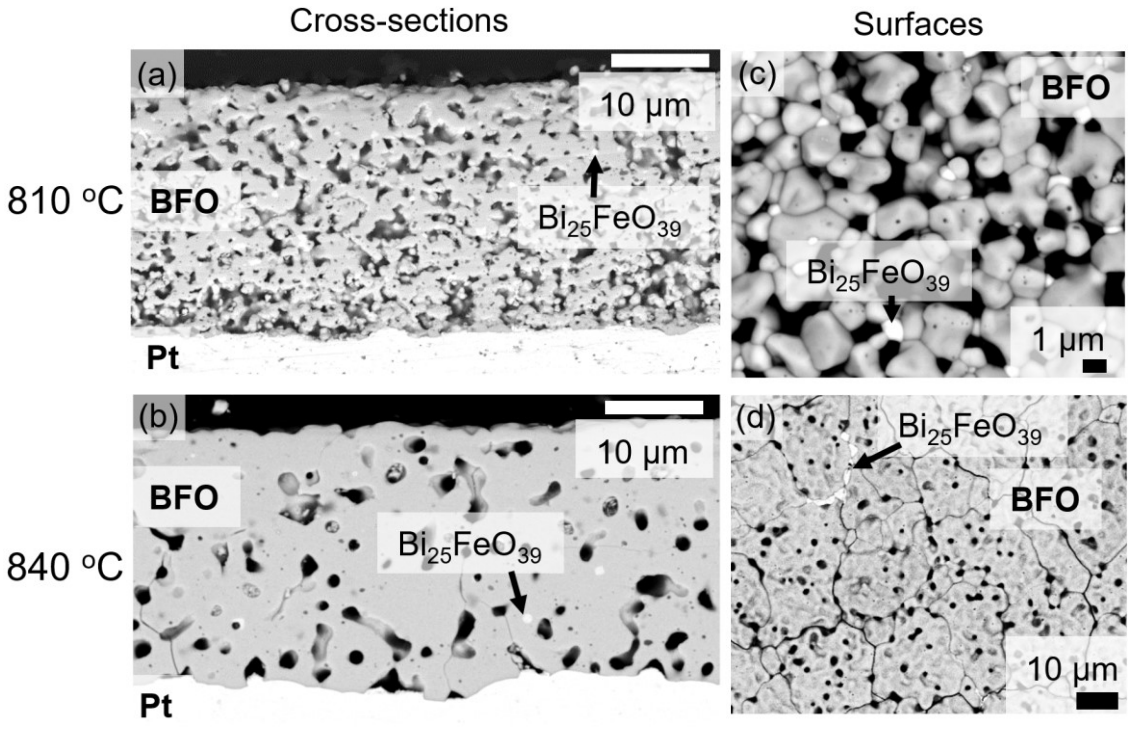


Figure 4.27: BE SEM images of the cross-sections (a,b) and surface views (c,d) of BFO thick-film structure sintered at 750 °C and post-annealed either at 810 °C (a,c) or 840 °C (b,d).

Similar as for the BFO films directly sintered at 820 °C, the BFO thick films post-annealed at 840 °C for only two minutes, exhibited large columnar grains spanning across the film thickness with clearly observed domains, as shown in the EBSD orientation maps (Fig. 4.28).

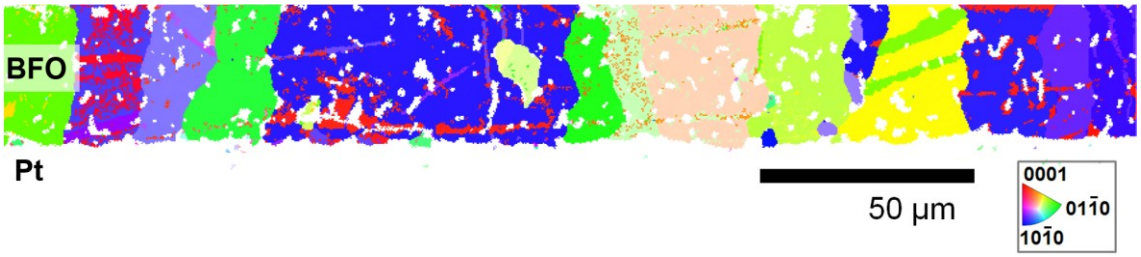


Figure 4.28: EBSD orientation maps of cross-section of BFO thick film sintered at 750 °C and post-annealed at 840 °C with the corresponding colour-key IPF legend showing Miller Bravais indices for hexagonal symmetry (inset).

The presented results suggest that the grain size, grain morphology and type of porosity (inter- or intragranular) are strongly related to whether the film experienced the ferroelectric-paraelectric phase transition either during sintering or post-annealing; namely, the coarser grains and intragranular porosity were observed in all the films that were cooled from above this phase transition. Finally, it is possible that the distinct type of the microstructure of the films (equiaxed versus columnar, see Fig. 4.25) has an impact on the thick-film piezoelectric response (see the DC poling experiments in Chapter 4.4.1).

4.4.3 Strain gradient in $BiFeO_3$ thick films

Strain gradients were reported to lie at the origin of the self-poling effect in several cases in thin films and bulk ceramics [69-71, 86, 89]. The BFO thick-film structure sintered above T_C exhibited a pronounced self-poling effect, thus, we used high-resolution (HR) TEM imaging and selected area electron diffraction (SAED) technique for investigation of the change in the unit-cell parameters across the thickness. The analysed sample was sintered at 820°C.

Fig. 4.29a presents a low-magnification BF TEM image of a BFO grain on the Pt with the marked interface between them. The HR TEM image of the enlarged view of BFO/Pt interface with a part of the same BFO grain is shown in Fig. 4.29b. In the enlarged region of the grain (highlighted by a rectangle in Fig. 4.29b) shown in Fig. 4.29c the in-plane $[001]_{pc}$ and out-of-plane $[\bar{1}10]_{pc}$ directions of the analysed BFO grain relative to the substrate are marked.

In order to investigate the variation of the in-plane and out-of-plane unit-cell parameters of rhombohedral BFO throughout the film thickness, we performed a set of SAED analyses for areas of ~0.5 μm in diameter for one selected domain. Circles in Fig. 4.29a highlight the four areas along the BFO film thickness from where the SAED patterns were acquired. SAED patterns were indexed using a pseudo-cubic BFO unit cell, where the $(001)_{pc}$ and $(\bar{1}10)_{pc}$ d-spacing values were measured.

Fig. 4.29d illustrates the change in d-spacing along the thickness of a single grain. The change is presented as a relative d/d_0 value, where d_0 is the value obtained from the area closest to the surface of the film, i.e., 2 μm away from the BFO/Pt interface, as indicated in Fig. 4.29a (circled region 4). The d/d_0 versus distance clearly demonstrates that both the $(001)_{pc}$ and $(\bar{1}10)_{pc}$ interplanar spacings of the BFO reduce towards the BFO/Pt interface by 0.55%. The result thus shows that the unit-cell parameters are not constant across the grain (film) thickness, suggesting the presence of a gradient of compressive strain in both the in-plane and out-of-plane directions relative to the substrate plane. The origin of this triaxial strain is not understood, but it has been reported in the literature for TiN [133, 134] and Cu [135] films, and might be associated with the grain-to-grain elastic coupling [107], particularly because our films are polycrystalline with grains of random orientation (see EBSD results, Fig. 4.25).

A strain of 0.55% developing within a distance of ~2 μm results in a strain gradient of $\sim 2.7\times10^{3}$ m^{-1}. Worth noting is that the strain gradient in the BFO thick film is three orders of magnitude smaller than that reported for epitaxial thin films, ($\sim 10^{6}$ m^{-1} [68]), and four orders of magnitude higher than that estimated in bulk ceramics (~0.1 m^{-1} [68]).

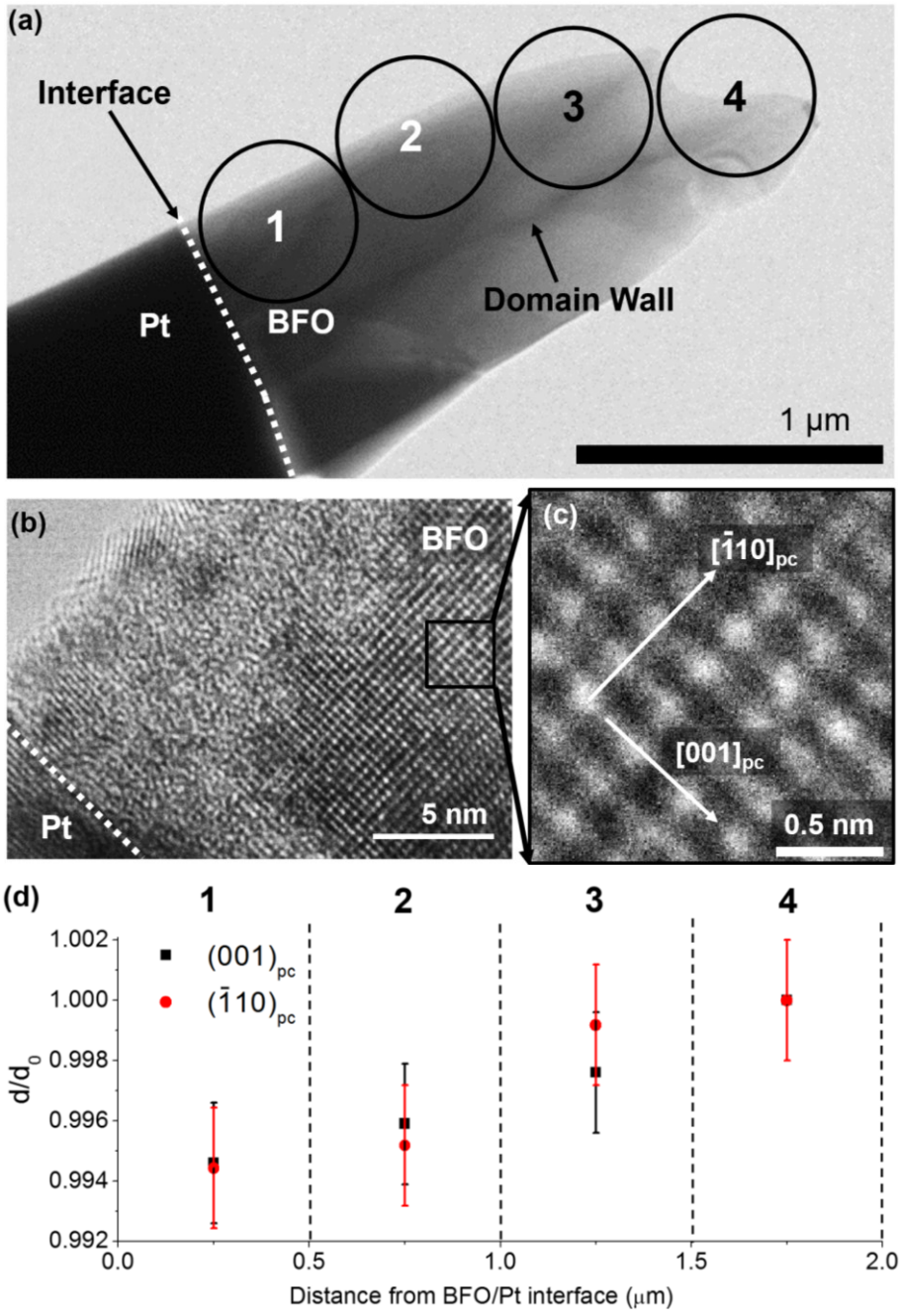


Figure 4.29: BFO/Pt/Al_2O_3 structure sintered at 820 °C: Low-magnification BF TEM image of the BFO/Pt interface, circles indicate areas where SAED patterns were acquired (a). HR TEM image of BFO grain in the $[110]_{pc}$ zone axis near the film-substrate interface (b); enlarged area showing out-of-plane $(\bar{1}10)_{pc}$ and in-plane $(001)_{pc}$ direction relative to the substrate plane (c). Variation of normalized $(001)_{pc}$ and $(\bar{1}10)_{pc}$ d-values calculated from SAED patterns through the film thickness (d). Error bars represent 0.2% uncertainty evaluated from the stress-free ceramic (see the experimental part, Chapter 3.3.5.2).

As TEM is a local technique, we additionally studied the change in the out-of-plane unit-cell parameter by XRD analysis in BFO films with different thicknesses. Fig. 4.30 shows the $(001)_{pc}$ peak of the 6-, 17-, 23- and 40-µm-thick BFO films sintered at 750 °C and post-annealed at 850 °C. The $(001)_{pc}$ peak position is changing with the thickness of the BFO film; the thinner is the BFO layer the more the peak is shifted to the higher 2Θ values, i.e., to the smaller d-spacing. Therefore, a decrease in the out-of-plane BFO unit-cell parameter is observed with the decreasing film thickness. This result is in agreement with the TEM analysis, where a decrease in both the in-plane and out-of-plane d-spacings of the BFO was observed (Fig. 4.29d) as the substrate was approached. In addition to the change in the peak position, a peak broadening was also observed, which is more significant as the film thickness is reduced (Fig. 4.30). This peak broadening is a convolution of the effects of microstrain and the reducing thickness of the film.

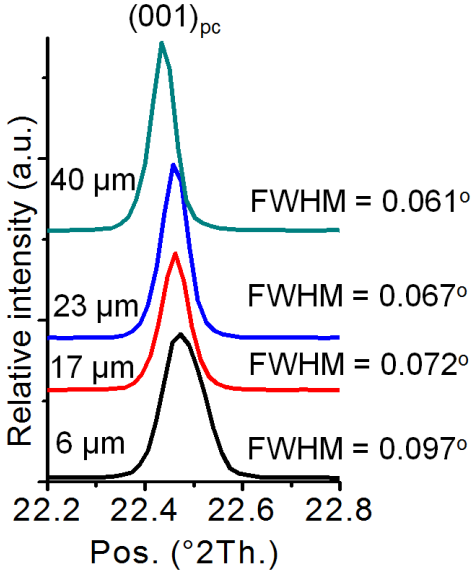


Figure 4.30: XRD patterns showing $(001)_{pc}$ peak of BFO film with different thickness sintered at 750 °C and post-annealed at 850 °C.

4.4.4 Discussion of the self-poling effect

The results confirm a macroscopic direct and converse piezoelectric response in as-sintered BFO thick films (Chapter 4.4.1) where the magnitude and direction of the built-in polarization appears to be dependent on the temperature from which the sample was cooled. BFO thick films cooled from above the T_C exhibit an upward polarization and a direct d_{33} of up to 20 pC/N. Worth noting is that this d_{33} value represents 45% of the d_{33} measured in well-poled BFO ceramics, i.e., 44 pC/N [41], and that this fraction is higher than that observed in thick films of PMN-PT and "soft" PZT (~20–30 %) poled with external electric fields. Consistent with the self-poling effect is the preferred $[111]_{pc}$ domain orientation developing out-of-plane during the cooling just below the T_C (Fig. 4.22b). In contrast, films that did not experience the ferroelectric-paraelectric phase transition exhibited a weak self-poling effect (Fig. 4.20a) with a direct d_{33} of 3 pC/N and the out-of-plane component of the polarization looking downward, i.e., towards the substrate (Chapter 4.4.1).

The difference in the self-poling effect in the films sintered below and above the T_C may be explained by different sources of thermal stresses in these films as schematically shown in Fig. 4.31. In the following, we show a simplified quantitative estimation of the residual strains in the films which, however, explains the observed differences in the crystallographic orientation and magnitude of the self-poling effect between the two films.

In the case of the BFO thick film sintered below the T_C, stresses induced by the thermal expansion coefficient (CTE) mismatch between the thick film and the substrate material should be considered because they are known to have a great impact on the phase composition,[64, 65] crystal structure [63, 66] and piezoelectric properties of ferroelectric thick films[66]. According to the linear CTEs (25–800 °C), which are $\alpha(Pt)$ =10.0×10^{-6} K^{-1} for Pt,[117] $\alpha(Al_2O_3)$ =8.2×10^{-6} K^{-1} for Al_2O_3,[136] and $\alpha(BFO)$ =~13.3×10^{-6} K^{-1} for BFO,[30] (Chapter 1.2.1.2) the BFO thick film should be under tensile stress during cooling (Fig. 4.31a). The residual tensile strain related to the difference in CTEs (e_{CTE}) developed in the BFO film during cooling from 800 to 25 °C can be estimated as:

$$e_{CTE} = [\alpha(Pt) - \alpha(BFO)] \times [T_{sint} - T_{RT}] \quad (4.1)$$

where T_{sint} = 800 °C, T_{RT}=25 °C. As shown in Fig. 4.31a the strain calculated with the formula 4.1 is −0.26% (negative sign indicates tensile strain). This substrate-related tensile strain might be responsible for the slight orientation of the $[11\bar{1}]_{pc}$ domains in the out-of-plane film direction (see Fig. 4.21b) and weak downward self-poling (see Fig. 4.20a,b), although the exact mechanism is not clear.

In the case of self-poled films, which were cooled through the ferroelectric-paraelectric phase transition, in addition to stresses related to the difference in CTEs (equation 4.1), the stresses associated with the ferroelectric-paraelectric phase transitions should be taken into account, as shown schematically in Fig. 4.31b. The ferroelectric-paraelectric phase transition of the BFO is strongly first order in nature and is accompanied by a large change in the primitive unit-cell volume, i.e., ~1.5%, which corresponds to ~0.5% of linear expansion of the BFO unit cell.[4, 13, 30] As this expansion of the BFO unit cell during the transformation from the paraelectric to the ferroelectric phase is hindered due to substrate-related clamping of the film (providing the stresses relax at $T > T_C$), a compressive strain of +0.5% (positive sign indicates compressive strain) should develop in the film just by cooling it from above T_C (°C) to a temperature just below T_C (800°C). The total strain at room temperature, e_{RT}, is therefore a sum of the transition-related compressive strain, e_{TR}, and the tensile strain related to the difference in CTEs, e_{CTE}, as shown in equation 4.2:

$$e_{RT} = e_{TR} + e_{CTE} \quad (4.2)$$

The calculated total strain at room temperature is thus $e_{TR} = +0.24\%$.

This proposed mechanism is consistent with the compressive strain observed at room temperature in the vicinity of the bottom-electrode/BFO interface (Fig. 4.29d). Considering that the film is clamped to the substrate, we expect the stresses to decay towards the surface of the film, resulting in a strain gradient, as effectively measured (Fig. 4.29d). Likewise, the observed strain gradient is responsible for the strong orientation of the $[111]_{pc}$ domains in the out-of-plane film direction (Fig. 4.21d) and the pronounced upward self-poling effect (Fig. 4.20c,d) in BFO tick-films cooled from above T_C.

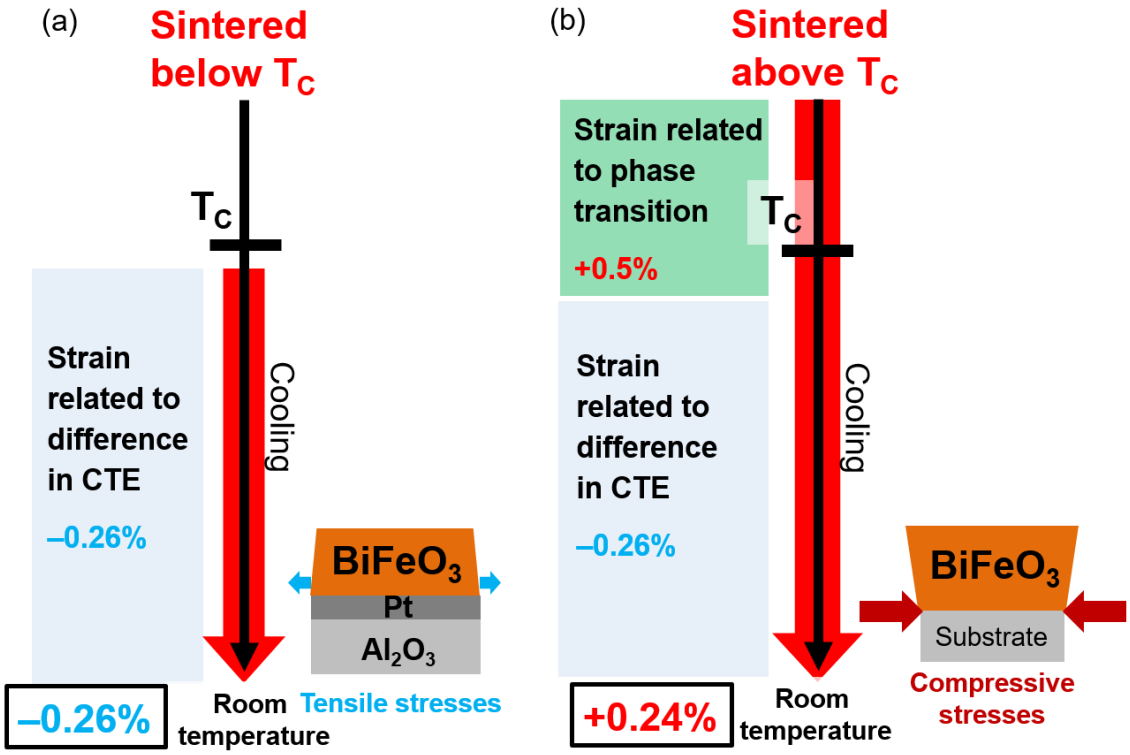


Figure 4.31: Schematic illustration of the strain-developing mechanism in BFO thick films sintered below (a) or above T_C (b).

While the experimental data presented here strongly suggest a relationship between the significant self-poling in BFO films and the strain gradient associated with the stresses induced by crossing the ferroelectric-paraelectric phase transition, there are various mechanisms by which the strain gradient may lead to self-poling, for example, through the flexoelectric effect (called flexoelectric poling)[71, 88] and/or the redistribution of charged defects.[70, 86, 87, 89] We also note that the observed significant change in the microstructure of the film (from an equiaxed to a columnar grain morphology) by cooling through the T_C (Fig. 4.27 and 4.28), can also be a result of the strain distribution in the film and possibly related to the self-poling effect, though the exact mechanisms are still to be investigated.

4.4.5 Characterization of macroscopic piezoelectric behaviour of the self-poled $BiFeO_3$ thick films

For a comparison with the piezoelectric response of the BFO ceramics [137] and to gain insights into the domain-wall contributions and the piezoelectric dissipation processes in self-poled BFO films, we next show the longitudinal d_{33} coefficient and piezoelectric phase angle, tanδ, of the BFO thick film sintered at 750 °C and post-annealed at 840 °C, measured as a function of the frequency and amplitude of the applied electric field (Fig. 4.32).

The piezoelectric response of the BFO thick film shows a sequence of increasing and decreasing d_{33} and piezoelectric tanδ with the driving frequency (see Fig. 4.32a). Complex piezoelectric dispersions have also been observed in BFO ceramics [137]; however, in that case the d_{33} and piezoelectric tanδ showed larger variations in the same frequency range (1–200 Hz) and for the same driving amplitude (~10 kV/cm). Interestingly, the piezoelectric response of the thick film at low frequency (Fig. 4.32b, 1 Hz) is linear (d_{33} independent of the electric-field amplitude in the range from 4 to 11 kV/cm). This is in contrast to the behaviour of BFO ceramics, which exhibit a significant nonlinear response, particularly at low frequencies (< 5 Hz), [137] related to irreversible displacements of the conductive non-180° domain walls. The linear d_{33} response of the BFO film (Fig. 4.32b) and the weak dispersion in d_{33} (Fig. 4.32a) relative to the BFO ceramics, could be related to the

clamping of the film to the substrate, which may provide elastic pinning of the non-180° domain walls, limiting their mobility under an applied field.[138, 139] The clamping effect of the substrate is expected to decay from the substrate/film interface towards the surface of the film, which is consistent with the observed strain gradient along the thickness of the film (Fig. 4.29d). A similar effect of the substrate clamping on the d_{33} response was reported for KNN thick films.[63]

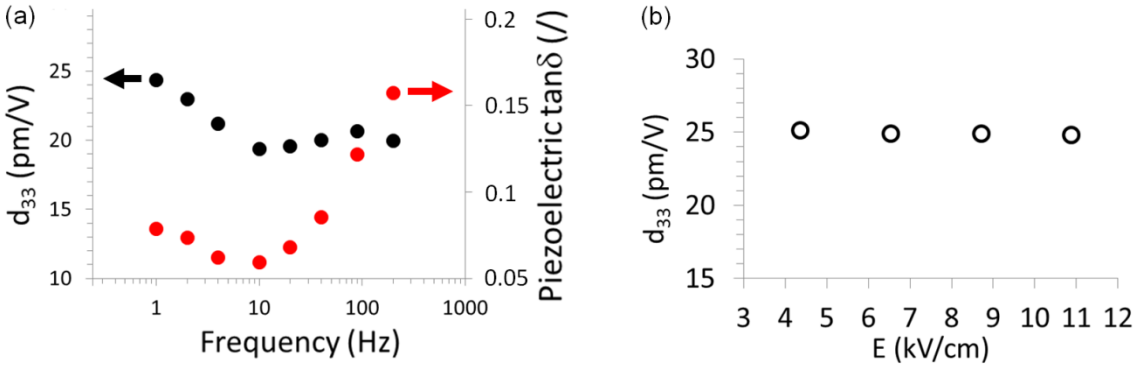


Figure 4.32: Piezoelectric d_{33} and tanδ of the BFO thick film sintered at 750 °C and post-annealed at 840 °C as a function of the driving-field frequency measured at ~11 kV/cm of field amplitude (a). The d_{33} of the film as a function of the amplitude of the driving field measured at 1 Hz of frequency (b).

Chapter 5

Summary and Conclusions

In first two chapters of the PhD thesis we demonstrated the important role of the processing conditions on the microstructure and phase composition of BFO thick films.

First, we studied the phase composition and phase distribution in BFO thick films on Au/Al_2O_3 substrate as a function of the sintering temperature. We showed that by optimizing the sintering temperature we can significantly reduce the amount of secondary phases in the BFO thick films. At temperatures as low as 750 ^oC, a nearly single-phase BFO was produced. Various mechanisms were proposed to explain the formation of Bi- and Fe-rich secondary phases present in the films annealed below or above 750 ^oC. At elevated temperatures ($\geq$ 800 ^oC) several processes took place, including diffusion of the Bi-rich phase into the Al_2O_3 substrate, evaporation of bismuth oxide from the BFO film surface and segregation of the sillenite phase ($Bi_{25}FeO_{39}$). In addition, chemical reactions with impurities from the Au electrode caused the formation of the mullite ($Bi_2Fe_4O_9$) phase, and its segregation at the BFO/Au electrode interface. Based on these results we can conclude that in order to avoid the degradation of the phase composition of BFO thick films, particularly at the film/electrode contact, higher purity electrode and substrate materials are required.

Later on, interactions between the BFO thick films and high-purity Ag, Au or Pt metal substrates were studied. While the XRD analysis revealed an almost single phase composition for all three films sintered at 750 ^oC, the SEM analysis showed that the density, microstructure and phase composition of films differ significantly depending on the type of substrate. The post-annealing step at 820 ^oC for 2 hours improved the BFO's density on Au and Pt substrates but, due to chemical reactions, this led to a complete compositional degradation of the BFO film on Ag.

By optimizing the annealing temperature (740 ^oC) we successfully prepared a dense and nearly single-phase, ~23-μm-thick BFO film on a high purity Ag metal substrate. Although the macroscopic electrical response of this film was characterized by high conductivity, the ferroelectric behaviour of the BFO was confirmed locally using PFM analysis.

In the last part of the PhD thesis we reported on a self-poling effect in BFO thick films on Pt/Al_2O_3 substrates. Through measurements of the direct and converse piezoelectric responses, and an XRD analysis of domain orientation in the films, we presented evidence that the self-poling in BFO thick films is closely linked to the sintering (or post-annealing) temperature and to the strain gradient developed in the film. Significant self-poling only appeared when the material was annealed and cooled through the ferroelectric-paraelectric phase transition ($T_C \sim 820$ °C). Passing through the T_C was also accompanied by an abrupt change in the microstructure: the thick film cooled from above the T_C exhibited a columnar grain morphology, while those cooled from below the T_C had equiaxed grains. The thick films that experienced the ferroelectric-paraelectric phase transition revealed the presence of a compressive strain gradient across the film thickness, which was suggested to be responsible for the appearance of the self-poling effect. In sharp contrast to BFO ceramics, the macroscopic piezoelectric response of the self-poled BFO film showed a linear, field-independent d_{33} response, possibly related to the clamped state of the film.

References

[1] J. M. Moreau, C. Michel, R. Gerson and W. J. James, "Ferroelectric $BiFeO_3$ X-ray and neutron diffraction study," *Journal of Physics and Chemistry of Solids*, vol. 32, no. 6, pp. 1315–1320, 1971.

[2] J. D. Bucci, B. K. Robertson and W. J. James, "Precision determination of the lattice parameters and the coefficients of thermal expansion of $BiFeO_3$," *Journal of Applied Crystallography*, vol. 5, pp. 187–191, 1972.

[3] S. M. Selbach, T. Tybell, M. A. Einarsrud, T. Grande, "Phase transitions, electrical conductivity and chemical stability of $BiFeO_3$ at high temperatures, " *Journal of Solid State Chemistry*, vol. 183, no. 5, pp. 1205–1208, 2010.

[4] D. C. Arnold, K. S. Knight, F. D. Morrison and P. Lightfoot, "Ferroelectric-paraelectric transition in $BiFeO_3$: crystal structure of the orthorhombic phase" *Physical Review Letters*, vol. 102, no. 2, pp. 027602–1–4, 2009.

[5] M. Polomska, W. Kaczmarek and Z. Pająk, "Electric and magnetic properties of $(B_{1-x}La_x)FeO_3$ solid solutions," *Physica Status Solidi A-Applications and Materials Science*, vol. 23, no. 2, pp. 567–574, 1974.

[6] G. A. Smolenskii and V. M. Yudin, "Weak ferromagnetism of some $BiFeO_3$–$Pb(Fe_{0.5}Nb_{0.5})O_3$ perovskite," *Soviet physics-Solid state*, vol. 6, pp. 2936–2942, 1965.

[7] G. Catalan, J. F. Scott, "Physics and applications of bismuth ferrite", *Advanced Materials*, vol. 21, no. 24, pp. 2463–2485, 2009.

[8] H. Bea, M. Gajek, M. Bibes and A. Barthelemy, "Spintronics with multiferroics," *Journal of Physics: Condensed Matter*, vol. 20, no. 43, pp. 434221–1–11, 2008.

[9] J. B. Neaton, C. Ederer, U. V. Waghmare, N. A. Spaldin and K. M. Rabe, "First-principles study of spontaneous polarization in multiferroic $BiFeO_3$," *Physical Review B*, vol. 71, no. 1, pp. 014113–1–8, 2005.

[10] D. Lebeugle, D. Colson, A. Forget, and M. Viret, "Very large spontaneous electric polarization in $BiFeO_3$ single crystals at room temperature and its evolution under cycling fields," *Applied Physics Letters*, vol. 91, no. 2, pp. 022907–1–3, 2007.

[11] N. Setter, D. Damjanovic, L. Eng, G. Fox, S. Gevorgian, S. Hong, A. Kingon, H. Kohlstedt, N. Y. Park, G. B. Stephenson, I. Stolitchnov, A. K. Tagantsev, D. V. Taylor, T. Yamada and S. Streiffer, "Ferroelectric thin films: review of materials, properties, and applications," *Journal of Applied Physics*, vol. 100, no. 5, pp. 051606–1–46, 2006.

[12] T. Rojac, A. Bencan, B. Malic, G. Tutuncu, J. L. Jones, J. E. Daniels and D. Damjanovic, "$BiFeO_3$ Ceramics: Processing, Electrical, and Electromechanical Properties," *Journal of the American Ceramic Society*, vol. 97, no. 7, pp. 1993–2011, 2014.

[13] R. Palai, R. S. Katiyar, H. Schmid, P. Tissot, S. J. Clark, J. Robertson, S. A. T. Redfern and J. F. Scott, "The β phase of multiferroic bismuth ferrite and its γ-β metal-insulator transition," *Physical Review B*, vol. 77, no. 1, pp 014110–1–11, 2008.

[14] G. L. Yuan and S. W. Or, "Enhanced piezoelectric and pyroelectric effects in single-phase multiferroic $Bi_{1-x}Nd_xFeO_3$ (x = 0–0.15) ceramics," *Applied Physics Letters*, vol. 88, no. 6, pp. 062905–1–3, 2006.

[15] C. Sun, X. Chen, J. Wang, G. Yuan, J. Yin and Z. Liu, "Structure and piezoelectric properties of $BiFeO_3$ and $Bi_{0.92}Dy_{0.08}FeO_3$ multiferroics at high temperature," *Solid State Communications*, vol. 152, no. 14, pp. 1194–1198, 2012.

[16] X. Chen, Y. Wang, Y. Yang, G. Yuan, J. Yin and Z. Liu, "Structure, ferroelectricity and piezoelectricity evolutions of $Bi_{1-x}Sm_xFeO_3$ at various temperatures," *Solid State Communications*, vol. 152, no. 6, pp. 497–500, 2012.

[17] T. Stevenson, D. G. Martin, P. I. Cowin, A. Blumfield, A. J. Bell, T. P. Comyn, P. M. Weaver, "Piezoelectric materials for high temperature transducers and actuators," *Journal of Materials Science: Materials in Electronics*, vol. 26, no. 12, pp. 9256–9267, 2015.

[18] S. R. Basu, L. W. Martin, Y. H. Chu, M. Gajek, R. Ramesh, R. C. Rai, X. Xu and J. L. Musfeldt, "Photoconductivity in $BiFeO_3$ thin films," *Applied Physics Letters*, vol. 92, no. 9, pp. 091905–1–3, 2008.

[19] T. Choi, S. Lee, Y. J. Choi, V. Kiryukhin and S.-W. Cheong, "Switchable ferroelectric diode and photovoltaic effect in $BiFeO_3$," *Science*, vol. 324, no. 5923, pp. 63–66, 2009.

[20] D. Belavic, M. Hrovat, J. Holc, M. S. Zarnik, M. Kosec and M. Pavlin, "The application of thick-film technology in C-MEMS," *Journal of Electroceramics*, vol. 19, no. 4, pp. 363–368, 2007.

[21] F. Kubel and H. Schmid, "Structure of a ferroelectric and ferroelastic monodomain crystal of the perovskite $BiFeO_3$," *Acta Crystallographica Section B-Structural Science*, vol. 46, no. 6, pp. 698–702, 1990.

[22] C. Michel, J. M. Moreau, G. D. Achenbach, R. Gerson and W. J. James, "The atomic structure of $BiFeO_3$," *Solid State Communications*, vol. 7, no. 9, pp. 701–704, 1969.

[23] J. G. Park, M. D. Le, J. Jeong and S. Lee, "Structure and spin dynamics of multiferroic $BiFeO_3$," *Journal of Physics: Condensed Matter*, vol. 26, no. 43, pp. 433202–1–33, 2014.

[24] A. Palewicz, R. Przeniosło, I. Sosnowska and A. W. Hewat, "Atomic displacements in $BiFeO_3$ as a function of temperature: neutron diffraction study," *Acta Crystallographica Section B-Structural Science*, vol. 63, no. 4, pp. 537–544, 2007.

[25] R. Seshadri and N. A. Hill, "Visualizing the role of Bi 6s »lone pairs« in the off-center distortion in ferromagnetic $BiMnO_3$," *Chemistry of Materials*, vol. 13, no. 9, pp. 2892–2899, 2001.

[26] P. Ravindran, R. Vidya, A. Kjekshus, H. Fjellvåg and O. Eriksson, "Theoretical investigation of magnetoelectric behavior in $BiFeO_3$," *Physical Review B*, vol. 74, no. 22, pp. 224412–1–18, 2006.

[27] J. R. Chen, W. L. Wang, J. B. Li, G. H. Rao, "X-ray diffraction analysis and specific heat capacity of $(Bi_{1-x}La_x)FeO_3$ perovskites," *Journal of Alloys and Compounds*, vol. 459, no. 1-2, pp. 66–70, 2008.

[28] Q. Li, D. H. Huang, Q. L. Cao and F. H. Wang, "Phase transition and thermodynamic properties of $BiFeO_3$ from first-principles calculations," *Chinese Physics B*, vol. 22, no. 3, pp. 037101–1–7, 2013.

[29] R. Mazumder, S. Ghosh, P. Mondal, D. Bhattacharya, S. Dasgupta, N. Das, A. Sen, A. K. Tyagi, M. Sivakumar, T. Takami and H. Ikuta, "Particle size dependence of magnetization and phase transition near T_N in multiferroic $BiFeO_3$," *Journal of Applied Physics*, vol. 100, no. 3, pp. 033908–1–9, 2006.

[30] S. M. Selbach, T. Tybell, M. A. Einarsrud and T. Grande, "The ferroic phase transitions of $BiFeO_3$," *Advanced Materials*, vol. 20, no. 19, pp. 3692–3696, 2008.

[31] R. Haumont, I. A. Kornev, S. Lisenkov, L. Bellaiche, J. Kreisel, B. Dkhil, "Phase stability and structural temperature dependence in powdered multiferroic $BiFeO_3$," *Physical Review B*, vol. 78, no. 13, pp. 134108–1–8, 2008.

[32] R. Haumont, J. Kreisel, P. Bouvier and F. Hippert, "Phonon anomalies and the ferroelectric phase transition in multiferroic $BiFeO_3$," *Physical Review B*, vol. 73, no. 13, pp. 132101–1–4, 2006.

[33] I. Kornev, S. Lisenkov, R. Haumont, B. Dkhil and L. Bellaiche, "Finite-temperature properties of multiferroic $BiFeO_3$," *Physical Review B*, vol. 99, no. 22, pp. 227602–1–4, 2007.

[34] D. C. Arnold, K. S. Knight, G. Catalan, S. A. T. Redfern, J. F. Scott, P. Lightfoot, and F. D. Morrison, "The β-to-γ transition in $BiFeO_3$: a powder neutron diffraction study," *Advanced Functional Materials*, vol. 20, no. 13, pp. 2116–2123, 2010.

[35] M. Guennou, P. Bouvier, G. S. Chen, B. Dkhil, R. Haumont, G. Garbarino and J. Kreisel, "Multiple high-pressure phase transitions in $BiFeO_3$," *Physical Review B*, vol. 84, no. 17, pp. 174107–1–10, 2011.

[36] M. Guennou, P. Bouvier, R. Haumont, G. Garbarino and J. Kreisel, "High-pressure phase transitions in $BiFeO_3$: hydrostatic vs. non-hydrostatic conditions," *Phase Transitions*, vol. 84, no. 5-6, pp. 474–482, 2011.

[37] X. L. Zhang, Y. Wu, Q. Zhang, J. C. Dong, X. Wu, J. Liu, Z. Y. Wu and D. L. Chen, "Pressure-induced phase transitions of multiferroic $BiFeO_3$," *Chinese Physics C*, vol. 37, no. 12, pp. 128001–1–5, 2013.

[38] S. M. Selbach, M. A. Einarsrud and T. Grande, "On the thermodynamic stability of $BiFeO_3$," *Chemistry of Materials*, vol. 21, no. 1, pp. 169–173, 2009.

[39] M. Valant, A. K. Axelsson and N. Alford, "Peculiarities of a solid-state synthesis of multiferroic polycrystalline $BiFeO_3$," *Chemistry of Materials*, vol. 19, no. 22, pp. 5431–5436, 2007.

[40] M. S. Bernardo, T. Jardiel, M. Peiteado, A. C. Caballero and M. Villegas, "Reaction pathways in the solid state synthesis of multiferroic $BiFeO_3$," *Journal of the European Ceramic Society*, vol. 31, no. 16, pp. 3047–3053, 2011.

[41] T. Rojac, M. Kosec, B. Budic, N. Setter and D. Damjanovic, "Strong ferroelectric domain-wall pinning in $BiFeO_3$ ceramics," *Journal of Applied Physics*, vol. 108, no. 7, pp. 074107–1–8, 2010.

[42] A. V. Mikhailov, N. A. Gribchenkova, E. N. Kolosov, A.R. Kaul' and A. S. Alikhanyan, "Mass spectrometric investigation of vaporization in the Bi_2O_3–Fe_2O_3 system," *Russian Journal of Physical Chemistry A*, vol. 85, no. 1, pp. 26–30, 2011.

[43] T. T. Carvalho and P. B. Tavares, "Synthesis and thermodynamic stability of multiferroic $BiFeO_3$," *Materials Letters*, vol. 62, no. 24, pp. 3984–3986, 2008.

[44] M. I. Morozov, N. A. Lomanova and V. V. Gusarov, "Specific features of $BiFeO_3$ formation in a mixture of bismuth(III) and iron(III) oxides," *Russian Journal of General Chemistry*, vol. 73, no. 11, pp. 1676–1680, 2003.

[45] S. Phapale, R. Mishra and D. Das, "Standard Enthalpy of Formation and Heat Capacity of Compounds in the Pseudo-Binary Bi_2O_3–Fe_2O_3 System," *Journal of Nuclear Materials*, vol. 373, no. 1-3, pp. 137–141, 2008.

[46] M. Kosec, D. Kuščer and J. Holc, "Processing of ferroelectric ceramic thick films" in *Multifunctional Polycrystalline Ferroelectrics Materials*, L. Pardo, J. Ricote, Eds., Springer, 2011.

[47] T. K. Gupta, "Thick film deposition techniques" in *Handbook of thick- and thin-film hybrid microelectronics*, Wiley, 2003.

[48] D. R. Dinger, Rheology for ceramists, Clemson: C B Dinger, 2010.

[49] A. G. Fredrickson, Principles and applications of rheology, Upper Saddle River: Prentice Hall, 1964.

[50] M. Kosec, J. Holc, B. Malic and V. Bobnar, "Processing of high performance lead lanthanum zirconate titanate thick films," *Journal of the European Ceramic Society*, vol. 19, no. 6-7, pp. 949–954, 1999.

[51] E. S. Thiele, D. Damjanovic and N. Setter, "Processing and properties of screen-printed lead zirconate titanate piezoelectric thick films on electroded silicon," *Journal of the American Ceramic Society*, vol. 84, no. 12, pp. 2863–2868, 2001.

[52] S. P. Beeby, A. Blackburn and N. M. White, "Processing of PZT piezoelectric thick films on silicon for microelectromechancial systems," *Journal of Micromechanics and Microengineering*, vol. 9, no. 3, pp. 218–229, 1999.

[53] P. Glynne-Jones, S. P. Beeby, P. Dargie, T. Papakostas and N. M. White, "An investigation into the effect of modified firing profiles on the piezoelectric properties of thick-film PZT layers on silicon," *Measurement Science and Technology*, vol. 11, no. 5, pp. 526–531, 2000.

[54] M. Hrovat, J. Holc, S. Drnovsek, D. Belavic, J. Cilensek and M. Kosec, "PZT thick films on LTCC substrates with an interposed alumina barrier layer," *Journal of the European Ceramic Society*, vol. 26, no. 6, pp. 897–900, 2006.

[55] M. Hrovat, J. Holc, S. Drnovsek, D. Belavic, J. Bernard, M. Kosec, L. Golonka, A. Dziedzic and J. Kita, "Characterization of PZT thick films fired on LTCC substrates," Journal of Materials Science Letters, vol. 22, no. 17, pp. 1193–1195, 2003.

[56] S. Gentil, D. Damjanovic and N. Setter, "Development of relaxor ferroelectric materials for screen-printing on alumina and silicon substrates," *Journal of the European Ceramic Society*, vol. 25, no. 12, pp. 2125–2128, 2005.

[57] H. Ursic, E. Tchernychova, A. Bencan, J. Jouin, J. Holc, S. Drnovsek, M. Hrovat and B. Malic, "The influence of the platinum substrate roughness on the ferroelectric properties of $0.65Pb(Mg_{1/3}Nb_{2/3})O_3$–$0.35PbTiO_3$ thick films," *Informacije Midem-Journal of Microelectronics Electronic Components and Materials*, vol. 44, no. 1, pp. 14–20, 2014.

[58] S. Gebhardt, L. Seffner, F. Schlenkrich and A. Schoenecker, "PZT thick films for sensor and actuator applications," *Journal of the European Ceramic Society*, vol. 27, no. 13-15, pp. 4177–4180, 2007.

[59] R. K. Bordia and R. Raj, "Sintering behavior of ceramic films constrained by a rigid substrate," *Journal of the American Ceramic Society*, vol. 68, no. 6, pp. 287–292, 1985.

[60] J. Bang and G. Q. Lu, "Densification kinetics of glass-films constrained on rigid substrates," Journal of Materials Research, vol. 10, no. 5, pp. 1321–1326, 1995.

[61] M. Ohring, The material science of thin films, San Diego: Academic Press, 1992.

[62] K. Hiramatsu, T. Detchprohm, I. Akasaki, "Relaxation mechanism of thermal stresses in heterostructure of GaN grown on sapphire by vapor phase epitaxy," *Japanese Journal of Applied Part 1-Regular Papers Short Notes and Review Papers*, vol. 32, no. 4, pp. 1528–1533, 1993.

[63] J. Pavlic, B. Malic and T. Rojac, "Microstructural, structural, dielectric and piezoelectric properties of potassium sodium niobate thick films," *Journal of the European Ceramic Society*, vol. 34, no. 2, pp. 285–295, 2014.

[64] H. Ursic, M. Hrovat, J. Holc, J. Tellier, S. Drnovsek, N. Guiblin, B. Dkhil and M. Kosec, "Influence of the substrate on the phase composition and electrical properties of 0.65PMN–0.35PT thick films," *Journal of the European Ceramic Society*, vol. 30, no. 10, pp. 2081–2092, 2010.

[65] H. Ursic, "Structural and electrical properties of 0.65PMN−0.35PT thick films on different substrates," Jožef Stefan International Postgraduate School, Ljubljana, Slovenia, 2010.

[66] G. Han, J. Ryu, W. H. Yoon, J. J. Choi, B. D. Hahn, J. W. Kim, D. S. Park, C. W. Ahn, S. Priya, D. Y. Jeong, "Stress-controlled $Pb(Zr_{0,52}Ti_{0,48})O_3$ thick films by thermal expansion

mismatch between substrate and $Pb(Zr_{0,52}Ti_{0,48})O_3$ film," *Journal of Applied Physics*, vol. 110, no. 12, pp. 124101–1–5, 2011.

[67] J. Ryu, G. Han, T. K. Song, A. Welsh, S. Trolier-McKinstry, H. Choi, J. P. Lee, J. W. Kim, W. H. Yoon, J. J. Choi, D. S. Park, Ch. W. Ahn, S. Priya, S. Y. Choi and D. Y. Jeong, "Upshift of phase transition temperature in nanostructured $PbTiO_3$ thick film for high temperature applications," *ACS Applied Materials and Interfaces*, vol. 6, no. 15, pp. 11980−11987, 2014.

[68] D. Lee and T. W. Noh, "Giant flexoelectric effect through interfacial strain relaxation," *Philosophical Transactions of the Royal Society A-Mathematical Physical and Engineering Sciences*, vol. 370, no. 1977, pp. 4944–4957, 2012.

[69] Y. Luo, X. Li, L. Chang, W. Gao, G. Yuan, J. Yin and Z. Liu, "Upward ferroelectric self-poling in (001) oriented $PbZr_{0.2}Ti_{0.8}O_3$ epitaxial films with compressive strain," *AIP Advances*, vol. 3, no. 12, pp. 122101–1–8, 2013.

[70] J. Chen, Y. Luo, X. Ou, G. Yuan, Y. Wang, Y. Yang, J. Yin and Z. Liu, "Upward ferroelectric self-polarization induced by compressive epitaxial strain in (001) $BaTiO_3$ films," *Journal of Applied Physics*, vol. 113, no. 20, pp. 204105–1–5, 2013.

[71] B. C. Jeon, D. Lee, M. H. Lee, S. M. Yang, S. C. Chae, T. K. Song, S. D. Bu, J. S. Chung, J. G. Yoon and T. W. Noh, "Flexoelectric effect in the reversal of self-polarization and associated changes in the electronic functional properties of $BiFeO_3$ Thin films," *Advanced Materials*, vol. 25, no. 39, pp. 5643–5649, 2013.

[72] D. Lee, A. Yoon, S. Y. Jang, J. G. Yoon, J. S. Chung, M. Kim, J. F. Scott and T. W. Noh, "Giant flexoelectric effect in ferroelectric epitaxial thin films," *Physical Review Letters*, vol. 107, no. 5, pp. 057602–1–4, 2011.

[73] V. P. Afanas'ev, I. P. Pronin and A. L. Kholkin, "Formation and relaxation mechanisms of the self-polarization in thin ferroelectric films," *Physics of the Solid State*, vol. 48, no. 6, pp. 1214–1218, 2006.

[74] V. P. Afanasjev, A. A. Petrov, I. P. Pronin, E. A. Tarakanov, E. J. Kaptelov and J. Graul, "Polarization and self-polarization in thin $PbZr_{1-x}Ti_xO_3$ (PZT) films," *Journal of Physics: Condensed Matter*, vol. 13, no. 39, pp. 8755–8763, 2001.

[75] I. Coondoo, N. Panwar, I. Bdikin, V. S. Puli, R. S. Katiyar and A. L. Kholkin, "Structural, morphological and piezoresponse studies of Pr and Sc co-substituted $BiFeO_3$ ceramics," *Journal of Physics D-Applied Physics*, vol. 45, no. 5, pp. 055302–1–7, 2012.

[76] I. Coondoo, N. Panwar, R. Rai, H. Amorin and A. L. Kholkin, "Synthesis and physical properties of Ca- and Ta-modified (K,Na)NbO3 lead-free piezoelectric ceramics," *Phase Transitions: A Multinational Journal*, vol. 86, no. 11, pp. 1130–1140, 2013.

[77] M. Davis, N. Klein, D. Damjanovic and N. Setter, "Large and stable thickness coupling coefficients of $[001]_C$-oriented $KNbO_3$ and Li-modified $(K,Na)NbO_3$ single crystals," *Applied Physics Letters*, vol. 90, no. 6, pp. 062904–1–3, 2007.

[78] I. K. Bdikin, J. A. Perez, I. Coondoo, A. M. R. Senos, P. Q. Mantas and A. L. Kholkin, "Ferroelectric domain structure of $PbZr_{0.35}Ti_{0.65}O_3$ single crystals by piezoresponse force microscopy," *Journal of Applied Physics*, vol. 110, no. 5, pp. 052003–1–7, 2011.

[79] J. Pavlic, "Optimization of the processing of potassium sodium niobate thick films and their electromechanical behaviour," Jožef Stefan International Postgraduate School, Ljubljana, Slovenia, 2014.

[80] E. Cattan, T. Haccart, G. Velu, D. Remiens, C. Bergaud and L. Nicu, "Piezoelectric properties of PZT films for microcantilever" *Sensors and Actuators A: Physical*, vol. 74, no. 1-3, pp. 60–64, 1999.

[81] J. Cheng, N. Li, L.Eric Cross and Zh. Meng, "Self-poling effects in sol-gel derived $Pb(Zr_{1-x}Ti_x)O_3$ thin films," *Materials Research Society Symposium-Proceedings*, vol. 748, pp. 179–185, 2003.

[82] A. L. Kholkin, K. G. Brooks, D. V. Taylor, S. Hiboux and N. Setter, "Self-polarization effect in Pb(Zr,Ti)O_3 thin films," *Integrated Ferroelectrics: An International Journal*, vol. 22, no. 1-4, pp. 1045–1053, 1998.

[83] B. Wang, K. W. Kwok, H. L. W. Chan and C. L. Choy, "Internal field and self-polarization in sol–gel-derived lead zirconate titanate films," *Applied Physics A: Materials Science and Processing*, vol. 79, no. 3, pp. 643–646, 2004.

[84] L. H. Wang, M. L. Zhao, C. L. Wang, J. Wang, W. J. Kuai and X. T. Tao, "Piezoelectricity and local structural distortions in $(Na_{0.5}Bi_{0.5})_{1-x}Sr_xTiO_3$-$Bi_{12}TiO_{20}$ flexoelectric-type polar ceramics," *Applied Physics Letters*, vol. 101, no. 6, pp. 062903–1–4, 2012.

[85] W. J. Kuai, M. L. Zhao, C. L. Wang, L. H. Wang, J. Wang, Z. G. Gai, J. L. Zhang and N. Yin, "Effect of composition on the structure and piezoelectricity of $Na_{0.5}Bi_{4.5}Ti_4O_{15}$-based flexoelectric-type polar ceramics," *Journal of Alloys and Compounds*, vol. 559, pp. 76–80, 2013.

[86] X. Chen, Y. Zou, G. Yuan, M. Zeng, J.M. Liu, J. Yin and Z. Liu, "Temperature gradient introduced ferroelectric self-poling in $BiFeO_3$ ceramics," *Journal of the American Ceramic Society*, vol. 96, no. 12, pp. 3788–3792, 2013.

[87] A. Biancoli, C. M. Fancher, J. L. Jones, D. Damjanovic, "Breaking of macroscopic centric symmetry in paraelectric phases of ferroelectric materials and implications for flexoelectricity," *Nature Materials*, vol. 14, no. 2, pp. 224–229, 2015.

[88] L. M. Garten and S. Trolier-McKinstry, "Enhanced flexoelectricity through residual ferroelectricity in barium strontium titanate," *Journal of Applied Physics*, vol. 117, no. 9, pp. 094102–1–5, 2015.

[89] Y. F. Hou, T. D. Zhang, W. L. Li, W. P. Cao, Y. Yu, D. Xu, W. Wang, X. L. Liu and W. D. Fei, "Self-polarization induced by lattice mismatch and defect dipole alignment in (001) $BaTiO_3$/$LaNiO_3$ polycrystalline film prepared by magnetron sputtering at low temperature," *RSC Advances*, vol. 5, no. 76, pp. 61821–61827, 2015.

[90] B. U. M. Rao, G. Srinivasan, S. Babu and M. S. Seehra, "Magnetic properties of amorphous $BiFeO_3$-$PbZrO_3$ sputtered films," *Journal of Applied Physics*, vol. 69, no. 8, pp. 5463–5465, 1991.

[91] J. Ryu, C. W. Baek, Y. S. Lee, N. K. Oh, G. Han, J. W. Kim, B. D. Hahn, J. J. Choi, W. H. Yoon, J. H. Choi, D. S. Park and D. Y. Jeong, "Enhancement of multiferroic properties in $BiFeO_3$–$Ba(Cu_{1/3}Nb_{2/3})O_3$: film fabricated by aerosol deposition," *Journal of the American Ceramic Society*, vol. 94, no. 2, pp. 355–358, 2011.

[92] T. Futakuchi, T. Kakuda and Y. Sakai, "Preparation of $BiFeO_3$-$BaTiO_3$ based thick films by screen printing," *Key Engineering Materials*, vol. 582, pp. 55–58, 2014.

[93] T. P. Comyn, T. Chakraborty, R. E. Miles and S. J. Milne, "Characterization of laser-transferred bismuth ferrite lead titanate ferroelectric thick films," *Applied Physics Letters*, vol. 93, no. 5, pp. 052909–1–3, 2008.

[94] T. Kawae, H. Tsuda, M. Shiomoto, S. Yamada, M. Nagao, A. Morimoto and M. Kumeda, "Fabrication of $BiFeO_3$ thick films by a simple liquid-phase epitaxial growth technique," *Japanese Journal of Applied Physics*, vol. 47, no. 1, pp. 237–239, 2008.

[95] C. Ponzoni, R. Rosa, M. Cannio, V. Buscaglia, E. Finocchio, P. Nanni and C. Leonelli, "Electrophoretic deposition of multiferroic $BiFeO_3$ sub-micrometric particles from stabilized suspensions," *Journal of the European Ceramic Society*, vol. 33, no. 7, pp. 1325–1333, 2013.

[96] H. Y. Si, W. l. Lu, J. S. Chen, G. M. Chow, X. Sun and J. Zhao, "Hydrothermal epitaxial multiferroic $BiFeO_3$ thick film by addition of the PVA," *Journal of Alloys and Compounds*, vol. 577, pp. 44–48, 2013.

[97] J. Ryu, C. W. Baek, D. S. Park and D. Y. Jeong, "Multiferroic $BiFeO_3$ thick film fabrication by aerosol deposition," *Metals and Materials International*, vol. 16, no. 4, pp. 639–642, 2010.

[98] S. Das, S. Basu, S. Mitra, D. Chakravorty and B. N. Mondal, "Wet chemical route to transparent $BiFeO_3$ films on SiO_2 substrates," *Thin Solid Films*, vol. 518, no. 15, pp. 4071–4075, 2010.

[99] H. Liu, Z. Liu, Q. Liu and K. Yao, "Ferroelectric properties of $BiFeO_3$ films grown by sol–gel process," *Thin Solid Films*, vol. 500, no. 1-2, pp. 105–109, 2006.

[100] P. Du, F. Yang, X. Zang and C. Qiu, "Effect of excess Bi content on the electrical properties of $Bi_{0.95}La_{0.05}FeO_3$ thick films," *Journal of Materials Science-Materials in Electronics*, vol. 25, no. 12, pp. 5316–5321, 2014.

[101] S. J. Guo, C. H. Yang, X. M. Jiang, P. P. Lv and G. D. Hu, "High ferroelectric performance of $Bi_{0.9}La_{0.1}FeO_3$ thick film by optimizing preparation precursor solution," *Journal ot Sol-Gel Science and Technology*, In press. doi: 10.1007/s10971-016-4059-3

[102] J. M. Park, F. Gotoda, S. Nakashima, M. Sohgawa, T. Kanashima and M. Okuyama, "Preparation of $BiFe_{0.9}Co_{0.1}O_3$ films by pulsed laser deposition under magnetic field," *Japanese Journal of Applied Physics*, vol. 50, no. 9, pp. 09NB03–1–5, 2011.

[103] H. Okamoto, "The Bi-Pt (Bismuth-Platinum) system," *Journal of Phase Equilibria*, vol. 12, no. 2, pp. 207–210, 1991.

[104] T. Atsuki, N. Soyama, T. Yonezawa and K. Ogi, "Preparation of Bi-based ferroelectric thin films by sol-gel method," *Japanese Journal of Applied Part 1-Regular Papers Short Notes and Review Papers*, vol. 34, no. 9B, pp. 5096–5099, 1995.

[105] R. A. Young, The Rietveld Method (International Union of Crystallography Monographs on Crystallography), Chester: International Union of Crystallograhy, 1995.

[106] Peakoc version 1.0; the software written by Olivier Masson, Université de Limoges, Limoges Cedex, France; e-mail: olivier.masson@unilim.fr.

[107] A. Pramanick, D. Damjanovic, J. E. Daniels, J. C. Nino and J. L. Jones, "Origins of electro-mechanical coupling in polycrystalline ferroelectrics during subcoercive electrical loading," *Journal of the American Ceramic Society*, vol. 94, no. 2, pp. 293–309, 2011.

[108] V. K. Pecharsky and P. Y. Zavalij, Fundamentals of Powder Diffraction and Structural Characterization of Materials, New York: Springer, 2005.

[109] A. Maitre, M. Francois and J. C. Gachon, "Experimental study of the Bi_2O_3–Fe_2O_3 pseudo-binary system," *Journal of Phase Equilibria and Diffusion*, vo. 25, no. 1, pp. 59–67, 2004.

[110] E. M. Levin and R. S. Roth, "Polymorphism of bismuth sesquioxide. II. Effect of oxide additions on the polymorphism of Bi_2O_3," *Journal of Research of the National Bureau of Standards-A. Physics and Chemistry*, vol. 68A, no. 2, pp. 197–206, 1964.

[111] S. Immovilli, B. Morten and M. Prudenziati, "Interactions between bismuth oxide and ceramic substrates for thick film technology," *Journal of Materials Research*, vol. 13, no. 7, pp. 1865–1874, 1998.

[112] D. Risold, B. Hallstedt, L. J. Gauckler, H. L. Lukas, and S. G. Fries, "The bismuth-oxygen system," *Journal of Phase Equilibria*, vol. 16, no. 3, pp. 223–234, 1995.

[113] B. G. Kakhan, V. B. Lazarev and I. S. Shaplygin, "Study of the subsolidus part of phase diagrams of Bi_2O_3-MO (M = Ni, Cu, or Pd) binary systems," *Zhurnal Neorganicheskoi Khimii*, vol. 24, no. 6, pp. 1663–1668, 1979; *Russian Journal of Inorganic Chemistry* (Engl. Transl.), vol. 24, no. 6, pp. 922–925, 1979.

[114] N. G. Gorashchenko, S. Y. Tsareva, Z. S. Kuchuk and A. A. Maier, "Stoichiometric compositions and crystallochemical regularities of sillenite formations"/ "Стехиометрические составы и кристаллохимические закономерности образования силленитов" [in Russ.], *Perspektivnye Materialy*, vol. 3, no. 6, pp. 46–51, 1999.

[115] J. Cassedanne and C. P. Campelo, "The phase diagram of Bi_2O_3-CuO system", *Anais da Academia Brasileira de Ciências*, vol. 38, no. 1, pp. 35–38, 1966.

[116] J. Assal, B. Hallstedt and L. J. Gauckler, "Experimental phase diagram study and thermodynamic optimization of the Ag–Bi–O System," *Journal of the American Ceramic Society*, vol. 82, no. 3, pp. 711–715, 1999.

[117] Y. S. Touloukian, R. K. Kirby, R. E. Taylor and P. D. Desai, Thermal Expansion: Metallic Elements and Alloys (Thermophysical properties of matter, Vol. 12.), New York: IFI/Plenum, 1975.

[118] R. A. Dorey and R. W. Whatmore, "Electroceramic thick film fabrication for MEMS," *Journal of Electroceramics*, vol. 12, no. 1-2, pp. 19–32, 2004.

[119] D. Kuscer, M. Skalar, J. Holc and M. Kosec, "Processing and properties of $0.65Pb(Mg_{1/3}Nb_{2/3})O_3–0.35PbTiO_3$ thick films," *Journal of the European Ceramic Society*, vol. 29, no. 1, pp. 105–113, 2009.

[120] J. Lu, A. Gunther, F. Schrettle, F. Mayr, S. Krohns, P. Lunkenheimer, A. Pimenov, V. D. Travkin, A. A. Mukhin and A. Loid, "On the room temperature multiferroic $BiFeO_3$: magnetic, dielectric and thermal properties," *European Physical Journal B*, vol. 75, no. 4, pp. 451–460, 2010.

[121] C. Wang, M. Takahashi, H. Fujino, X. Zhao, E. Kume, T. Horiuchi and S. Sakai, "Leakage current of multiferroic $(Bi_{0.6}Tb_{0.3}La_{0.1})FeO_3$ thin films grown at various oxygen pressures by pulsed laser deposition and annealing effect," *Journal of Applied Physics*, vol. 99, no. 5, pp. 054104–1–5, 2006.

[122] G. W. Pabst, L. W. Martin, Y. H. Chu and R. Ramesh, "Leakage mechanisms in $BiFeO_3$ thin films," *Applied Physics Letters*, vol. 90, no. 7, pp. 072902–1–3, 2007.

[123] N. Maso and A. R. West, "Electrical properties of Ca-doped $BiFeO_3$ ceramics: from p-type semiconduction to oxide-ion conduction," *Chemistry of Materials*, vol. 24, no. 11, pp. 2127–2132, 2012.

[124] M. I. Morozov, M. A. Einarsrud and T. Grande, "Control of conductivity and electric field induced strain in bulk $Bi_{0.5}K_{0.5}TiO_3–BiFeO_3$ ceramics," *Applied Physics Letters*, vol. 104, no. 12, pp. 122905–1–4, 2014.

[125] E. T. Wefring, M. A. Einarsrud and T. Grande, "Electrical conductivity and thermopower of $(1–x)BiFeO_3–xBi_{0.5}K_{0.5}TiO_3$ ($x = 0.1, 0.2$) ceramics near the ferroelectric to paraelectric phase transition," *Physical Chemistry Chemical Physics*, vol. 17, no. 14, pp. 9420–9428, 2015.

[126] C. Wang, K. Jin, Z. Xu, L. Wang, Ch. Ge, H. Lu, H. Guo, M. He and G. Yang, "Switchable diode effect and ferroelectric resistive switching in epitaxial $BiFeO_3$ thin films," *Applied Physics Letters*, vol. 98, no. 19, pp. 192901–1–3, 2011.

[127] A. Q. Jiang, C. Wang, K. J. Jin, X. B. Liu, J. F. Scott, C. S. Hwang, T. A. Tang, H. B. Lu and G. Z. Yang, "A Resistive memory in semiconducting $BiFeO_3$ thin-film capacitors," *Advanced Materials*, vol. 23, no. 10, pp. 1277–1281, 2011.

[128] D. Lee, S. H. Baek, T. H. Kim, J. G. Yoon, C. M. Folkman, C. B. Eom and T. W. Noh, "Polarity control of carrier injection at ferroelectric/metal interfaces for electrically switchable diode and photovoltaic effects," *Physical Review B*, vol. 84, no. , pp. 125305–1–9, 2011.

[129] C. Ge, C. Wang, K. Jin, H. Lu and G. Yang, "Recent progress in ferroelectric diodes: explorations in switchable diode effect," *Nano-Micro Letters*, vol. 5, no. 2, pp. 81–87, 2013.

[130] G. Yuan and J. Wang, "Evidences for the depletion region induced by the polarization of ferroelectric semiconductors," *Applied Physics Letters*, vol. 95, no. 25, pp. 252904–1–3, 2009.

[131] R. J. Brook, "Pore-grain boundary interactions and grain growth," *Journal of the American Ceramic Society*, vol. 52, no. 1, pp. 56–57, 1969.

[132] A. J. Schwartz, M. Kumar, B. L. Adams, D. P. Field, Electron Backscattered Diffraction in Material Science, New York: Springer, 2009.

[133] G. Abadias, Y. Y. Tse, P. Guérin and V. Pelosin, "Interdependence between stress, preferred orientation, and surface morphology of nanocrystalline TiN thin films deposited by dual ion beam sputtering," *Journal of Applied Physics*, vol. 99, no. 11, 113519–1–13, 2006.

[134] G. Abadias, "Stress and preferred orientation in nitride-based PVD coatings," *Surface and Coatings Technology*, vol. 202, no. 11, pp. 2223–2235, 2008.

[135] A. M. Vodnick, D. E. Nowak, S. Labat, O. Thomas and S. P. Baker, "Out-of-plane stresses arising from grain interactions in textured thin films," *Acta Materialia*, vol. 58, no. 7, pp. 2452–2463, 2010.

[136] Kyocera, Technical characteristics of Al_2O_3, 99.6% purity, A-493 substrate.

[137] T. Rojac, H. Ursic, A. Bencan, B. Malic and D. Damjanovic, "Mobile domain walls as a bridge between nanoscale conductivity and macroscopic electromechanical response," *Advanced Functional Materials*, vol. 25, no. 14, pp. 1–10, 2015.

[138] K. Lefki and G. J. M. Dormans, "Measurement of piezoelectric coefficients of ferroelectric thin-films," *Journal of Applied Physics*, vol. 76, no. 3, pp. 1764–1767, 1994.

[139] F. Griggio, S. Jesse, A. Kumar, O. Ovchinnikov, H. Kim, T. N. Jackson, D. Damjanovic, S. V. Kalinin and S. Trolier-McKinstry, "Substrate clamping effects on irreversible domain wall dynamics in lead zirconate titanate thin films," *Physical Review Letters*, vol. 108, no. 15, pp. 157604–1–5, 2012.

Bibliography

Publications Related to the Thesis

Journal Articles

E. Khomyakova, M. Sadl, H. Ursic, J. Daniels, B. Malic, A. Bencan, D. Damjanovic and T. Rojac, "Self-poling of $BiFeO_3$ thick films," *ACS applied materials and interfaces*, vol. 8, no. 30, pp. 19626−19634, 2016.

E. Khomyakova, J. Pavlic, M. Makarovic, H. Ursic, J. Walker, V. Shur, T. Rojac, B. Malic and A. Bencan, "Screen-printed $BiFeO_3$ thick films on noble metal foils," *Ferroelectrics*, vol. 496, no. 1, pp. 196−203, 2016.

E. Khomyakova, J. Pavlic, M. Makarovic, H. Ursic, J. Walker, V. Shur, T. Rojac, B. Malic and A. Bencan, "Integration of $BiFeO_3$ thick films onto ceramic and metal substrates by screen printing," *Journal of the European ceramic society*, vol. 35, no. 15, pp. 4163−4171, 2015.

Published scientific conference contribution abstract

E. Khomyakova, J. Pavlic, J. Walker, M. Makarovic, T. Rojac, B. Malic and A. Bencan, "Microstructural characterization of screen-printed $BiFeO_3$ thick films on different substrates," in *9th Young researchers' day*, Ljubljana, Slovenia: Jozef Stefan Institute, 2015.

E. Khomyakova, M. Makarovic, J. Walker, J. Pavlic, T. Rojac, B. Malic and A. Bencan, "The influence of substrate on structure and phase composition of $BiFeO_3$ thick films and the resulting local electro-mechanical properties," in *Modern Nanotechnology International Workshop*, Ekaterburg, Russia: Ural Feredal University, 2015.

E. Khomyakova, J. Pavlic, J. Walker, T. Rojac, B. Malic and A. Bencan, "Interface reactions between screen-printed $BiFeO_3$ thick films and different substrates," in *Piezo 2015 : Electroceramics for End-Users VIII*, Maribor, Slovenia: Piezo 2015, 2015.

E. Khomyakova, J. Pavlic, J. Walker, M. Makarovic, T. Rojac, B. Malic and A. Bencan, "$BiFeO_3$ thick films on different substrates," in *3rd Conference of the Serbian Society for Ceramic Materials*, Belgrade, Serbia: 3CSCS-2015, 2015.

E. Khomyakova, J. Pavlic, T. Rojac, B. Malic and A. Bencan, "Interface reactions in $BiFeO_3$ thick films," in *14th Edition of Electroceramics Conference*, Bucharest, Romania: National Institute of Materials Physics, 2014.

E. Khomyakova, J. Pavlic, T. Rojac, B. Malic and A. Bencan, "Interface reaction between screen-printed $BiFeO_3$ thick films and alumina substrates," in *8th Young Researchers' Day*, Ljubljana, Slovenia: Jožef Stefan Institute, 2014.

E. Khomyakova, T. Rojac, B. Malic and A. Benčan, "Synthesis and microstructure of $BiFeO_3$ thick films," in *Slovenian Chemistry Days 2014*, Maribor, Slovenia: Faculty of Chemistry and Chemical Technology, 2014.

Published scientific conference contribution abstract (invited lecture)

T. Rojac, J. Walker, M. Makarovic, E. Khomyakova, H. Uršič, A. Bencan, B. Malic and D. Damjanovic, "Processing and conductivity issues in $BiFeO_3$-based piezoelectric

ceramics" in *3rd Conference of the Serbian Society for Ceramic Materials*, Belgrade, Serbia: 3CSCS-2015, 2015.

Invited lecture at foreign university

T. Rojac, A. Bencan, H. Uršič, E. Khomyakova, B. Malic, G. Tutuncu, J. L. Jones, J. Daniels and D. Damjanovic, "$BiFeO_3$ ceramics : how far are we in the uderstanding of the porcessing and dynamics of domain-wall-defects interaction under switching and subswitching conditions?" Raleigh, USA: North Carolina State University, Department of Materials Science and Engineering, 2014.

Other Publications

Journal Articles

E. Khomyakova, A. Bencan and B. Malic, "Compositional and microstructural study of sol-gel-derived $PbZr_{0.3}Ti_{0.7}O_3/Al_2O_3/SiO_2$/Si thin-film structures," *Informacije Midem-Journal of Microelectronics Electronic Components and Materials*, vol. 44, no. 1, pp. 25–31, 2014.

Published scientific conference contribution abstract

M. Makarovic, J. Walker, E. Khomyakova, A. Bencan, B. Malic and T. Rojac, "Processing challenges and functional potential of ferroelectric (1-x)$BiFeO_3$-(x)$SrTiO_3$ solid solution." in *10th Young researchers' day*, Ljubljana, Slovenia: Jožef Stefan Institute, 2016.

H. Uršič, A. Bencan, B. Malic, E. Khomyakova, J. Walker, M. Makarovic, D. Damjanovic and T. Rojac, "Local electrical conductivity and domain structure in $BiFeO_3$," in *E-MRS 2015 Fall Meeting & Exhibit*, Warsaw, Poland: Materials Research Society, 2015.

M. Makarovic, J. Walker, E. Khomyakova, A. Bencan, D. Damjanovic and T. Rojac, "The potential of polar-to-non-polar phase boundaries : $BiFeO_3$-$SrTiO_3$ piezoelectric ceramics," in *Piezo 2015: Electroceramics for End-Users VIII*, Maribor, Slovenia: Piezo 2015, 2015.

K. Vojisavljevic, B. Stojanovic, E. Khomyakova, A. Bencan, B. Kmet and B. Malic, "Nanocrystalline $CuAlO_2$ powder by the nitrate-citrate combustion route," in *14th Edition of Electroceramics Conference*, Bucharest, Romania: National Institute of Materials Physics, 2014.

E. Khomyakova, A. Benčan, B. Malic and M. Kosec, "The influence of annealing conditions on the microstructure of Al_2O_3 thin films on silicon substrates," in *7th Young Researchers' Day*, Ljubljana, Slovenia: Jožef Stefan Institute, 2013.

E. Khomyakova, A. Bencan and B. Malic, "Micro structural characterization of sol gel derived $PbZr_{0.3}Ti_{0.7}O_3/Al_2O_3/SiO_2$/Si thin film structures," V: in *Slovenian Chemistry Days 2013*, Maribor, Slovenia: Faculty of Chemistry and Chemical Technology, 2013.

E. Khomyakova, A. Bencan, B. Malic and M. Kosec, "The influence of heat treatment conditions on microstructure of aluminium oxide thin filims on silicon substrate," in *SLONANO 2012*, Ljubljana, Slovenia: Jozef Stefan Institute, 2012.

Biography

In this chapter the educational and professional experience of the author of this thesis with an emphasis on the activity in the scientific field are presented.

Education:

2004-2006	***High school:*** Lomonosov Moscow State University School, Moscow, Russia. Program: Chemistry
2006-2011	***Undergraduate Study:*** Faculty of Chemistry of Lomonosov Moscow State University, Moscow, Russia ***Diploma Thesis:*** "Immobilized transition metal complex with ionic liquids in catalysis of chlorination reaction of alkane with carbon tetrachloride" Mentor: Dr. Tarkhanova I.G. Co-mentor: Dr. Zelikman V.I.
2012-	**Postgraduate Study:** **-** Jožef Stefan International Postgraduate School, Doctoral Study, Programme: Nanoscience and Nanotechnologies

Professional Experience:

2010	***Industrial Practice:*** Kaustik, Volgograd, Russia (1 month)
2011-2012	Research assistant at Electronic Ceramics Department, Jožef Stefan Institute, Slovenia Research topics: Preparation and characterization of lead zirconate titanate thin films on platinized silicon substrate by spin-coating technique.
2012-	PhD student and young researcher under the mentorship of Asst. Prof. Dr. Andreja Benčan Golob at Electronic Ceramics Department, Jožef Stefan Institute, Slovenia. Research topics: Synthesis, screen-printing and characterisation of bismuth ferrite in ceramic and thick film form.

Workshops and Courses:

- Adhesion science and technology course, Bled, Slovenia, 2nd-3rd December 2013
- EBSD introduction short course, Ljubljana, Slovenia, 3rd May 2015Workshop